

# DISORDERED CARBONS AND BATTERY APPLICATIONS

by

Hang Shi

B.Sc. Nanjing University, P.R. China, 1983

M.Sc. Nanjing University, P.R. China, 1985

A THESIS SUBMITTED IN PARTIAL FULFILLMENT  
OF THE REQUIREMENTS FOR THE DEGREE OF  
DOCTOR OF PHILOSOPHY  
in the Department  
of  
Physics

© Hang Shi 1993

SIMON FRASER UNIVERSITY

September 1993

All rights reserved. This work may not be  
reproduced in whole or in part, by photocopy  
or other means, without the permission of the author.

## APPROVAL

Name: Hang Shi  
Degree: Doctor of Philosophy  
Title of thesis: Disordered Carbons and Battery Applications

Examining Committee: Dr. Brett Heinrich  
Chairman

---

Dr. Jeff Dahn  
Senior Supervisor

---

Dr. E. Daryl Crozier

---

Dr. Mike Thewalt

---

Dr. Robert F. Frindt  
Internal Examiner

---

Dr. Mark Sutton  
External Examiner, McGill University

Date Approved:

Sept 27, 1993

PARTIAL COPYRIGHT LICENSE

I hereby grant to Simon Fraser University the right to lend my thesis, project or extended essay (the title of which is shown below) to users of the Simon Fraser University Library, and to make partial or single copies only for such users or in response to a request from the library of any other university, or other educational institution, on its own behalf or for one of its users. I further agree that permission for multiple copying of this work for scholarly purposes may be granted by me or the Dean of Graduate Studies. It is understood that copying or publication of this work for financial gain shall not be allowed without my written permission.

Title of Thesis/Project/Extended Essay

Disordered Carbons And  
Battery Applications

Author: \_\_\_\_\_

(signature)

Hang Shi

(name)

Sept 29, 93

(date)

# Abstract

This dissertation describes studies of the crystal structure of disordered carbons and the electrochemical intercalation of lithium in the disordered carbons. One of the most important applications of carbons is as an electrode material in rechargeable lithium-ion (rocking chair) battery systems. These usually use carbon as the anode and thus depend on the related behavior of lithium intercalation in carbons. An important quantity for measuring the performance of such a battery is the maximum reversible capacity, which strongly depends on the carbon crystal structure. In order to study the structure of disordered carbons, we have developed a structural model for disordered carbons and a corresponding automated structure refinement program for X-ray powder diffraction patterns of disordered carbons. These diffraction patterns can be complex to interpret because of the complicated nature of layer stacking in disordered carbons.

The structural model used in the refinement program is divided into two cases, the one-layer model (for highly disordered carbons) and the two-layer model (for graphitic carbons). Some of the important parameters of the model are, for example, (1) the probability  $P$  of finding a random shift between layers, which is large for disordered carbons like coke and carbon fibers, small for heat treated synthetic graphitic carbons and practically zero for natural graphite; (2)  $P_t$ , the probability of finding a local 3R stacking fault in graphitic carbons; (3)  $1 - g$  (only in the one layer model), the percentage of unorganized carbon in disordered carbons; (4)  $\zeta$ , a dimensionless parameter for measuring in-plane strain in the carbon layer; (5) the finite size of carbon grains  $L_a$  (parallel to the layers) and  $L_c$  (perpendicular to the layers); (6) fluctuations in the spacing between adjacent layers; (7) the average lattice constants,  $c$  and  $a$ ; (8) the constant background and other important quantities.

The program minimizes the difference between the observed and calculated diffraction profiles in a least-squares sense by optimizing model parameters analogously to the popular Rietveld refinement method. Unlike the Rietveld method, which is designed for crystalline materials, this program allows the quantification of the finite size, strain and disorder present in disordered carbon fibers and cokes. We have used our model and program <sup>1</sup> to fit over 50 carbons from Canadian, US and Japanese sources. These include cokes, heat treated cokes, fibers, synthetic graphites and mesocarbon etc..

The structural data have been correlated to the maximum reversible capacity,  $x_{max}$ , of  $Li/Li_xC_6$  electrochemical cells to determine how the carbon structure influences the intercalation of lithium. A phenomenological picture which explains the trends in the data has been proposed, which allows us to predict  $x_{max}$  for any carbon, given its structural parameters. We are able to understand qualitatively the variation in  $x_{max}$  with heat treatment temperature and with the types of disorder present in both hard and soft carbons. A general statement about which classes of carbons are most suitable as anodes in lithium-ion cells has been made in the conclusion and some suggestions for future research directions are given.

---

<sup>1</sup>This program is available from the author

# Acknowledgments

Behind every thesis can be found the support and encouragement of many individuals. This thesis is no exception. I would especially like to express my most sincere thanks to Professor Jeff Dahn, my senior supervisor, for guidance and constant encouragement throughout this work. His enormous experimental expertise and theoretical insight were invaluable making this work possible. I feel lucky to have been his student. I have definitely benefited a great deal from his clear understanding of physics and battery research and also from his positive attitude towards life. His confidence and conscientiousness towards research, talent of quickly focusing on the point of a problem and solving it through simple and clear steps will influence the rest of my research career.

I am indebted to Dr. J. N. Reimers for his assistance in programming and many useful suggestions and discussions during this work. He also helped me to clarify some of the mathematic formulae in this thesis.

I wish to thank my graduate committees members, Professor M.L.W. Thewalt, Professor E. D. Crozier, Professor R. F. Frindt and Professor Mark Sutton for their time spent reading my thesis and providing me with valuable comments. I particularly wish to thank Professor E. D. Crozier, the former chairman of graduate students, for his consistently supportive attitude during my Ph. D studies. I also wish to thank Professor G. Kirczenow for his assistance during the early days, when I had arrived at this beautiful city.

I wish to thank Dr. A. K. Sleigh and Dr. Q. Zhong at Moli Energy (1990) Ltd. for supplying me with various carbon samples and allowing me to use their data. I also wish to thank Dr. U. von Sacken , head of R & D at Moli Energy, for providing me

with the opportunity to learn what practical problems may arise in "real-life" battery manufacturing.

Finally, I wish to thank my fellow students: B. M. Way, Alf Wilson, Wu Li, Michelle Baudais, Wolfgang Weydanz and Erik Rossen, for making these past years of working together an enjoyable time.

The generous financial support of Moli Energy Ltd (1990), Maple Ridge, B.C. is gratefully acknowledged.

# Contents

<b>Abstract</b>	<b>iii</b>
<b>Acknowledgments</b>	<b>v</b>
<b>1 Introduction</b>	<b>1</b>
<b>2 Structural Models for Carbons and Graphite</b>	<b>10</b>
2.1 Review of Some Previous Work . . . . .	13
2.2 Structural Model For Disordered Carbons . . . . .	16
2.2.1 Disordered Carbon:One Layer Model . . . . .	17
2.2.2 Graphitic Carbons: Two Layer Model . . . . .	23
<b>3 X-ray Theory of Disordered Carbons</b>	<b>27</b>
3.1 Single Layer With Finite Extent . . . . .	28
3.1.1 Strained Layer . . . . .	32
3.2 Diffraction from Stacked Layers . . . . .	33
3.2.1 G Averaging . . . . .	36
3.3 Powder Averaging . . . . .	37
3.3.1 Tangent Cylinder Approximation (TCA) . . . . .	39
3.3.2 Debye Scattering Equation . . . . .	42
3.4 The Measured Intensity . . . . .	45
3.4.1 Absorption and Sample Thickness . . . . .	45
3.4.2 Polarization Factors . . . . .	48
3.4.3 Preferred Orientation and 00l Peaks . . . . .	48



3.4.4	Thermal Motion . . . . .	48
3.5	Summary . . . . .	48
<b>4</b>	<b>Models and Algorithm</b>	<b>51</b>
4.1	One layer model . . . . .	53
4.2	Two Layer Model . . . . .	55
4.3	Comparing the Two Models . . . . .	56
4.4	Levenberg-Marquardt Method . . . . .	58
4.4.1	Least Square Merit Function . . . . .	58
4.4.2	How To Minimize A Nonlinear Model . . . . .	60
4.4.3	Gradient and Hessian Matrices . . . . .	61
4.4.4	Adjusting Parameters . . . . .	62
4.4.5	Correlations and Standard Errors . . . . .	64
<b>5</b>	<b>Examples of Fits</b>	<b>69</b>
5.1	Petroleum Pitch Series . . . . .	71
5.2	Conoco Soft Carbon Series . . . . .	78
5.3	Osaka Carbon Series . . . . .	82
5.4	A Hard Carbon Series . . . . .	86
5.5	Hard Carbons Synthesized From Furfuryl Alcohol At Moli . . . . .	91
5.6	A Graphitic Carbon Series . . . . .	99
5.6.1	Summary and Comment . . . . .	103
<b>6</b>	<b>Carbon and Lithium Intercalation Cells</b>	<b>104</b>
6.1	Carbons and Anode Materials . . . . .	104
6.2	Cell Voltage and Chemical Potential . . . . .	105
6.3	Electrochemical Cell Construction and Cycling . . . . .	107
6.3.1	Cathodes . . . . .	107
6.3.2	Electrolyte . . . . .	109
6.3.3	Cycling . . . . .	110
6.4	Li Intercalation in Graphite . . . . .	111
6.4.1	Irreversible Capacity . . . . .	111

6.4.2	Staging . . . . .	114
6.5	Lithium Intercalation in Disordered Carbons . . . . .	117
6.6	Electrochemical Studies On Soft Carbon . . . . .	119
6.6.1	Disordered Soft Carbons . . . . .	120
6.6.2	Graphitic Carbons . . . . .	124
6.7	Electrochemical Studies On Hard Carbon . . . . .	129
6.8	Structural Disorder and Capacities For Soft Carbons . . . . .	133
6.8.1	Probabilities and Disordered carbon . . . . .	133
6.8.2	A Phenomenological Picture . . . . .	138
6.8.3	Graphitic Carbons . . . . .	140
6.8.4	Disordered Soft Carbons . . . . .	141
6.8.5	Summary . . . . .	144
<b>7</b>	<b>Summary and Future Work</b>	<b>148</b>
7.1	Summary of the Thesis . . . . .	148
7.2	Suggestions for Future Work . . . . .	149

## List of Symbols

$a$	lattice constant (in plane)
$\vec{a}_1, \vec{a}_2, \vec{a}_3$	unit cell vectors
$A(\vec{s})$	the amplitude of the beam diffracted by the stack of M layers
$A, B, C$	hexagonal close-packed layer notation
$\vec{b}_1, \vec{b}_2, \vec{b}_3$	reciprocal lattice vectors corresponding to $\vec{a}_1, \vec{a}_2$ and $\vec{a}_3$ .
$B$	the isotropic temperature factor
$c$	twice of $d_{002}$ , the lattice constant normal to graphite layer
$\eta(\epsilon_1, \epsilon_2)$	Fourier transform of shape function $g(x, y, 0)$
$d_{002}$	the average interplanar spacing
$dA$	the element of the intersection surface of the sphere of radius S and the $hk$ rod.
$f(s)$	the atomic scattering factor of carbon
$F(\vec{s})$	structure factor of a single layer
$g(x, y, z)$	crystallite shape function, 0 outside the crystallite and 1 inside the crystallite
$g$	the fraction of organized or low strain carbon atoms
$G_{hk}(s, \varphi)$	the modulation function which takes turbostratic disorder and strain along the $Z$ direction into account
$h, k, l$	<i>Miller</i> indices
$i_{hk}(\vec{s})$	scattering intensity of the $hk$ rod
$I(s)$	the powder intensity per unit cell at scattering vector $\vec{s}$
$I(\theta')$	the powder intensity modified by absorption and sample thickness
$L_0$	the distance between the X-ray source and the sample.
$L_a$	lateral extent of single layer sheets
$L_c$	extent of the crystallites perpendicular to the layers
$M$	the number of layers of a specific substack in the powder grain
$M_0$	the average number of layers of a specific substack in the powder
$n_1, n_2, n_3$	integers used to sum over all unit cells
$p_{n1}, p_{n2}, p_{n3}$	see definition for $\vec{r}_{n1}, \vec{r}_{n2}, \vec{r}_{n3}$

$po(\varphi)$	the preferred orientation function
$p^k, p_k$	the probability distribution of random translation between adjacent layers
$P$	the probability of finding a random shift between adjacent layers (one layer model) or between adjacent packages (two layer model)
$P_i$	the probability of finding a local 3R stacking
$PO$	a parameter in $po(\varphi)$
$p(\delta)$	the distribution of c-axis strain, $\delta$
$P(\theta)$	polarization factor
$q$	average phase factor $\langle e^{2i\pi\vec{s}\cdot\Delta\vec{r}} \rangle$
$\vec{r}_m, \vec{r}_{m'}$	vectors from the origin to two homologous points in layers $m$ and $m'$
$\vec{r}_n$	$\vec{r}_n = \vec{r}_m - \vec{r}_{m'}$
$\vec{\Delta}_n$	the projection of $\vec{r}_n$ parallel to the carbon plane
$\Delta\vec{r}(i, i+1)$	displacement between homologous points of adjacent layers $i$ and $i+1$
$\Delta\vec{r}$	the random translation between adjacent layers
$\vec{r}_{n1}, \vec{r}_{n2}, \vec{r}_{n3}, \dots$	vectors allowed between homologous points of $n$ th neighbor layers with corresponding probabilities $p_{n1}, p_{n2}, p_{n3}, \dots$
$x, y, z$	space coordinate
$R$	the radius of a Bragg rod
$\vec{v}_1, \vec{v}_2$	registered translations for a carbon layer $ABABAB\dots$ stacking
$\vec{R}$	a Bravais lattice vector
$\vec{s}$	scattering vector with magnitude $s = 2\sin(\theta)/\lambda$
$\vec{s}_0$	the reciprocal lattice vector of 2-dimensional layer
$t, dt$	the thickness of the sample and an infinitesimal change of thickness
$T(s, \varphi)$	a function related to layer shape for intensity calculation
$\hat{u}$	a unit vector parallel to the Bragg rod
$U, V$	coordinates in a coordinate system which has the one axis parallel to the rod and another perpendicular to the rod
$V(x)$	Voltage $V$ as a function of lithium concentration, $x$ , in carbon
$W_b, W_h$	the width of the X-ray beam, $W_b$ , and the sample holder, $W_h$ .
$Z$	the coordinates in $\hat{u}$ direction

$x_{max}$	maximum reversible capacity
$\vec{v}_i$	the coordinates of atoms in a unit cell
$\alpha(\vec{s})$	geometrical structure factor for a carbon unit cell
$\beta_n, \gamma_n$	x and y components of random shift parallel to layer
$\sigma_i$	measurement error
$\alpha_{ij}$	covariance matrix
$\sqrt{\langle \delta \rangle^2}$	fluctuation in the spacing between adjacent sheets (one layer model) or between two layer packages (two layer model)
$\zeta$	a parameter for describing in-plane strain
$\delta_D$	Dirac delta function
$\delta\theta$	the change of Bragg angle due to the thickness of the sample
$\lambda$	X-ray wavelength
$\epsilon_1, \epsilon_2$	small deviation of the scattering vector from the center of the Bragg rod
$\theta$	Bragg angle
$\theta'$	the changed Bragg angle due to thickness and absorption of sample
$\theta_1$	monochromator angle
$\varphi$	the angle between the scattering vector and the basal plane
$\Phi(\vec{s})$	amplitude of x-rays scattered in direction $\vec{s}$ by a single layer
$d\Omega$	an element of solid angle
$\mu$	absorption length
$\mu_c, \mu_c^0$	Li chemical potential in carbon, $\mu_c$ , and in lithium metal, $\mu_c^0$ .
$\chi^2$	a goodness of fit function for least square fitting

# List of Tables

2.1	Applications of Carbon and Graphite in Electrochemical Technologies . .	11
2.2	Parameters of Models . . . . .	26
4.1	The meaning of parameters in the output file . . . . .	67
5.1	Selected Carbons Fitted and Plotted For Examples . . . . .	70
5.2	The Structural Parameters and Selected Correlation Percentages for the Five Petroleum Pitch Carbons . . . . .	77
5.3	The Structural Parameters and Selected Correlation Percentages for the Three Conoco Carbons . . . . .	85
5.4	The Structural Parameters and Selected Correlation Percentages for the Four Osaka Carbons . . . . .	86
5.5	The Structural Parameters and Selected Correlation Percentages for the Three Hard Carbons . . . . .	91
5.6	The Structural Parameters and Selected Correlation Percentages for the Three FA Hard Carbons . . . . .	95
5.7	The Structural Parameters and Selected Correlation Percentages of the Six Graphitic Carbons Studied by the Two Layer Model . . . . .	99
6.1	The Reversible Capacity and HTT For Disordered Soft Carbons . . . . .	120
6.2	The Maximum Reversible Capacity and HTT For Soft Carbons . . . . .	127
6.3	The Maximum Reversible Capacity and HTT For Hard Carbons . . . . .	132
6.4	Electrochemical and Structural Data for disordered carbons . . . . .	146
6.5	Electrochemical and Structural Data for graphitic carbons . . . . .	147

# List of Figures

1.1	Schematically showing the discharge of a rocking chair cell . . . . .	2
1.2	Schematically showing the working mechanism of $Li_x/C_6$ Cell . . . . .	3
1.3	The first discharge, first charge and second discharge for two soft carbons, petroleum pitch heated to 900C and 2850C . . . . .	4
1.4	The Diffraction Patterns (Solid lines) and Calculation Patterns (Dashed Lines) of Petroleum Pitch 900°C and 2850°C . . . . .	6
1.5	The Diffraction Patterns (Solid Lines) and Calculated Patterns (Dashed lines) of Petroleum Pitch 2850°C . . . . .	7
2.1	The Honeycomb structure of a graphite layer and the <i>ABAB</i> stacking structure of 2H graphite . . . . .	12
2.2	Ordered and disordered stacking in disordered carbon . . . . .	12
2.3	The comparison between the 2D and 3D peaks . . . . .	14
2.4	Carbon with unorganized and organized regions . . . . .	18
2.5	A Typical X-ray Pattern for Highly Disordered Carbon . . . . .	20
2.6	a) Calculated (002) profiles for $d_{002} = 3.5\text{\AA}$ , $\delta = 0.0\text{\AA}$ , at different values of $M$ . This simulates the sharp particle size cutoff model. One curve, $\langle M \rangle = 5$ , has been averaged over $M$ as described in section 2.2.1 of the thesis. b) Same as a) except $M = 20\text{\AA}$ and $\delta$ varies. For $\delta = 0.5\text{\AA}$ , one curve has been averaged over $M$ (indicated by $\langle M \rangle$ in figure). This simulates highly strained adjacent layers. . . . .	22
2.7	Showing the two layer package and <i>ABC</i> stacking faults in two layer model	24
3.1	The Comparison of the equal area Gaussian $N^2 e^{-(Nx)^2/\pi}$ with $\sin^2(Nx)/\sin^2 x$	30

3.2	The reciprocal "lattice" of an ideal two dimensional graphite layer — a hexagonal array of rods . . . . .	31
3.3	The Effect on X-ray intensity of strained layers . . . . .	32
3.4	A $M$ layer stack . . . . .	33
3.5	Showing how averaging over $M$ removes the harmonics in $G(Z)$ between the main (00 $l$ ) reflections, $Z$ is the length of the projection of $\vec{s}$ along $c$ axis. . . . .	37
3.6	Ewald construction for building up powder intensity . . . . .	38
3.7	The tangent cylinder approximation (top view) . . . . .	39
3.8	The tangent cylinder approximation (view along cylinder axis) . . . . .	40
3.9	The Bravis lattice of a graphite layer. Each unit cell contains two carbon atoms . . . . .	42
3.10	The comparison of the Debye calculation with that of the tangent cylinder approximation for a small size graphite layer. . . . .	44
3.11	Equal area rule to determine $L_a$ depending on the choice of polygon shape . . . . .	45
3.12	Schematically showing the sample holder and related parameters . . . . .	46
3.13	Showing the reciprocal rods with Miller index less than 3 . . . . .	49
4.1	Showing the dependence of $Q(g, Z)$ on $g$ and $Z$ . . . . .	53
4.2	Showing how $G$ depends on $g$ and $Z$ , for $M = 20$ and $d_{002} = 3.5\text{\AA}$ , with $\langle \delta^2 \rangle = 0.5\text{\AA}$ . . . . .	54
4.3	The comparison of one layer model with two layer model by changing $P$ . . . . .	57
4.4	Comparing the intensities calculated with the two layer model at different selected $P$ and $P_t$ . . . . .	59
4.5	The flow diagram for L-M fitting method . . . . .	64
5.1	The Diffraction Pattern of Petroleum Pitch 550°C . . . . .	73
5.2	The Diffraction Pattern of Petroleum Pitch 1100°C . . . . .	74
5.3	The Diffraction Pattern of Petroleum Pitch 2000°C . . . . .	75
5.4	The Diffraction Pattern of Conoco 2100°C . . . . .	79
5.5	The Diffraction Pattern of Conoco 2200°C . . . . .	80
5.6	The Diffraction Patterns of Conoco 2300°C . . . . .	81
5.7	The Diffraction Patterns of Conoco 2300°C . . . . .	83



5.8	Blow-up For Comparison between one and two layer fitting . . . . .	84
5.9	The Diffraction Pattern of Osaka 1 . . . . .	87
5.10	The Diffraction Pattern of Osaka 2 . . . . .	88
5.11	The Diffraction Pattern of Osaka 9 . . . . .	89
5.12	The Diffraction Pattern of Osaka 16 . . . . .	90
5.13	The Diffraction Pattern of Hard Carbon 1200 . . . . .	92
5.14	The Diffraction Pattern of Hard Carbon 2000 . . . . .	93
5.15	The Diffraction Pattern of Hard Carbon 2850 . . . . .	94
5.16	The Diffraction Pattern of FA 600°C . . . . .	96
5.17	The Diffraction Pattern of FA 900°C . . . . .	97
5.18	The Diffraction Pattern of FA 1100°C . . . . .	98
5.19	The Diffraction Pattern of G2300 . . . . .	100
5.20	The Diffraction Pattern of G2500 . . . . .	101
5.21	The Diffraction Pattern of G2800 . . . . .	102
6.1	The relation between plateaus in $V(x)$ and first order phase transitions .	106
6.2	Exploded View Of a Typical Lithium Coin Cell . . . . .	108
6.3	Schematic of charger circuit . . . . .	110
6.4	The first cycles of a Li/graphite cell at a 100 hour rate. The electrolyte used was 1M $LiN(CF_3SO_2)_2$ and 12-Crown-4 dissolved in 50:50 PC and EC. . . . .	112
6.5	The square root of the derivative of $-dx/dV$ for the first cycles of a Li/graphite cell at a 100 hour rate. The electrolyte used was 1M $LiN(CF_3SO_2)_2$ and 12-Crown-4 dissolved in 50:50 PC and EC. . . . .	113
6.6	Staging of lithium intercalated graphite compounds . . . . .	114
6.7	A Phase Diagram for $Li_xC_6$ from Dahn (1991) . . . . .	115
6.8	Showing the signiture of phase transitions between staged phase in the voltage profile of Li/graphite cell . . . . .	116
6.9	The first cycles of a Li/Xp coke cell at a 100 hour rate. The electrolyte used was 1M $LiN(CF_3SO_2)_2$ dissolved in 50:50 PC and EC. Cell number is 910206.102. . . . .	117

6.10	The derivative, $-dx/dV$ , for the first cycles of a Li/xp coke cell at a 100 hour rate. The electrolyte used was 1M $LiN(CF_3SO_2)_2$ dissolved in 50:50 PC and EC. Cell number is 910206.102. . . . .	118
6.11	The Voltage Curve of Petroleum Pitch heated to 550°C . . . . .	121
6.12	The Voltage Curve of Petroleum Pitch heated to 1200°C . . . . .	121
6.13	The Voltage Curve of Petroleum Pitch heated to 2000°C . . . . .	122
6.14	The Voltage Curve of Conoco Coke heated to 2100°C . . . . .	122
6.15	Showing the relation between maximum reversible capacities of disordered soft carbon and their heat treatment temperature . . . . .	123
6.16	The Voltage Curve of Conoco Coke heated to 2300°C . . . . .	124
6.17	The Voltage Curve of a mesocarbon heated to 2300°C . . . . .	125
6.18	The Voltage Curve of a mesocarbon heated to 2400°C . . . . .	125
6.19	The Voltage Curve of a mesocarbon heated to 2600°C . . . . .	126
6.20	The Voltage Curve of a mesocarbon heated to 2800°C . . . . .	126
6.21	Showing the relation between maximum reversible capacity and heat treatment temperature for all the soft carbons . . . . .	128
6.22	The Voltage Curve of hard carbon heated to 1200°C . . . . .	130
6.23	The Voltage Curve of hard carbon heated to 2000°C . . . . .	130
6.24	The Voltage Curve of hard carbon heated to 2850°C . . . . .	131
6.25	The Voltage Curve of FA 600 as a function of $x$ . . . . .	131
6.26	The Voltage Curve of FA 1100 as a function of $x$ . . . . .	133
6.27	A summary of probabilities used in our carbon model . . . . .	134
6.28	Random stacking probability versus the heat treatment temperature for soft carbons . . . . .	135
6.29	2H-type stacking probability $1 - P - P_t$ , 3R-type stacking fault probability $P_t$ and probability for buckled layers versus the heat treatment temperature (HTT) for soft carbons . . . . .	136
6.30	Six Carbon atoms share one Lithium in the graphite case . . . . .	137
6.31	Showing that highly distorted layers may accommodate more lithium atoms than randomly stacked flat layers . . . . .	138

6.32	Showing that randomly stacked layers may accommodate less lithium atoms than highly distorted layers . . . . .	139
6.33	Capacities versus $P$ for graphitic carbons . . . . .	140
6.34	Capacities versus $g$ for highly disordered carbon . . . . .	142
6.35	Capacities versus HTT for soft carbons: data and prediction . . . . .	143
6.36	Showing our picture for lithium intercalation into carbons . . . . .	144

*“The increasing complexity of batteries for both civil and military usage has created a complicated technology which is often carried out with only very little limited understanding of the more fundamental aspects of battery problems”*

— Modern Batteries

# Chapter 1

## Introduction

During the last decade *lithium (Anode)/Li intercalatable compounds (Cathodes)* batteries using nonaqueous electrolytes have been intensively studied [1, 2, 3] and successfully commercialized [4] because of their promising high energy density and excellent performance. For example, Ballard Battery System Corp. in North Vancouver, B.C. has been manufacturing *Li/SO<sub>2</sub>* and *Li/MnO<sub>2</sub>* primary batteries for military use for some years. Moli Energy (1990) Ltd. produced a secondary lithium battery based on the *Li/MoS<sub>2</sub>* system in the late 80's [5]. However, potential safety problems associated with the use of lithium metal as a negative electrode often occur. The formation of dendrites on the surface of lithium electrode and the changes in shape of the lithium electrode, can lead to safety problems [5]. In order to eliminate these problems, the concept of a rocking-chair or lithium ion battery has been put forward [6, 7]. These cells use another Li intercalation compound, usually a carbonaceous material, in place of lithium for the anode. The lithium-doped carbon acts much like a lithium electrode, and eliminates the safety problems that exist with lithium metal. During the

discharge of such a cell, the lithium moves out of the intercalated carbon and into another lithium intercalatable compound. Figure 1.1 schematically shows the discharge process.

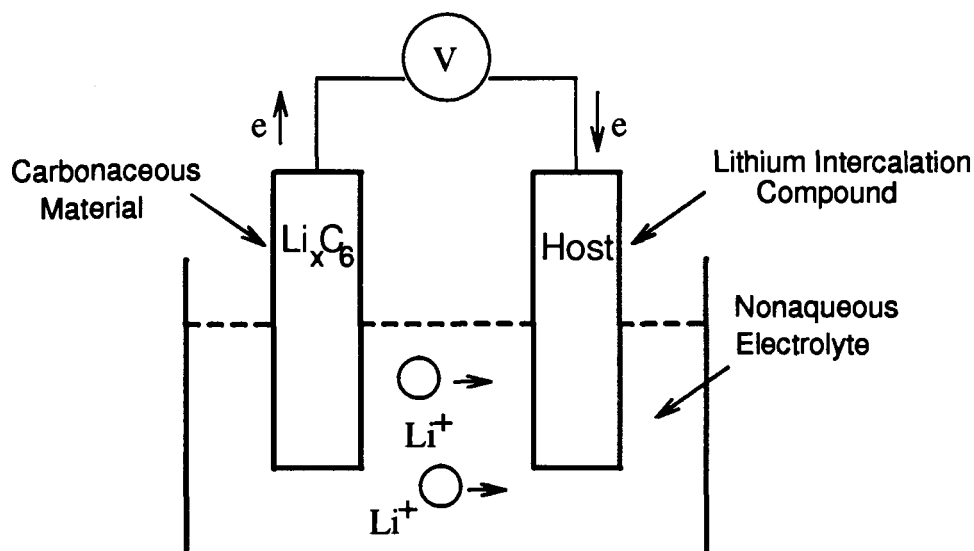


Figure 1.1: Schematically showing the discharge of a rocking chair cell

Searching for better anode and cathode materials for lithium ion cells becomes increasingly important to meet the demands of both environmental issues and for the miniaturization of consumer electronics. Among the many choices for the cathode of lithium ion cells,  $LiCoO_2$ ,  $LiNiO_2$  and  $LiMn_2O_4$  are the three most popular materials [6, 7, 8, 9, 10]. For example, Sony Energytec has commercialized a rechargeable lithium-ion cell that uses the layered intercalation compound  $LiCoO_2$  [11]. Sony is now using these cells to power its cellular phones and videorecorder. Moli Energy (1990) Ltd. is also developing a similar cell. Recently, Bell Communications Research (Bellcore) at Red Bank, N.J. started to develop a cell using  $LiMn_2O_4$  as the cathode. [11]

Among the alternatives for the anode material, the choice is almost exclusively limited to carbons. Carbon is believed to provide the best compromise between large specific capacity and reversible cycling behavior [12, 13, 14]. It is clear that lithium

intercalated carbons are theoretically and industrially vitally important materials. To understand what really influences lithium intercalation into carbons is not only an interesting scientific problem but also an essential issue in the contemporary battery industry. Carbon structures strongly depend on the preparation temperature and process and this structure governs the behavior of lithium intercalation in the carbon.

Experimentally, lithium intercalation in carbon can be studied electrochemically by using  $Li/Li_xC_6$  test cells and measuring the voltage across the cell as a function of time during constant current charging and discharging. The operation of  $Li/Li_xC_6$  test cell during discharge is shown schematically in figure 1.2. During the discharge,

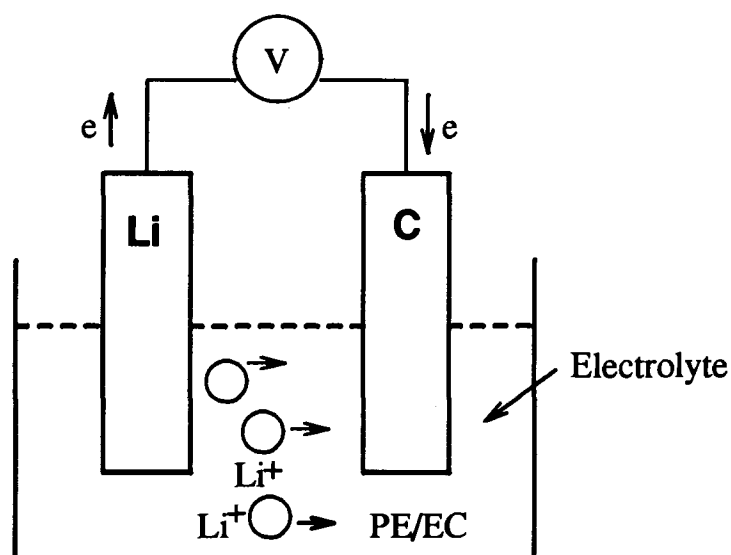


Figure 1.2: Schematically showing the working mechanism of  $Li_x/C_6$  Cell

lithium atoms at the surface of the anode separate into lithium ions and electrons and the  $Li^+$  move through an ionically conducting electrolyte to the carbon electrode. At the carbon, the ion combines with an electron from the external circuit and intercalates into the carbon host. Conversely during the charging of the cell, lithium deintercalates from the carbon host and moves back through the electrolyte to the lithium metal. Theoretically, as long as we know the current, the charging and discharging time and

the mass of the carbon, we can calculate the concentration of lithium in the carbon at any time. Figure 1.3 shows voltage curves versus lithium concentration in the carbon electrode of two  $Li/Li_xC_6$  cells. Two different disordered carbons were used in these cells, Petroleum Pitch 900 and Petroleum Pitch 2850 (the numbers indicate the heat treatment temperature (HTT) in  $^{\circ}C$ ). The first discharge (1D), first charge (1C) and second discharge (2D) are plotted. The capacity of the first discharge is usually about 20% greater than that of subsequent cycles. After the initial discharge, the system stays in a reversible state. These voltage curves illustrate that the voltage profiles of Li/Carbon cells can be substantially different if different carbons are used.

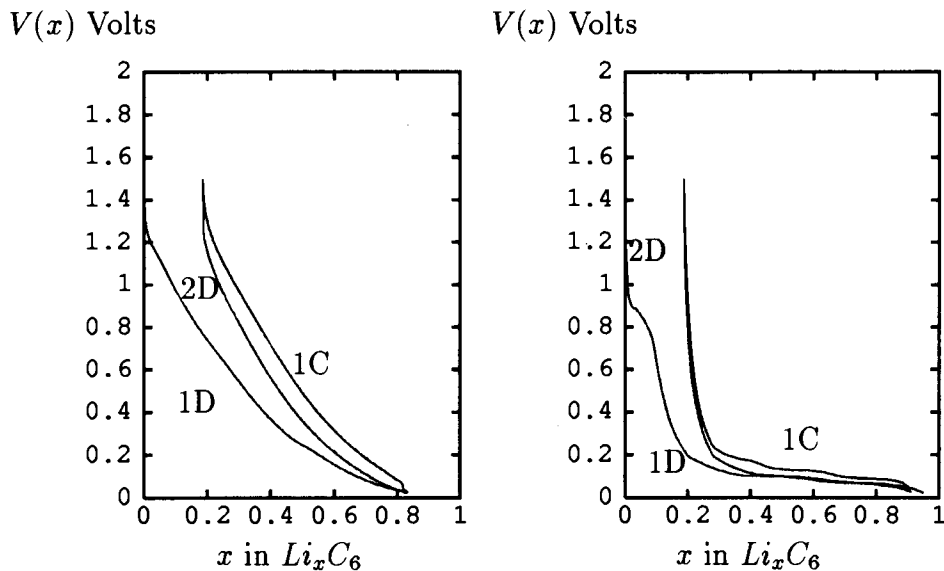


Figure 1.3: The first discharge, first charge and second discharge for two soft carbons, petroleum pitch heated to 900C and 2850C

From the viewpoint of industrial battery researchers, what is really crucial for lithium intercalation into disordered carbon, (except for some other minor technical considerations) is the maximum amount of lithium that is able to reversibly intercalate into carbon. The maximum reversible capacity,  $x_{max}$ , is important because the electrical energy that a cell can release is partially determined by the amount of inserted lithium in the carbon. Consequently, to increase reversible energy density, it

is desirable to increase reversible capacity as much as possible ( The theoretical upper limit is one Li atom per 6 carbon atoms, which corresponds  $x_{max} = 1$  in  $Li_xC_6$ ). The goal of this thesis is to understand the relation between lithium intercalation and carbon structure, both experimentally and theoretically and to determine which carbon is the best for the electrode in lithium ion cells.

We will take three steps to reach this goal. Experimentally, we start with a careful study of the voltage profiles of *Li/carbon* cells We make measurements of the maximum reversible capacities of *Li/carbon* cells by using commercially available carbons and others synthesized at Moli Energy (1990) Ltd.. These carbons include petroleum needle coke heat treated to successively higher temperatures from a US manufacturer (Conoco Ltd.), petroleum pitch heat treated to several temperatures from a Japanese manufacturer, mesocarbons from Osaka Gas Ltd. and several others made at Moli. These carbons differ most notably in their crystal structures.

Theoretically, we begin to examine the structural differences among them. The X-ray diffraction patterns from these disordered carbons can be remarkably different and complicated to interpret. For instance, figure 1.4 shows diffracted intensities versus scattering angles for two petroleum pitch samples heated to different temperatures, 900C and 2850C.

The carbon shown in figure 1.4 (a) is made at low temperatures and is very poorly graphitized. The carbon shown in figure 1.4 (b) is a reasonably well graphitized one. These profiles contain considerable information to allow the key structural differences between these carbons to be elucidated. The question is how to extract the full structural information from such X-ray profiles? Here we show, step by step, that it is possible to calculate these diffraction patterns with a simple structural model developed by us for disordered carbons. The parameters of the model are optimized by least-squares fitting to the X-ray profile as shown in the dashed lines of figure 1.4. We have developed an automated structure refinement program for these carbon X-ray profiles, which simplifies the analysis of these patterns. The refinement program optimizes the following important structural parameters: (1) the extent of crystallites in the basal plane direction, parallel to the graphite sheets,  $L_a$ ; (2) the extent of the crystallites normal to the graphite sheets,  $L_c$ ; (3) the probability,  $P$ , of finding



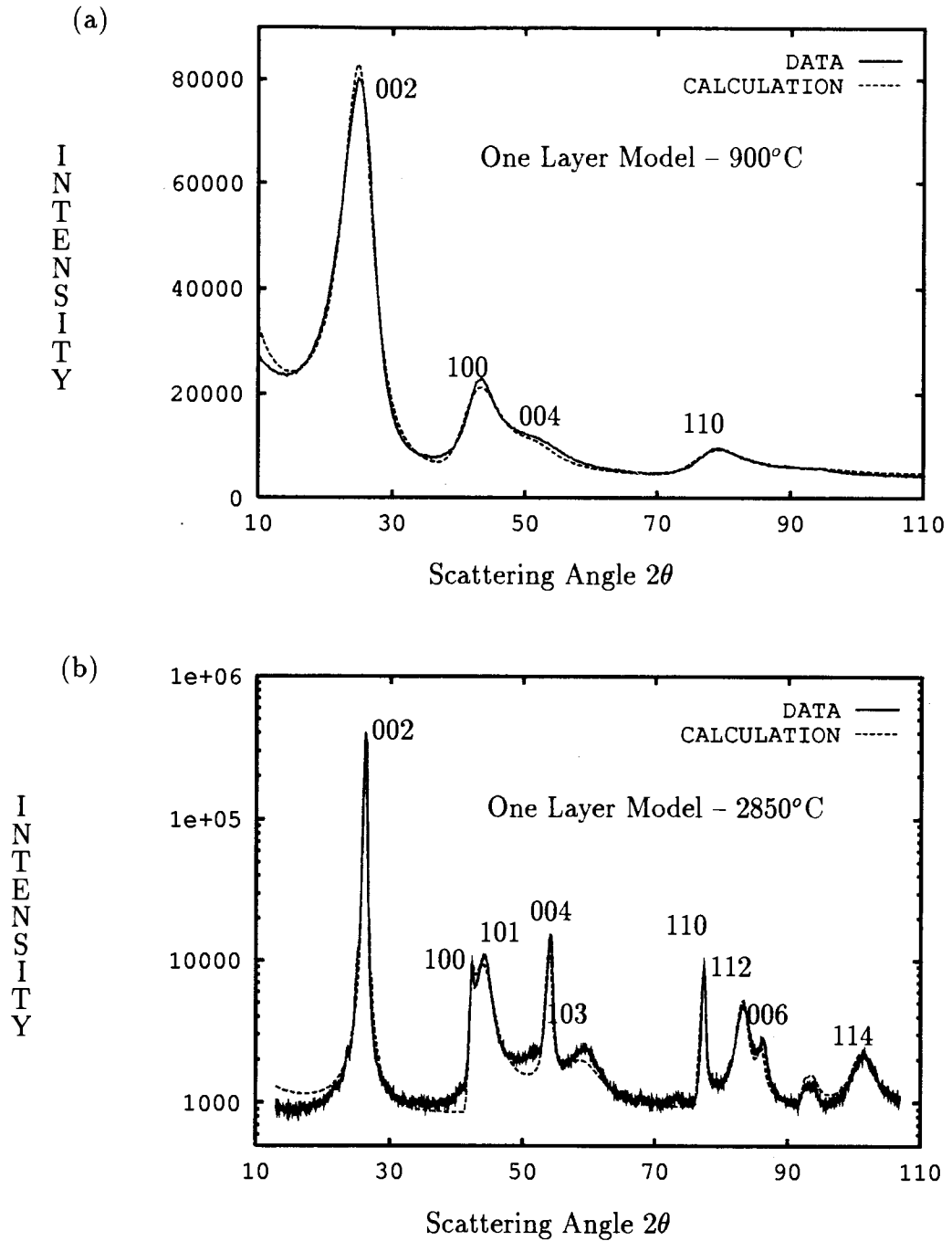


Figure 1.4: The Diffraction Patterns (Solid lines) and Calculation Patterns (Dashed Lines) of Petroleum Pitch 900°C and 2850°C

a random translation between adjacent parallel sheets; (4) a fluctuation in the  $c$ -axis spacing between neighboring layers; (5) an in-plane strain parameter to include distortions in the carbon layer. (6) the fraction of unorganized carbon atoms;  $1 - g$ , which is needed to model very disordered carbons; (7) the lattice constants  $a$  and  $c$ ; (8) a probability,  $P_t$  of finding a local 3R stacking fault in graphitic carbon and other important quantities.

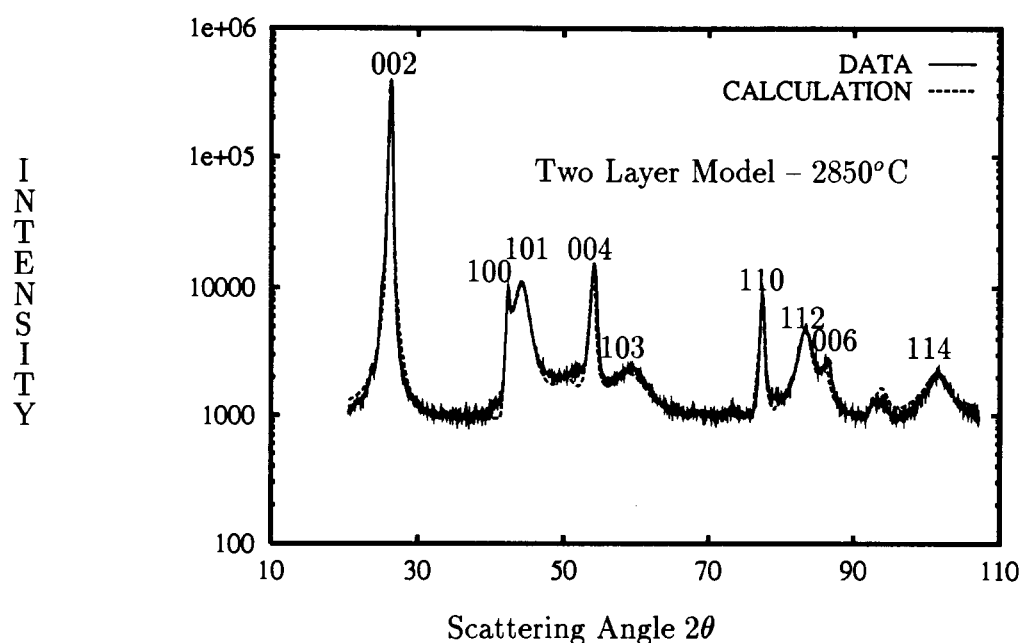


Figure 1.5: The Diffraction Patterns (Solid Lines) and Calculated Patterns (Dashed lines) of Petroleum Pitch 2850°C

The difference between the carbons in figure 1.4 is easily recognized in the light of these structural parameters. For instance, all layers stacked in petroleum pitch 900 are completely random ( $P = 1$ ), the layer size is small ( $L_a = 17\text{\AA}$ ), and there exists large fraction of unorganized carbon regions ( $1 - g = 0.6$ ). Meanwhile, petroleum pitch 2850 has only a small fraction of random stacking ( $P = 0.28$ ), large layer extent ( $L_a = 198\text{\AA}$ ) and zero fraction of unorganized carbon regions etc.. The fit in figure

1.4 (b) is quite poor on careful examination, one finds that the fit in the area between 100 and 110 peaks is not satisfactory. This is due to an oversimplified model (one layer model) used in fitting this quite graphitic carbon (larger layer extent and very few random stacking faults). As a matter of fact, to fit graphitic carbons, we must introduce the probability for registered 3R faults as well as random stacking faults. Figure 1.5 shows the agreement possible if both faults are taken into account.

The diffraction calculation is no simple task. We will detail the procedure later; basically we followed methods outlined in reference [15]. The structure refinement program is a combination of least square and Levenberg-Marquardt treatments for nonlinear problems [16].

Finally we correlate the electrochemically measured maximum reversible capacities to corresponding structural parameters for all the carbons. We then present a phenomenological picture to understand the measurements.

The arrangement of this thesis is as follows. Chapter 2 describes the structural model for the disordered carbons in more physical detail. We will also review some of the previous work on carbon X-ray diffraction, including Warren and Franklin's pioneering work in this area. The model parameters will be defined. Chapter 3 elaborates the theory that we use to calculate the diffraction pattern of carbon. In spite of much work done on the X-ray theory, we still present the formalism in our own notation so that not only the details of our model are made clear but also so that the theory is easier to program. In chapter 4, the phase averaging in the model is discussed and expressed as explicit calculable formula. The relation between model parameters and patterns are examined. The algorithm and techniques used in the structure refinement program are also mentioned briefly. Then, chapter 5 is devoted to illustrations of example fits. The X-ray patterns and fits for different carbons are presented in different sections. The agreement between data and the theory for various carbons is discussed and the corresponding parameters are tabulated respectively. The correlation between the structural data and the electrochemical results is discussed in chapter 6. We start with a short general review of the behaviors of lithium intercalation into graphite and disordered carbons, and a brief description of

cell construction. Cell voltage curves and reversible capacities for a variety of disordered carbons are shown and tabulated. Finally a simple phenomenological model is given to explain how the correlation can be understood. A short summary and outlook will be given in chapter 7.

*“Carbon is a truly old but new material.”*

— Chemistry and Physics of Carbon

## Chapter 2

# Structural Models for Carbons and Graphite

Carbons can be roughly classified into three common forms: <sup>1</sup> diamond, graphite and disordered carbons (hereafter often referred to simply as carbons). The theoretical densities of diamond and graphite are 3.51 and 2.25 g/cm<sup>3</sup> respectively [21]. The density of carbons is less than that of graphite and varies depending on processing. Despite the preciousness and usefulness of diamond, only graphite and carbons are electrochemically active. Graphite and carbons possess the unique combination of chemical, electrical, mechanical, and thermal properties that are attractive in electrochemical technologies. Perhaps the two major reasons for the widespread use of carbon in many electrochemical technologies are its (a) reasonably high electrical conductivity and (b) good corrosion resistance in many electrolytes. Other important factors that contribute to the strong acceptance of carbon in electrochemical systems are its low cost and availability in different physical structures, which are easily fabricated into electrodes. Table 2.1 provides a brief survey intended to illustrate the many uses for carbon in electrochemical systems [21]. A discussion of carbons and graphites and their industrial applications is presented in reference [22].

The ideal graphite structure is an ordered stacking of honeycomb carbon layers

---

<sup>1</sup>Other forms fullerenes e.g. C<sub>60</sub> etc. [17, 18, 19, 20] will not be discussed in this thesis.

(figure 2.1). This structure is somewhat analogous to the stacking of playing cards in an orderly pile where consecutive cards are laterally displaced so that cards 1...3...5 lie above each other in a sequence and cards 2...4...6 form a similar sequence laterally displaced from the first (figure 2.1). Disordered carbons consist of honeycomb carbon layers of varying size with very little order parallel to the layers (turbostratic disorder) shown schematically in figure 2.2.

Table 2.1: Applications of Carbon and Graphite in Electrochemical Technologies

Technology	Applications
Aluminum refining	Anode, cell lining
Chlor-alkali production	Anode, air cathode support
Electrofluorination	Anode
Electrolytic hydrogen production	Electrocatalyst support, anode, cathode
Electroorganic synthesis	Anode, cathode
Low-temperature fuel cells	Electrocatalyst support. bipolar electrode separator, carbon-paper substrate
Hydrogen peroxide production	Cathode
Intercalation compounds for battery electrodes	Cathode, Anode
Lead/acid batteries	Bipolar current collector, electrode additive
Lithium/nonaqueous cells	Conductive matrix for cathode
Lithium/oxyhalide cells	Cathode
Metal/air batteries	Air electrode
Ozone generation	Anode
Flow batteries	Anode, cathode, electrocatalyst support, current collector, bipolar separator
Sodium/sulfur cells	Cathode current collector
Zinc/carbon primary cells	Cathode

The turbostratic disorder between adjacent layers varies from one carbon to another. Hence, describing the turbostratic disorder becomes crucial for models of carbon structure. Although the microstructure of disordered carbon has been studied

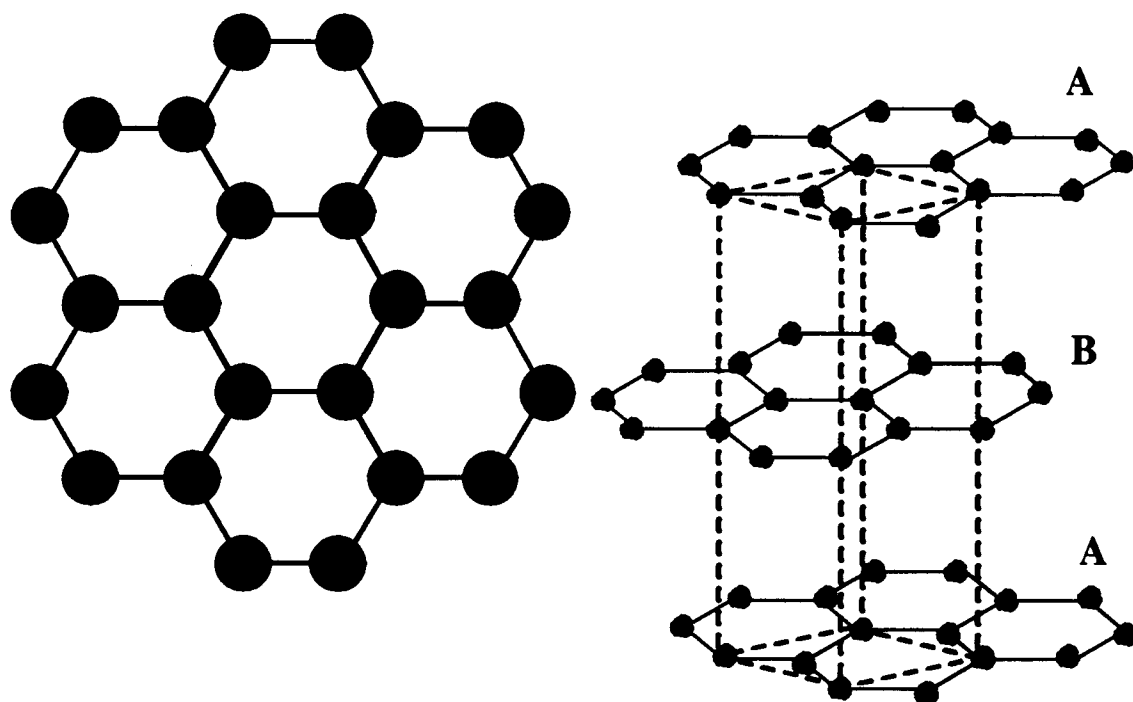


Figure 2.1: The Honeycomb structure of a graphite layer and the *ABAB* stacking structure of 2H graphite

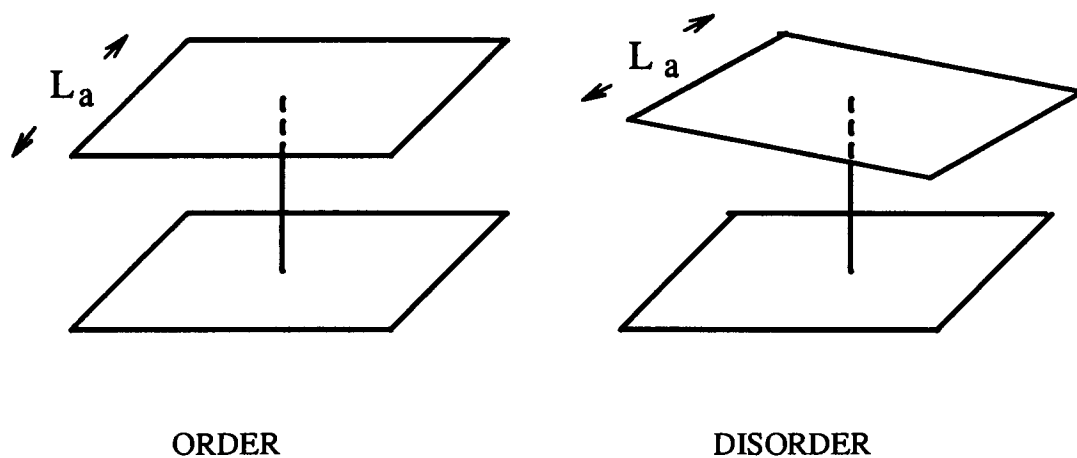


Figure 2.2: Ordered and disordered stacking in disordered carbon

for nearly one century, there still does not exist an unified model that can describe the disorder completely. In this chapter we present a simple model to describe such complicated disorder. However, before we start to elaborate our model, it is worth reviewing important previous work.

## 2.1 Review of Some Previous Work

Bernal (1924)[23] was the first who employed the single-crystal rotation technique to solve the crystal structure of graphite. Ten years later, Warren (1934) [24] reported the first rigorous X-ray diffraction analysis of carbon black from the results of his analytical procedure. Warren concluded that carbon black is composed of individual graphite layers ( hexagonal network of carbon atoms) which appear to be stacked parallel to each other and about 3.6 Å to 3.8 Å apart. He thought that carbon black was a mesomorphic carbon with regular arrangement in two dimensions only.

Later on Warren (1941) [25] published his famous paper in which he expressed quantitatively the 2D diffraction intensity distribution generated by a random layer lattice. These 2D peaks are strongly asymmetric and look much like a triangular spike sharply-cutoff at low scattering angle and with a long tail to large scattering angle. (*Warren tail*, see figure 2.3). Warren also calculated the shape factor constant 1.84 for use in the Scherrer equation [21, 26].

$$L_a = 1.84\lambda/(B_a \cos\theta) \quad (2.1)$$

where  $L_a$  is the dimension of the carbon particle in the plane of the layer,  $\lambda$  is the wavelength of the X-ray beam,  $B_a$  is the angular width of the 2D diffraction peak at half-maximum intensity corrected for instrumental line broadening (see figure 2.3), and  $\theta$  is the Bragg angle. Usually, the (100) and (110) reflections are used in the estimate of  $B_a$ . A corresponding equation for calculating the crystallite dimension perpendicular to the basal plane of graphite,  $L_c$ , is similarly [21]

$$L_c = 0.89\lambda/(B_c \cos\theta) \quad (2.2)$$



where the  $B_c$  is the angular width of the 3D diffraction peak, say (002), at half-maximum intensity. The difference between the constant factor in the two equations is due to the different behavior of 2D and 3D peaks. These equations, or slight modifications of these equations, are widely used to determine crystallite dimensions of various carbons.

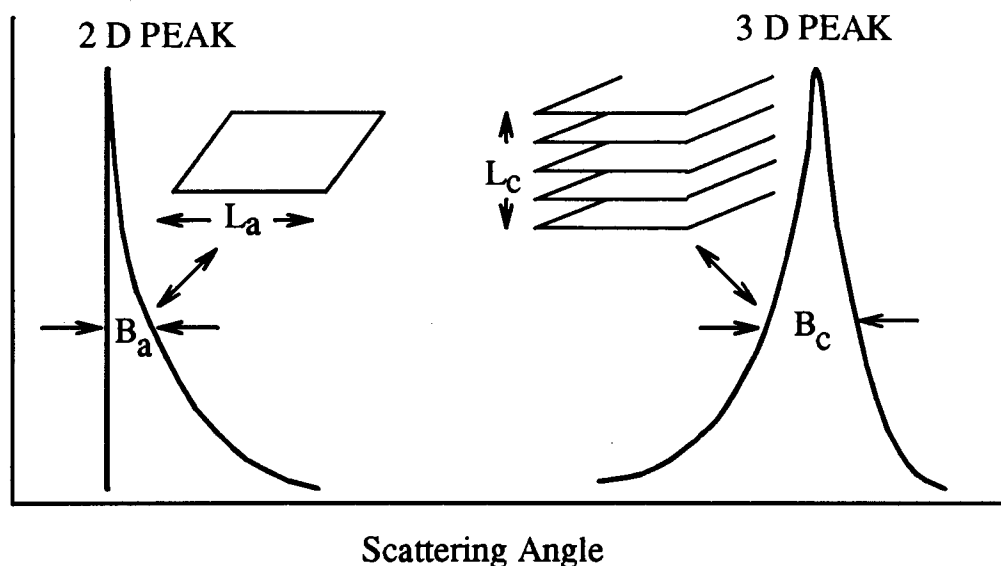


Figure 2.3: The comparison between the 2D and 3D peaks

Biscoe and Warren [27] further elucidated the crystalline nature of carbon by using heat treatment methods. They wrote:

The X-ray studies of the heat-treated carbon blacks allow us to draw the clear and unambiguous conclusion that carbon black is not small graphite crystals. Since the heat treatment at higher temperatures produces a more orderly structure, we can infer with certainty that the original unheated material had the same random layer structure, even though the patterns of the unheated material are too diffuse to allow any such definite conclusion to be drawn. . . . What should carbon black be called? It is not completely amorphous since there is a definite two-dimensional repetition of graphite.

Carbon black is a simple and definite example of an intermediate form of matter, which is distinctly different from both the crystalline and the amorphous states. The term *turbostratic* (unordered layers) is suggested for this particular class of mesomorphic solid.

The crystallographic framework suggested by Biscoe and Warren is, in general, still true today. In the early 1950's, Miss Rosalind E. Franklin [28] made a series of careful studies on the microstructure of carbon. The carbon she studied was polyvinylidene chloride pyrolyzed at 1000°C, which contains graphitelike layers with lots of turbostratic disorder. The sample also contained unorganized carbon atoms, that is, those not incorporated into layer planes. Franklin claimed that all the diffraction patterns could be satisfactorily interpreted assuming that in these samples, only two phases exist: small, perfect graphite layers and highly unorganized carbon. She was also the first who attempted to classify all carbons into two groups: the graphitizing (soft) and non-graphitizing (hard) carbons.<sup>2</sup> The key differences between the two types are crystallite orientation, strength and extent of crosslinking between crystallites. The non-graphitizing carbons show no trace of homogeneous development of the three-dimensional graphite structure, even after heating to 3000°C. However the graphitizing carbons are, by contrast, soft and comparatively dense and their porosity is eventually eliminated by heating.

During the past decades, many people have studied disordered carbons. Houska and Warren [29] have developed the diffraction theory for partially ordered layer groups; Brindley [30] solved the integration problem related to the calculation of the intensity along a 2-dimensional Bragg rod by introducing the tangent cylinder approximation; Allegra [31] created a matrix theory to calculate the diffraction patterns of disordered carbons; J. Mering [32] studied the graphitization of soft carbons etc., just to name a few. To conclude this short review section we list the terminologies that we use in this thesis to describe carbons (for historic reasons, the terminology used in the carbon literature is a mess).

Solid carbon (usually referred to in texts as *carbon*) covers all natural and synthetic

---

<sup>2</sup>The soft carbon graphitizes nearly completely upon heating to 3000°C. The hard carbon never becomes a graphite. We will talk about this later

substances consisting mainly of carbon atoms and two-dimensionally ordered layers of carbon.

A coke is a highly carbonaceous product of pyrolysis of organic material at least parts of which have passed through a liquid or liquid crystalline state during the carbonization process. Most cokes are soft carbons.

Nongraphitic carbons are all varieties of substances consisting mainly of carbon atoms with two-dimensional long range order in planar hexagonal networks but without any measurable crystallographic order in the third direction ( *c* direction), apart from more or less parallel stacking. These are turbostratic carbons.

Graphitic carbons are all varieties consisting of the carbon atoms in the allotropic form of graphite irrespective of the presence of structural defects and characterized by distinguishable three-dimensional order, recognized by at least some modulation of the (*hk*) x-ray reflections. At least, some adjacent layers show non-random stacking.

Nongraphitizable carbon (hard carbon) is a nongraphitic carbon that cannot be transformed into graphitic carbon solely by high-temperature treatment up to 3000°C under atmospheric or lower pressure.

Graphitizable carbon (soft carbon) is a nongraphitic carbon that, upon graphitization heat treatment (above 2000°C), converts into graphitic carbon.

## 2.2 Structural Model For Disordered Carbons

During the century of research on carbon, there have been many models proposed to describe the structure of disordered carbons [33, 34, 35, 25, 15]. Nevertheless, all of these models have an essential assumption, that is, any carbon is made of single atomic sheets of carbon in the graphite honeycomb arrangement which are then stacked to form the carbon. The lateral extent of the sheets ( $L_a$ ) and the number of sheets stacked ( $M$ ) are often model parameters as well. In graphite, the sheets are stacked with  $\cdots ABABAB \cdots$  stacking, but in disordered carbons, the sheets are stacked with turbostratic disorder. At intermediate heat treatment temperatures, (near 2200°C for soft carbons) some neighboring pairs display the  $AB$  registered arrangement, and some show a random displacement parallel to the layers.

### 2.2.1 Disordered Carbon:One Layer Model

To describe the turbostratic disorder between adjacent layers in disordered carbons, we ignore the random rotations and only keep the random shifts in our model. There are two reasons for this. First, the random translations are easier to describe mathematically than the random rotations. Secondly, for the intensity calculation, we need the average phase factor (see chapter 4), which only depends on the correlation between adjacent layers (all random terms will become zero after averaging). In our model, we assume that the turbostratic disorder makes adjacent layers completely uncorrelated with respect to basal position. In the random translation model, we introduce a probability  $P$  of finding a random shift between adjacent layers.  $P$  is large for disordered carbon like coke and small for heat treated synthetic graphite. The remaining layers are assumed to be stacked with the registry of adjacent layers in graphite. If a particular carbon sheet is said to occupy the so-called A position in the notation of hexagonal close packed planes [36], then the choices for the next layer are:

1. a random shift with probability  $P$ ,
2. occupy the  $B$  position with probability  $(1 - P)/2$ , or
3. occupy the  $C$  position with probability  $(1 - P)/2$ .

This model (one layer model) clearly can not reproduce the  $ABABAB \dots$  stacking found in crystalline graphite. But it appears to describe the most disordered carbons adequately since even Lonza KS-44, the most graphitic carbon sample we used, still has a quite large  $P$ . For more crystalline carbons and graphites a model with an  $AB$  stacked primitive sandwich is used (see section 2.2.2).

Ergun (1976)[35] showed that for carbon fibers, strain makes a major contribution to  $(00l)$  peak widths, and must be included, along with particle size, to give a proper description of peak shapes. He also showed (see figure 4 in Ergun (1976)[35]) that the contribution of strain to peak widths of  $(hk0)$  reflections is less than that of particle size.

Hence in order for us to include the c-axis strain and particle size in the model, we take the spacing between adjacent layers to be  $d_{002} + \delta$ , where  $\langle \delta \rangle = 0$  ( $\langle \rangle$  denotes average value) and  $\langle \delta^2 \rangle \neq 0$ . ( $\langle \delta^2 \rangle^{1/2}$  can be considered as the root mean square c-axis strain. The probability of finding a particular strain,  $\delta$ , is determined by the strain probability distribution,  $p(\delta)$ , as we discuss below.) As to basal layer size and c-axis size, we simply assume two refineable parameters  $L_a$  and  $L_c$  to describe them.  $L_a$  and  $L_c$  we introduced in this way are too naive to describe very disordered carbon as we discussed before.

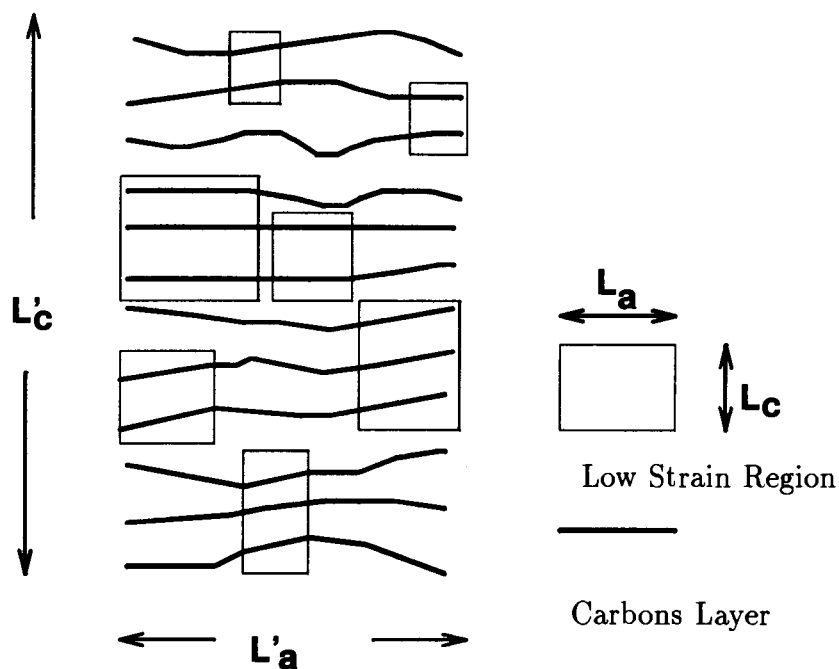


Figure 2.4: Carbon with unorganized and organized regions

For a literal interpretation,  $L_a$  and  $L_c$  are the size of carbon particles which sharply cut off beyond these dimensions. However, this interpretation is incorrect as we show with the following argument and simple measurement. If we use the Scherrer equations (2.1) and (2.2) to estimate  $L_a$  and  $L_c$  from the (100) and (002) peak widths of disordered carbons, then the values we obtain can be as small as  $10\text{\AA}$ . If this were

taken to be the true particle size, the surface area of such carbons would be enormous. However, since the BET [37] surface area of both hard and soft carbons with small  $L_a$  and  $L_c$  can be less than  $1m^2/g$ , it is clear that  $L_a$  and  $L_c$  do not correspond to particle size in the literal sense. Instead, each carbon grain is made up of many small regions characterized by  $L_a$  and  $L_c$  which scatter X-rays incoherently with respect to one another (see figure 2.4). It is  $L_a$  and  $L_c$  not  $L'_a$  and  $L'_c$  in figure 2.4 that the Scherrer equation measures. This means that the phase shift of scattered X-rays from one small region to the next is random. These small regions which scatter coherently within themselves will be called low strain regions or organized carbon regions here. Why do groups of the low strain regions scatter incoherently with respect to each other? Franklin [34] proposes what we consider to be the best explanation. She hypothesized that between each small region characterized by  $L'_a$  and  $L'_c$  there could be found unorganized carbon which is highly strained.

In her picture the unorganized carbon might consist of groups of tetrahedrally bonded carbon or of highly buckled graphitic sheets (in our opinion, buckled sheets are more likely) placed in between the low strain packets. Fig 2.4 shows our view of this situation by using a distorted layer model, which agrees well with the figure 8 in Franklin's paper [34]. It is the presence of the unorganized carbon which leads to the lower densities found in disordered carbons compared to graphite [34]

How can we treat the situation shown in Fig 2.4 in a scattering calculation? The X-ray pattern from such a disordered carbon typically has a very broad (002) peak (see figure 2.5). There is excess intensity in the low angle region. One can adjust the number of layers to give the correct peak width (see figure 2.6a when  $M = 2$ ). However, the calculation always predicts excess intensity below 10 degrees for a broad (002) peak if the sharp particle size cutoff model is used. Figure 2.6b shows that the excess intensity below  $10^\circ$  is reduced, when  $\delta$ , not  $M$  is used to broaden the (002) peaks.<sup>3</sup> The calculation shows a significant increase near  $10^\circ$  in figure 2.6a but smaller increase near  $10^\circ$  in figure 2.6b. We will see that disordered carbons can only be fit

---

<sup>3</sup>In figure 2.6a and 2.6b, we also gave a calculation ( $M = 5$ ,  $\delta = 0.5$ ), which is averaged on  $M$  for comparison. Averaging eliminates the oscillation which exists in calculated pattern (see chapter 3 for details)

well if the (002) peak is broadened by strain.

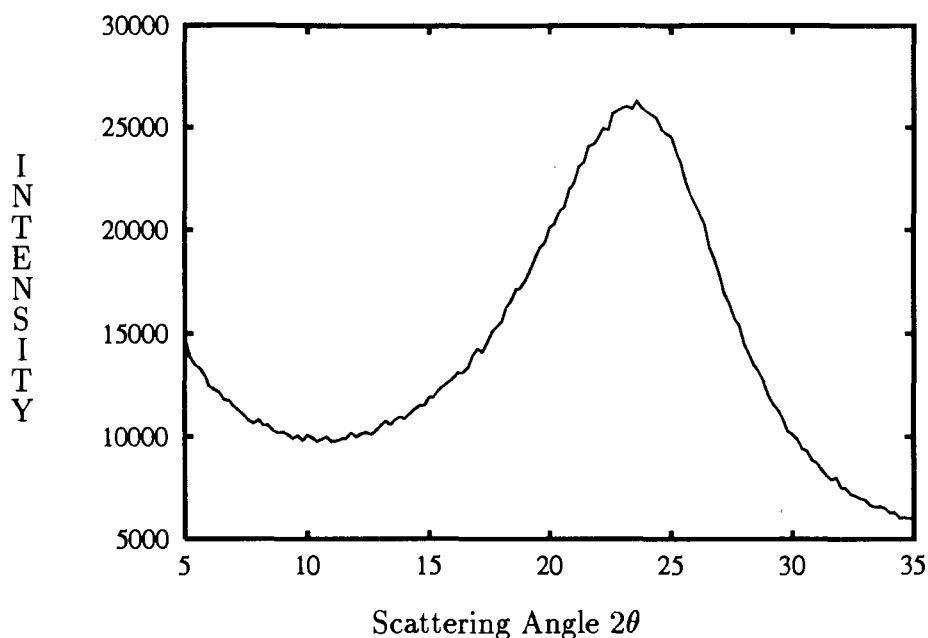


Figure 2.5: A Typical X-ray Pattern for Highly Disordered Carbon

Clearly, a treatment which assumes stacks of  $M$  carbon layers which then sharply terminate is incorrect. In fact, with such a model it is impossible to fit the X-ray data in the region below the (002) peak. The (002) plane spacing of disordered carbons measured by a simple application of the Bragg law to the (002) peak position as measured by powder diffraction can give spurious results. For instance, figure 2.6 (b) clearly shows that the 002 peaks shift to low angle when  $\delta$  increases or  $M$  decreases. This is because the intensity measured in a powder pattern includes the Lorentz-polarization factor (due to the experimental method used) and the square of the carbon atom scattering factor. Both of these functions decrease rapidly with scattering angle. When they are multiplied by a peak in the structure factor (whose center position is determined by  $d_{002}$ ) whose width is several degrees wide, they cause the measured peak to shift to lower scattering angle (see Dahn *et al* [38]). The peak in

the structure factor occurs several degrees higher than that in the data, only because the peak width is large. Many reports of disordered carbons with  $d_{002} > 3.55\text{\AA}$ , especially in the patent literature, are probably incorrect because the (002) peak for these carbons is also very broad.<sup>4</sup>

Theoretically speaking, it is almost impossible to model the situation in figure 2.4 in a rigorous sense. We tackle this problem statistically by selecting a strain probability distribution,  $p(\delta)$ , to reflect the situation shown in figure 2.4 as much as possible. Perhaps it is not the best way to cope with the distorted layers, but, at any rate, it takes these highly strained layers into account, and therefore is a better description than the sharp-cut-off model.

For the strain probability distribution, we choose a combination of a Dirac delta function centered at  $\delta = 0$  to represent the low strain regions and a Gaussian distribution of appropriate width,  $\langle \delta^2 \rangle^{1/2}$ , to represent the layers which are highly strained (refer to figure 4.2, the Fourier transform of (2.3))

$$p(\delta) = g\delta_D(\delta) + (1 - g)\frac{1}{\sqrt{2\pi \langle \delta^2 \rangle}}e^{-\delta^2/(2\langle \delta^2 \rangle)} \quad (2.3)$$

In equation (2.3),  $\delta_D$  is the Dirac delta function, and  $g$  is a number between zero and one which represents the fraction of low strain material present. Consequently, to build up a carbon sample, one selects a layer and places the next layer a distance  $d_{002} + \delta$  away, where  $\delta$  is selected based on the probability  $p(\delta)$ . If  $g$  is near one, there will be many layers selected with a spacing  $d_{002}(\delta = 0)$  before there is a strained layer placed, which could have a very different layer spacing if  $\langle \delta^2 \rangle$  is large ( $\sqrt{\langle \delta^2 \rangle}$  can be as large as  $2\text{\AA}$ ; see carbon S550 in chapter 5). When  $g$  is near zero, only rarely will one find adjacent layers separated by exactly  $d_{002}$ . The reader will see later that the low strain fraction in some disordered carbons can be as low as 20% (e.g. carbon Osaka 1, see chapter 5). This will have important consequence in our interpretation of the electrochemical data.

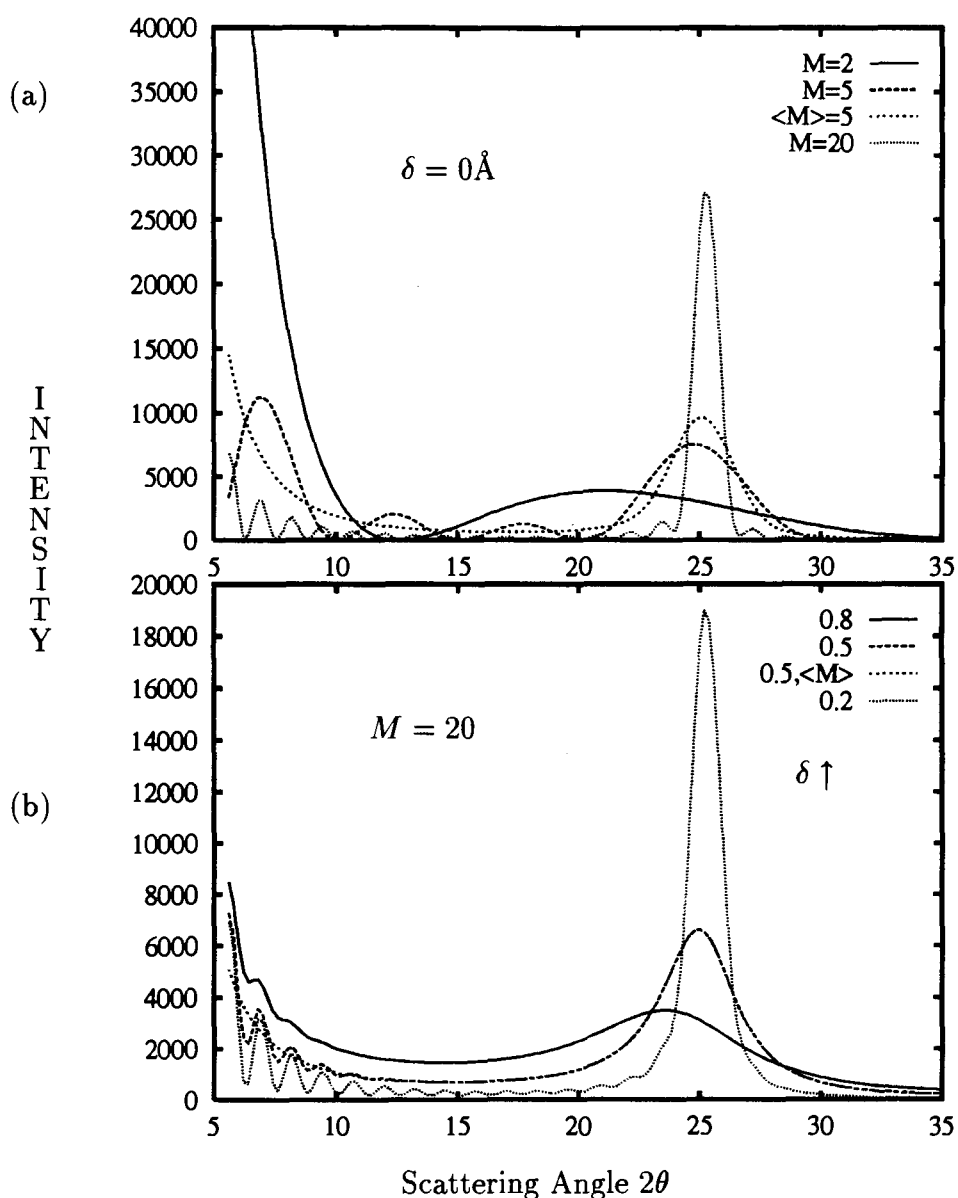
We also include other factors in our model. Ergun (1968)[39] also showed the importance of a careful treatment of sample geometry on the resulting intensity and

---

<sup>4</sup>Once the (002) peak width decreases below about  $2^\circ$ , its position in the powder pattern can be directly used to measure  $d_{002}$ .



Figure 2.6: a) Calculated (002) profiles for  $d_{002} = 3.5\text{\AA}$ ,  $\delta = 0.0\text{\AA}$ , at different values of  $M$ . This simulates the sharp particle size cutoff model. One curve,  $\langle M \rangle = 5$ , has been averaged over  $M$  as described in section 2.2.1 of the thesis. b) Same as a) except  $M = 20\text{\AA}$  and  $\delta$  varies. For  $\delta = 0.5\text{\AA}$ , one curve has been averaged over  $M$  (indicated by  $\langle M \rangle$  in figure). This simulates highly strained adjacent layers.



shapes of Bragg peaks due to the small absorption length of carbon.<sup>5</sup> Our treatment of the absorption is similar to his, but treats the effect of sample holders of small width as well. Ergun (1976) developed a treatment for preferred orientation of carbon samples. Our treatment is identical to his as will be described in the next chapter. Further parameters of the model are: lattice constants; an overall scale factor to scale the calculation to match the data; a constant background parameter; an isotropic thermal parameter etc..

We have found that this model, in spite of its simplicity, can accurately describe the diffraction pattern of disordered carbon as we show in chapter 5.

### 2.2.2 Graphitic Carbons: Two Layer Model

The one layer model breaks down when modeling graphitic carbon because it cannot produce  $ABABAB\dots$  stacking sequences. To reproduce the  $ABAB$  stacking, one must modify the near neighbor probabilities so that the probability of finding a  $B$  or  $C$  layer on an  $A$  layer is not the same. Assume that we want to put one more registered layer on an  $AB$  sandwich stack, obviously we have three choices: (1)  $B$  position, i.e.  $ABB$  (2)  $C$  position, i.e.  $ABC$  (3)  $A$  position,  $ABA$ . Considering the energy minimum of the  $ABAB$  sequence in graphite, one finds that (1) never happens and (2) has much lower probability than (3). That is to say, the  $A$  position is more preferred than  $C$  after an  $AB$  sandwich when the carbon is getting more and more graphitic. How do we include this preference in the simplest way in our theory? In principle, one always can introduce a second neighbor probability to account for this kind of preferred stacking. However, the second neighbor probability makes the theory much more complicated [15]. To simplify the theory and make the model physically more meaningful, we deal with this problem by using a similar model to the one layer model except that the primitive scattering unit now is a two layer package with  $AB$  registered stacking (refer to figure 2.7). These packages are then stacked with the following options:

---

<sup>5</sup>The absorption length of x-rays in 100% bulk carbon is  $9\text{cm}^{-1}$  for  $\text{CuK}\alpha$  radiation, so the penetration of x-rays into thick samples affects peak positions and peak shapes. Our program takes this into account. Powdered samples are usually between 20% and 50% dense.

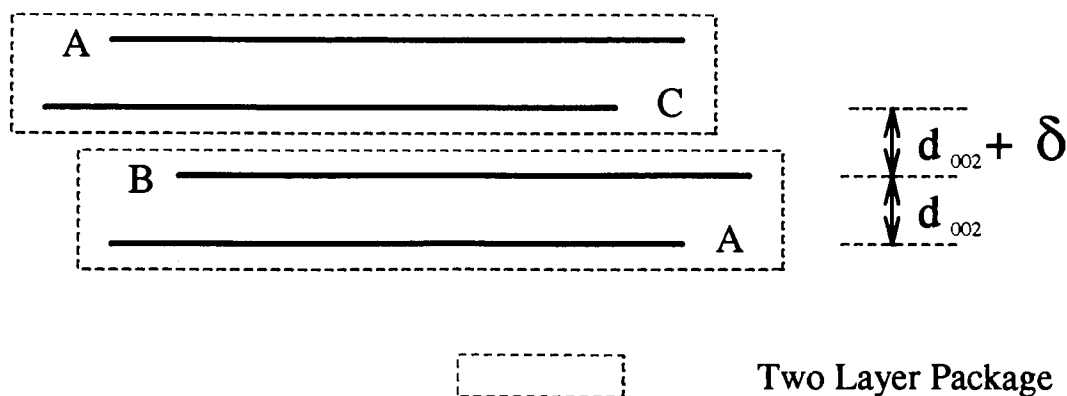


Figure 2.7: Showing the two layer package and  $ABC$  stacking faults in two layer model

1. a random shift between adjacent packages with probability  $P$  or
2. a registered shift between adjacent packages with probability  $P_t$  to make a local 3R type order  $AB/CA/BC$  etc., or
3. no shift at all with probability  $(1 - P - P_t)$ , which gives  $AB/AB$  stacking

Even though *artificial action* is embodied in this model to force  $ABAB$  stacking, it works well. Clearly, if  $P = P_t = 0$ , the  $ABABAB \dots$  stacking form in  $2H$  graphite is found. If  $P = 0$  and  $P_t = 1$ , the  $ABCABC$  stacking of 3R graphite is attained. When  $P_t$  is small, the model includes a small fraction of 3R-type stacking faults in graphitic carbons, which is necessary to reproduce the 3D mixing peaks (see figure 4.4). All the other parameters of the one layer model described in the last section are retained and have the same or similar meaning except that the low strain fraction  $g$  is omitted. In graphitic carbons the layer distortion is small and we use  $\delta$  to specify the strain in the low strain regions, that is, we use

$$p(\delta) = \frac{1}{\sqrt{2\pi} \langle \delta^2 \rangle} e^{-\delta^2 / (2\langle \delta^2 \rangle)} \quad (2.4)$$

for graphitic carbons.

In order to make a comparison with the parameters of the one layer model, the probability to find a random shift between any two carbon sheets in the two layer model should be divided by 2 because half the layers are constrained to be in *AB* registered stacking. For simplicity, we assume that there are no interlayer spacing fluctuations within the two layer package but only between them;  $\sqrt{\langle \delta \rangle^2}$  describes this fluctuation in the two layer model ( $\sqrt{\langle \delta \rangle^2}$  usually is very small). Therefore, the average size of the interlayer spacing fluctuation is  $\frac{1}{2}\sqrt{\langle \delta \rangle^2}$  because half the layer pairs are constrained to have no fluctuation in the two layer model. Also, in the two layer model,  $M$  is the number of two layer stacks, so the number of single layer sheets in the crystal is  $2M$ .

Table 2.2: Parameters of Models

Quantity	1-Layer Model	2-Layer Model
Interplanar spacing	$d_{002}$	$d_{002}$
In-plane lattice constant	$a$	$a$
Probability of random shift between adjacent layers	$P$	$P/2$
Probability of registered 3R-type shift between adjacent two layer packages	Not Applicable	$P_t$
the fraction of low strain	$g$	$No$
the in-plane strain parameter	$\zeta$	$\zeta$
Fluctuation in spacing between adjacent layers	$\sqrt{\langle \delta \rangle^2}$	$\sqrt{\langle \delta \rangle^2}/2$
Number of layers in the crystallite	$M$	$2M$
lateral size of the crystallite	$L_a$	$L_a$
Factor by which (00 $l$ ) reflections are enhanced by preferential orientation	$PO$	$PO$
Absorption length in the sample	$\mu$	$\mu$

Finally, there is a crossover region for material between about 60% and 90% graphitic where both models can be used to describe the carbon. The user must select the model he or she prefers. (usually the selection is easily done, see the example in chapter 5 .) To compare the results of the refinements of the two models one can roughly compare parameters as shown in Table 2.2.

## Chapter 3

# X-ray Theory of Disordered Carbons

The powder X-ray diffractometric method (XRD) is one of the most common and economical tools used in determining local structures related to order-disorder at the angstrom scale. This is due, first of all, to the relative ease of the method and to the moderate cost of the equipment. Secondly, compounds analyzed generally do not need to be put under special experimental conditions, such as vacuum. However, the cost for these conveniences is that the analysis of the data can become tricky. Thus, most interpretations of complicated diffraction profiles produced by partially disordered carbon crystal structures were based on an intuitive approach, which has been summarized in the last part of Heckman's paper on carbon X-ray interpretation [40]. The XRD patterns of disordered carbons are still, to a greater or lesser extent, open to interpretation.

In this chapter the mathematical formalism for calculating the diffraction pattern of a disordered carbon will be developed based on the model described in the last chapter. Historically, Warren (1941) [25] was the first who suggested an explanation for the X-ray diffraction patterns produced by partially disordered lamellar powders. The basic idea is simple, that is, considering a whole layer as a giant crystal-diffracting-unit with a layer structure factor, repeated more or less regularly along a single

direction. Since then, there have been many studies employing similar methods on partially disordered layered systems [41, 42, 43, 44, 45, 46]. In the following, we will use the standard x-ray theory, following closely the treatment of Drits and Tchoubar [15] but completely rewriting in our own notation, to construct our model.

In section 3.1, we start with the discussion of diffraction from a single layer of finite lateral extent. In section 3.2 we consider a stack of layers, in section 3.3 and 3.4 we consider the powder pattern from such a stack, the treatment of the finite size, preferred orientation and penetration of the X-rays into our weakly absorbing samples. Each symbol used in the theory is defined when it is first introduced (also see the list of symbols at the beginning).

### 3.1 Single Layer With Finite Extent

Scattering from a perfect, finite tri-periodic crystal can be fully described by: 1) three unit cell vectors  $\vec{a}_1, \vec{a}_2$  and  $\vec{a}_3$ , 2) the atom positions within each unit cell  $\vec{v}_i$  and corresponding atomic scattering factors  $f_i(\vec{s})$ , where  $\vec{s}$  is the scattering wave vector, 3) the shape function of the crystal,  $g(\vec{R})$ , which is equal to 1 within and 0 outside the crystal [47], and  $\vec{R} = n_1\vec{a}_1 + n_2\vec{a}_2 + n_3\vec{a}_3$  ( $n_1, n_2$  and  $n_3$  are integers), is a Bravais lattice vector. The atomic scattering factor will be approximated by the Fourier transform of the free atom charge density, which is isotropic, and identical for all carbon atoms. We will use the standard analytic representation for the atomic scattering factor described in [48]. The scattering wave vector is related to the scattering angle by  $s = 2\sin\theta/\lambda$ . The scattering amplitude for an array of identical atoms is

$$\Phi(\vec{s}) = f(\vec{s}) \sum_{\vec{R}, \vec{v}} e^{2\pi i \vec{s} \cdot (\vec{R} + \vec{v})} g(\vec{R}) = F(\vec{s}) \eta(\vec{s}) \quad (3.1)$$

where the lattice summation will be truncated by the shape function  $g(\vec{R})$ , and  $F(\vec{s})$  is the structure factor function

$$F(\vec{s}) = f(\vec{s}) \sum_{\vec{v}} e^{2\pi i \vec{v} \cdot \vec{s}}. \quad (3.2)$$

$\eta(\vec{s})$  is the spatial Fourier transform of the shape function

$$\eta(\vec{s}) = \sum_{\vec{R}} g(\vec{R}) e^{2\pi i \vec{s} \cdot \vec{R}}. \quad (3.3)$$

For a 2-dimensional graphite sheet the basis vectors can be chosen as  $\vec{v}_1 = \frac{1}{3}\vec{a}_1 + \frac{2}{3}\vec{a}_2$  and  $\vec{v}_2 = \frac{2}{3}\vec{a}_1 + \frac{1}{3}\vec{a}_2$ . Defining

$$\alpha(\vec{s}) = e^{2\pi i \vec{s} \cdot \vec{v}_1} + e^{2\pi i \vec{s} \cdot \vec{v}_2} \quad (3.4)$$

we have

$$F(\vec{s}) = f(\vec{s})\alpha(\vec{s}). \quad (3.5)$$

For a large enough crystallite  $\eta(\vec{s})$  will be sharply peaked near points of the reciprocal lattice. For this reason it is convenient to isolate the fractional portion of the scattering vector

$$\vec{s} = (h + \epsilon_1)\vec{b}_1 + (k + \epsilon_2)\vec{b}_2 + Z\hat{u}_z = \vec{s}_0 + \vec{\epsilon} + Z\hat{u}_z \quad (3.6)$$

where  $\vec{s}_0 = h\vec{b}_1 + k\vec{b}_2$  and  $\vec{\epsilon} = \epsilon_1\vec{b}_1 + \epsilon_2\vec{b}_2$ , and the  $\vec{b}_i (i = 1, 2)$  are two-dimensional primitive reciprocal lattice vectors such that  $\vec{a}_i \cdot \vec{b}_j = \delta_{ij}$  ( $ij = 1, 2$ ),  $hk$  are integer Miller indices labeling 2D reciprocal lattice points, and  $\hat{u}_z$  is the unit vector perpendicular to the layer plane,  $Z$  is the component in  $\hat{u}_z$  direction, and the  $\epsilon$ 's are fractional deviations of  $\vec{s}$  from the reciprocal lattice point. By definition,  $\eta(\vec{s})$  is independent of  $hk$  and because it is sharply peaked we will neglect the  $\epsilon$  dependence of  $\alpha(\vec{s})$

$$\alpha(\vec{s}) \simeq \alpha_{hk} = 2\cos\left[\frac{2}{3}\pi(h - k)\right] \quad (3.7)$$

Our final expression for the structure factor of carbon atoms is

$$F(\vec{s}) = f(\vec{s})\alpha_{hk} \quad (3.8)$$

The transverse decay of the scattering away from the rods is determined by  $\eta(\epsilon_1, \epsilon_2)$ . For a roughly isotropic layer with diameter  $L_a$ ,  $\eta(\epsilon_1, \epsilon_2)$  can be written as



$$\eta(\epsilon_1, \epsilon_2) = \sum_{\vec{R}} g(\vec{R}) e^{2\pi i \vec{\epsilon} \cdot \vec{R}} = \frac{\sin^2(\pi(N+1)\epsilon)}{\sin^2(\pi\epsilon)} \quad (3.9)$$

where  $N \simeq L_a/a$ ,  $a$  is the in-plane lattice constant, and  $\epsilon = \sqrt{\epsilon_1^2 + \epsilon_2^2 + \epsilon_1\epsilon_2}$  is dimensionless number.  $|\vec{\epsilon}|$  has the same dimension as  $b = \frac{2}{\sqrt{3}a}$ , in fact,  $|\vec{\epsilon}| = b\sqrt{\epsilon_1^2 + \epsilon_2^2 + \epsilon_1\epsilon_2}$ . Writing  $|\eta|^2$  in term of  $|\vec{\epsilon}|$  we have,

$$\eta(|\vec{\epsilon}|) \simeq \frac{\sin^2(\sqrt{3}\pi/2(L_a + a)|\vec{\epsilon}|)}{(\sqrt{3}\pi/2a|\vec{\epsilon}|)^2} \quad (3.10)$$

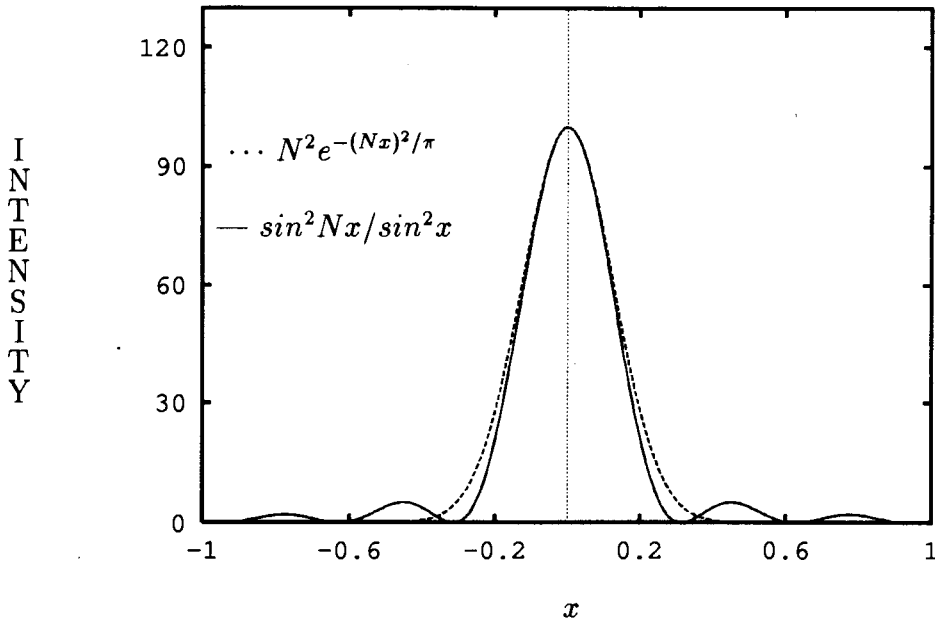


Figure 3.1: The Comparison of the equal area Gaussian  $N^2 e^{-(Nx)^2/\pi}$  with  $\sin^2(Nx)/\sin^2 x$

Following Warren(1969)[49] we replace the above equation with an equal area Gaussian function;

$$\eta(\vec{\epsilon}) \cong \frac{L_a^2}{a^2} e^{-|\vec{\epsilon}|^2/\omega^2} \quad (3.11)$$

with very nearly same half width, as shown in Fig 3.1.

The Gaussian is algebraically more convenient for powder averaging in section 3.4. In ( 3.11)  $\omega = 2/(L_a\sqrt{3\pi})$  determines the transverse decay from the rod, and the radius of each rod is roughly equal to the half width of  $\eta$ ,  $\sqrt{\ln 2/2} \times \omega$ .

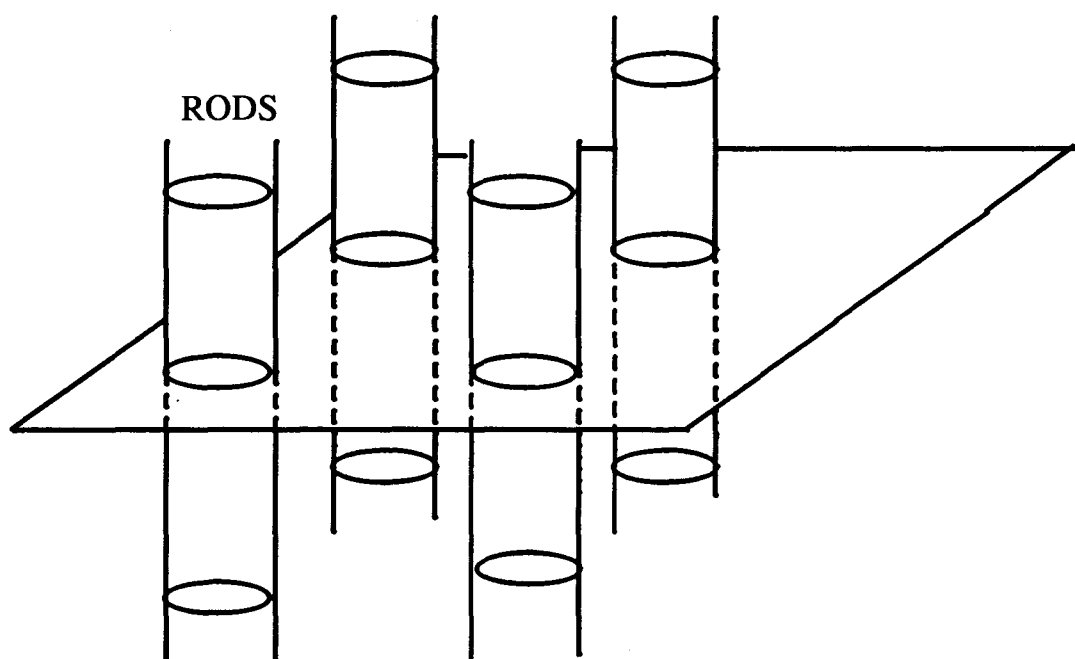


Figure 3.2: The reciprocal "lattice" of an ideal two dimensional graphite layer — a hexagonal array of rods

Consequently, the reciprocal "lattice" of an ideal two dimensional graphite layer with finite extent consists of a hexagonal array of rods, which is schematically shown in figure 3.2. The radius of each rod is only dependent on the size of layer, the larger the layer, the smaller the rod radius. However, this relation between the layer size and rod radius will alter when the layer deviates from the ideal structure i.e. when the layer is strained. In this case, the rod radius depends not only on the size of layer but also on the position ( $hk$ ) of the rod.

### 3.1.1 Strained Layer

In order to include the influence of layer strain on rod radius [35], we simply relax  $\omega$  by introducing a dimensionless refineable parameter  $\zeta$  to simulate in-plane strain [35, 39]. We let  $\omega \rightarrow \omega + \zeta s_0$ , at the same time maintaining the integrated scattering area in equation ( 3.11). Hence, the corresponding change in  $\eta$  is;

$$\eta(\vec{\epsilon}) \rightarrow \frac{L_a^2}{a^2} \frac{\omega}{\omega + \zeta s_0} e^{-|\vec{\epsilon}|^2 / (\omega + \zeta s_0)^2} \quad (3.12)$$

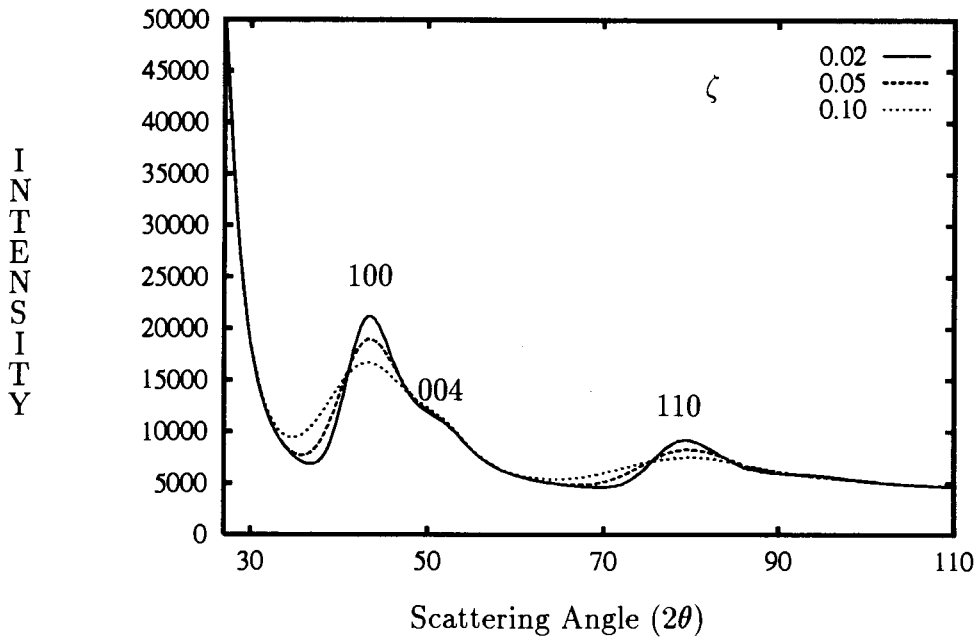


Figure 3.3: The Effect on X-ray intensity of strained layers

Equation ( 3.12) has a modified half width or radius,  $\sqrt{\ln 2/2}(\omega + \zeta s_0)$ , which depends on  $hk$  through  $s_0$ . Fig 3.3 shows a few X-ray diffraction patterns calculated from a strained layer stack (we will discuss how in the next section). We can see clearly how the in-plane strain changes the shapes of the (100) and (110) peaks,

which basically broadens the  $(hk0)$  peaks and has no effect on  $(00l)$  peaks. In what follows, we always implement the relaxed  $\eta$  expression.

## 3.2 Diffraction from Stacked Layers

We now consider a stack of  $M$  identical graphite layers arranged so that the layers are mutually parallel (see fig 3.4). As we pointed out above, each layer can be taken as a

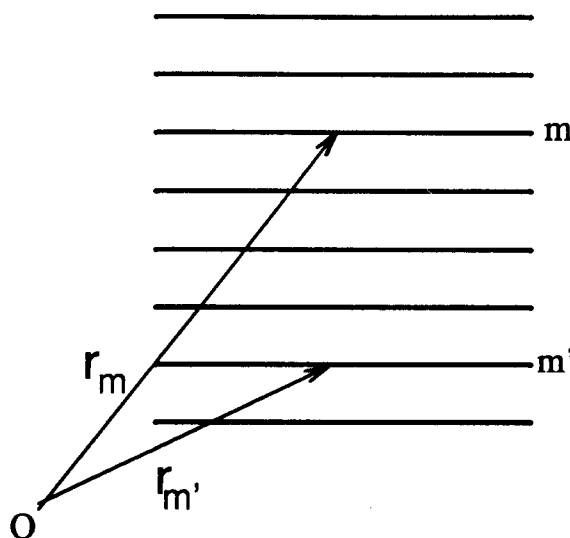


Figure 3.4: A  $M$  layer stack

giant unit which is then repeated in accordance with a given sequence along the stack direction. Let  $\vec{r}_m$  and  $\vec{r}_{m'}$  be real space vectors from the origin  $O$ , to two homologous points respectively in layers  $m$  and  $m'$ . The total amplitude of the beam diffracted by the entire stack can be expressed as

$$A(\vec{s}) = \sum_{m=1}^M \Phi(\vec{s}) e^{2i\pi\vec{s}\cdot\vec{r}_m} \quad (3.13)$$

The quantity  $(2\pi\vec{s}\cdot\vec{r}_m)$  is the difference in phase between the diffracted and incident waves. The diffraction intensity,  $i(\vec{s})$ , is:

$$i(\vec{s}) = |A(\vec{s})|^2 = |\Phi(\vec{s})|^2 \sum_{m=1}^M \sum_{m'=1}^M e^{2i\pi\vec{s}\cdot(\vec{r}_m - \vec{r}_{m'})} \quad (3.14)$$

where  $(\vec{r}_m - \vec{r}_{m'})$  is the relative translation between the  $n$ -th nearest neighbor layers  $m$  and  $m'$ . Introducing the  $n$ -th nearest neighbor vector  $\vec{r}_n = \vec{r}_m - \vec{r}_{m'}$ , and labeling  $n = |m - m'|$  we rearrange equation (3.14) to obtain

$$i(\vec{s}) = M|\Phi(\vec{s})|^2 \text{Re} \left( 1 + 2 \sum_{n=1}^{M-1} \frac{M-n}{M} e^{2i\pi\vec{s}\cdot\vec{r}_n} \right) \quad (3.15)$$

The vector  $\vec{r}_n$  may take on many values, each with a certain probability since we assume the stack is disordered. For a given  $n$ , assume that the allowed translation vectors are  $\vec{r}_{n_1}, \vec{r}_{n_2}, \dots, \vec{r}_{n_j}$  with respective probabilities

$$p_{n_1}, p_{n_2}, \dots, p_{n_j}. \quad (3.16)$$

For each pair of  $n$ -th nearest neighbors, the diffraction is therefore the mean of the interference corresponding to all possible configurations. Using the notation  $\langle \rangle$  for mean value we have,

$$\langle i(\vec{s}) \rangle = M \langle |\Phi(\vec{s})|^2 \rangle \left\{ 1 + 2 \text{Re} \left[ \sum_{n=1}^{M-1} \frac{M-n}{M} \langle e^{2i\pi\vec{s}\cdot\vec{r}_n} \rangle \right] \right\} = M \langle |\Phi(\vec{s})|^2 \rangle G \quad (3.17)$$

and

$$\langle e^{2i\pi\vec{s}\cdot\vec{r}_n} \rangle = \sum_j p_{n_j} e^{2i\pi\vec{s}\cdot\vec{r}_{n_j}} \quad (3.18)$$

$G$  is the so-called modulation or interference function for the crystal.

This notation separates the effects of the internal structure of the layer (through the factor  $\Phi$ ) and of the stacking sequence (through the factor  $G$ ) on the variation of the intensity of the diffracted wave. Let  $z_n$  be the component of  $\vec{r}_n$  perpendicular to the layer planes and let  $\vec{\Delta}_n$  be the projection of  $\vec{r}_n$  parallel to the layer plane. The translation  $\vec{\Delta}_n$  can be expressed in terms of the unit cell as follows,

$$\vec{\Delta}_n = \beta_n \vec{a}_1 + \gamma_n \vec{a}_2 \quad (3.19)$$

Thus the scalar product of  $\vec{r}_n \cdot \vec{s}$  is

$$\vec{r}_n \cdot \vec{s} = Zz_n + h\beta_n + k\gamma_n \quad (3.20)$$

and

$$G = 1 + 2\text{Re}\left[\sum_{n=1}^{M-1} \frac{M-n}{M} \langle e^{h\beta_n + k\gamma_n + Zz_n} \rangle\right] \quad (3.21)$$

The displacement  $\vec{r}_n$  of a layer with respect to its n-th neighbor is made up of the nearest neighbor displacements of all the intermediate layers  $\vec{r}_n = \Delta\vec{r}^n(1,2) + \Delta\vec{r}^n(2,3) + \dots + \Delta\vec{r}^n(n,n+1)$ , in which  $\Delta\vec{r}^n(i,i+1)$  represents displacement between adjacent layers  $i$  and  $i+1$  for a specific  $\vec{r}_n$ . Hence

$$\langle e^{2i\pi\vec{s}\cdot\vec{r}_n} \rangle = \langle \prod_{i=1}^n e^{2i\pi\vec{s}\cdot\Delta\vec{r}^n(i,i+1)} \rangle. \quad (3.22)$$

In general, the average above is difficult to obtain. However, if the stacking of each nearest neighbor pair is independent of neighboring layers, that is there is no correlation of nearest neighbor stacking vectors, then the average of the product is the product of the averages, and we have the results obtained by Mering [50]

$$\langle e^{2i\pi\vec{s}\cdot\vec{r}_n} \rangle = (\langle e^{2i\pi\vec{s}\cdot\Delta\vec{r}} \rangle)^n = q^n \quad (3.23)$$

Clearly,

$$q = \langle e^{2i\pi\vec{s}\cdot\Delta\vec{r}} \rangle = \sum_{k=1}^N p_k e^{2i\pi\vec{s}\cdot\Delta\vec{r}_k} \quad (3.24)$$

where  $\Delta\vec{r}_k$  is one of the N possible translations between *first-neighbor* layers. This uncorrelated translation approximation makes the sum of the geometric series in (3.21) trivial; we obtain

$$G = 1 + 2\text{Re}\left[\sum_{n=1}^{M-1} \frac{M-n}{M} q^n\right] = \text{Re}\left[\frac{1+q}{1-q} + \frac{2}{M} \frac{q^{M+1}-q}{(1-q)^2}\right] \quad (3.25)$$

and

$$i(\vec{s}) = M|\Phi(\vec{s})|^2 \text{Re}\left[\frac{1+q}{1-q} + \frac{2}{M} \frac{q^{M+1}-q}{(1-q)^2}\right] = M|\Phi(\vec{s})|^2 G(\vec{s}) \quad (3.26)$$

Equation (3.26) is the basis of our following discussions and from now on the average symbols  $\langle \rangle$  around  $i(\vec{s})$  will be implied. The nature of the disorder is completely

determined by the probability  $p_k$  and its associated shift vectors  $\Delta\vec{r}_k$ , which in turn determine, through equation (3.24), the wave vector dependence  $q$ . An explicit stacking model will be discussed in detail in the next chapter. During the derivation of these equations, we associated  $\Phi$  with the scattering amplitude from one single layer. However,  $\Phi(\vec{s})$  in the above equations could represent the scattering amplitude from a rigid two layer package or from any combination of several layers. Thus our treatment is not limited to the one layer model, which is self-evident. We will return to this topic when we deal with graphitic carbons.

### 3.2.1 G Averaging

As defined,  $G(s)$  will be peaked at  $(00l)$  reciprocal lattice points and also at harmonics in between the reciprocal lattice points, which are a result of a sharp cutoff in real space of the summations in (3.21). These harmonics are for most part unimportant but can cause problems near the  $(002)$  reflection which is very strong in many carbons. The harmonics are to our knowledge never observed in powder experiments, presumably because of the distribution in particle size present in any real sample.

We can emulate this situation in our calculation by assuming a Gaussian distribution of stacking size centered at  $M_0$

$$P(M) = \frac{1}{\sigma_M \sqrt{2\pi}} e^{-\frac{1}{2} \left[ \frac{M-M_0}{\sigma_M} \right]^2} \quad (3.27)$$

We now average  $G(s)$  over  $M$ , obtaining

$$\begin{aligned} \frac{1}{M_0} \langle MG(\vec{s}) \rangle_M &= \frac{1}{M_0} \int_{-\infty}^{\infty} P(M') M' G(\vec{s}) dM' \\ &= \text{Re} \left[ \frac{1+q}{1-q} + \frac{2}{M_0} \frac{q^{M_0+1} e^{[\sigma_M \ln q]^2 / 2} - q}{(1-q)^2} \right] \end{aligned} \quad (3.28)$$

This result is similar to equation (3.25) (We still use  $M$  instead of  $M_0$  in the following expressions for simplicity), the only modification being the exponential factor next to the  $q^{M+1}$  term. The choice of  $\sigma_M$  is somewhat arbitrary because any value  $\sigma_M > 2$ , essentially eliminates all harmonics without otherwise modifying the primary peaks. Therefore we have fixed  $\sigma_M = 2$  in our analysis. A graphical example of the

effect of averaging  $M$  on  $(00l)$  peaks is shown in Fig 3.5. The rule for implementing (3.28) will be discussed later below.

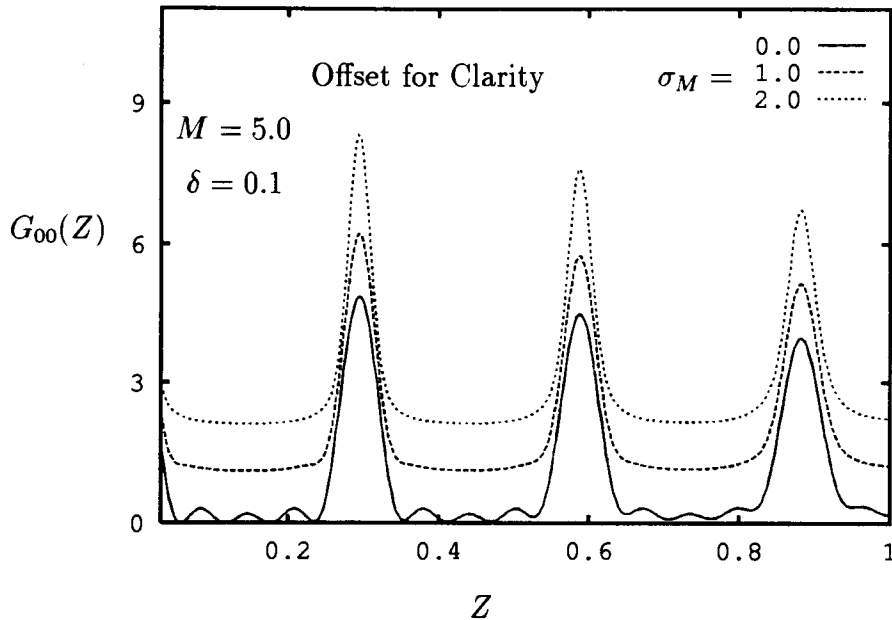


Figure 3.5: Showing how averaging over  $M$  removes the harmonics in  $G(Z)$  between the main  $(00l)$  reflections,  $Z$  is the length of the projection of  $\vec{s}$  along  $c$  axis.

### 3.3 Powder Averaging

All carbons studies in this work are poly-crystalline and we must calculate the powder average of (3.26) in order to make contact with experiment. The powder pattern can be built up using the Ewald construction. Figure 3.6 shows the intersection of an  $(hk)$  rod with the Ewald sphere of radius  $1/\lambda$ . The total powder intensity  $I(s)$ , at the tip of the vector  $\vec{s}$ , is the sum of the individual intensities  $i_{hk}(\vec{s})$  at the different points of intersection of the  $(hk)$  rods with the Ewald sphere at the end of vector  $\vec{s}$  when the reciprocal lattice is rotated in all directions around the origin  $O$ . This complicated



rotation can be simplified as shown by Brindley and Mering (1951)[30]. The same result can be obtained by keeping the reciprocal lattice fixed and considering the intersection of each  $(hk)$  rod with sphere centered on O.  $I(s)$  is obtained by increasing the radius  $s$  of the circle ( see figures 3.7 and 3.8). Therefore, for the  $hk$  rod considered, the powder intensity is an angular average in reciprocal space (see [51, 15])

$$I_{hk}(s) = \int i_{hk}(\vec{s})d\Omega = \int i_{hk}(\vec{s})\frac{dA}{4\pi s^2} \quad (3.29)$$

where  $d\Omega$  is the solid angle element, the integral is over a surface of the sphere of

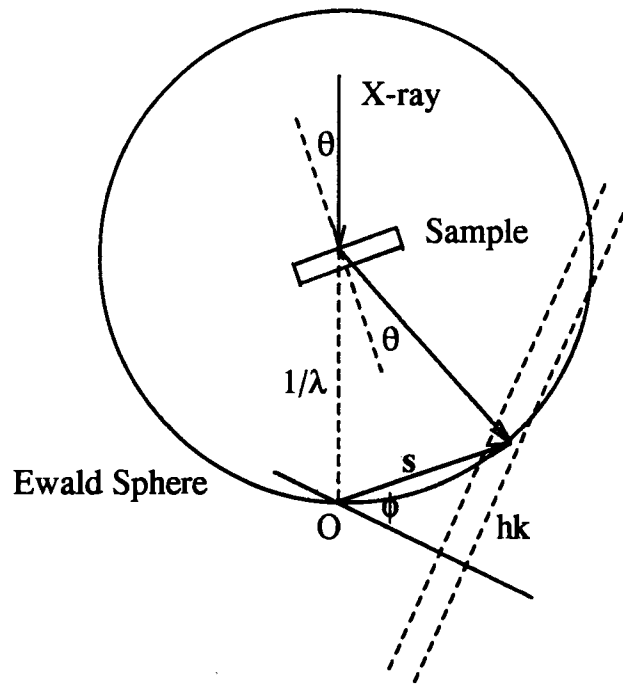


Figure 3.6: Ewald construction for building up powder intensity

radius  $s$ , and  $dA(\vec{s})$  is the corresponding surface element.  $i_{hk}(\vec{s})$  is given by ( 3.26). Such surface integrals were originally treated numerically by various authors [30, 52], but these methods would prove too cumbersome for a least squares refinement. Since the transverse scattering,  $\eta(\epsilon)^2$ , is only significant when  $\epsilon$  is small , the integration can be simplified by using the tangent cylinder approximation [30].

### 3.3.1 Tangent Cylinder Approximation (TCA)

For a given rod  $(hk)$  the sphere of radius  $s$  is replaced by a cylinder with the same radius, whose cylinder axis is in the basal plane and perpendicular to the vector  $\vec{s}_0 = h\vec{b}_1 + k\vec{b}_2$ , as shown in figures 3.6 and 3.7.

Looking down on the rod, the sphere appears as a circular arc, and near the rod can be approximated with a straight line. The angular integral is now transformed to a new basal plane coordinate system

$$\begin{aligned}\vec{u} &= \frac{1}{s_0}[h\vec{b}_1 + k\vec{b}_2] \\ \vec{v} &= \frac{1}{s_0}[-(2k+h)/\sqrt{3}\vec{b}_1 + (2h+k)/\sqrt{3}\vec{b}_2]\end{aligned}\quad (3.30)$$

where the  $\vec{u}$  is parallel to  $\vec{s}_0$  and  $\vec{v}$  is perpendicular to  $\vec{s}_0$  and defines the cylinder axis. In this new coordinate system we approximate the scattering vector

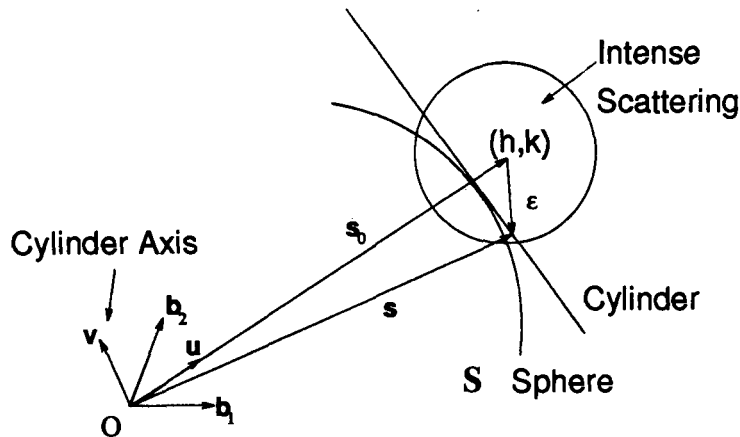


Figure 3.7: The tangent cylinder approximation (top view)

$$\vec{s} \simeq (s\cos\varphi, V, s\sin\varphi) \quad (3.31)$$

and

$$\vec{e} = (s\cos\varphi - s_0, V) \quad (3.32)$$

where  $\varphi$  is the angle between  $\vec{s}$  and the basal plane. The approximation (3.31) is exact when  $\vec{s}$  is collinear with  $\vec{s}_0$ . Using  $dA = sdV d\varphi$  for a cylinder surface element, The integral (3.29) now has the form

$$I_{hk}(s) = \frac{1}{4\pi s} \int d\varphi \int dV i_{hk}(s, V, \varphi) = \frac{M}{4\pi s} F(s)^2 \int d\varphi G_{hk}(\varphi) \int \eta(s, V, \varphi)^2 dV \quad (3.33)$$

Using the gaussian form of  $\eta^2$  and defining a new function  $T(s, \varphi)$

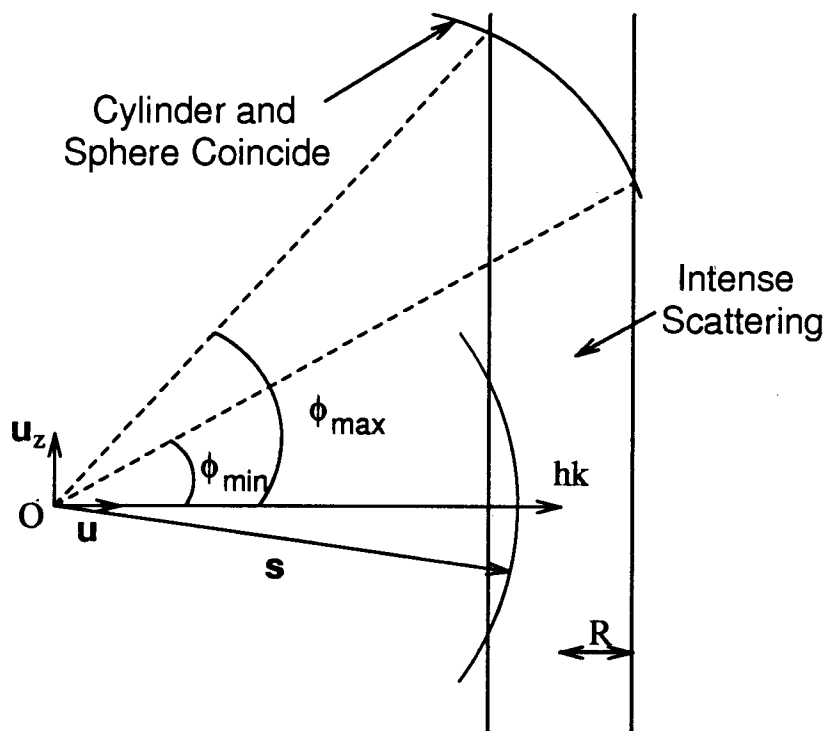


Figure 3.8: The tangent cylinder approximation (view along cylinder axis)

$$T(s, \varphi) = \int_{-\infty}^{\infty} \eta^2(s, V, \varphi) dV = \sqrt{\frac{\pi}{2}} \frac{L_a^4}{a^4} \frac{\omega^2}{\omega + \zeta s_0} e^{-2(s \cos \varphi - s_0)^2 / (\omega + \zeta s_0)^2} \quad (3.34)$$

where we use the relation  $|\vec{e}|^2 = ((s \cos \varphi - s_0)^2 + V^2)$ , then we can express  $I_{hk}$  as the following

$$I_{hk}(s) = \frac{1}{4\pi s} \int_{\varphi_{\min}}^{\varphi_{\max}} d\varphi G_{hk}(s, \varphi) T(s, \varphi) \quad (3.35)$$

The powder average has now been reduced to a one-dimensional integral over  $\varphi$ , which we can treat numerically (this is a time consuming calculation). However for the  $h = k = 0$  rod,  $s_0 = 0$ , this becomes simpler and we approximate the integral with

$$\int d\varphi = \sqrt{\pi/2} \frac{\omega + \zeta_{s_0}}{s} G_{00}(s, \pi/2) \quad (3.36)$$

which will speed up the calculation for the 00 rod significantly when we implement it in a refinement program. For the  $hk$  rods we must consider how, or if, the sphere of radius  $s$  intersects the rod. The intensity in the rod has a width (standard deviation),  $\sigma = \sqrt{\ln 2/2}(\omega + \zeta_{s_0})$ , and we will integrate three standard deviations on each side of the rod, which includes 99% of the scattered intensity. Thus we have three distinct cases

1.  $s < s_0 - 3\sigma$  ; the scattering sphere has no intersection with ( $hk$ ) rod and the integral is zero.
2.  $s_0 - 3\sigma < s < s_0 + 3\sigma$  ; the scattering sphere has complete intersection with the ( $hk$ ) rod. The integral limits will be

$$-\text{Arccos}\left[\frac{s_0 - 3\sigma}{s}\right] < \phi < \text{Arccos}\left[\frac{s_0 - 3\sigma}{s}\right]$$

3.  $s > s_0 + 3\sigma$  ; the scattering sphere cuts through the rod in two distinct regions which must be evaluated separately because the intensity along the rod is not always symmetric about  $Z = 0$  for the two layer model. Here the integration limits are

$$\text{Arccos}\left[\frac{s_0 - 3\sigma}{s}\right] > \phi > \text{Arccos}\left[\frac{s_0 + 3\sigma}{s}\right]$$

and

$$-\text{Arccos}\left[\frac{s_0 - 3\sigma}{s}\right] < \phi < -\text{Arccos}\left[\frac{s_0 + 3\sigma}{s}\right]$$

### 3.3.2 Debye Scattering Equation

How accurate will this tangent cylinder approximation be in a practical calculation of powder intensity? To examine the effectiveness of the TCA, it is worth comparing the TCA calculation with a rigorous calculation under the same conditions. Debye

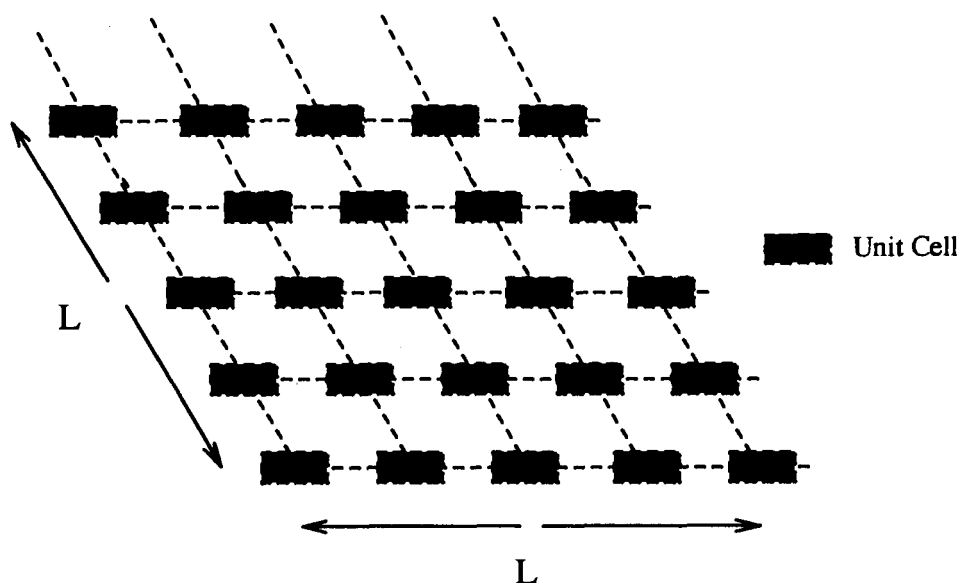


Figure 3.9: The Bravais lattice of a graphite layer. Each unit cell contains two carbon atoms

[53] has derived a well-known equation for calculating the powder averaged intensity of any arbitrary assembly of atoms. The intensity is given by,

$$I(s) = \frac{1}{N} \sum_{ij} f_i f_j \frac{\sin(2\pi s r_{ij})}{2\pi s r_{ij}} \quad (3.37)$$

where  $r_{ij}$  is the distance between  $i$ th and  $j$ th atom and  $f_i, f_j$  are the atomic scattering factors for  $i$ -th and  $j$ -th atom (for a graphite layer, all atomic scattering factors are the same), and  $N$  is total number of atoms. Equation (3.37) involves only the distance,  $r_{ij}$ , of each atom from every other atom. Therefore, as long as we can calculate the distance between any two atoms in the system, we can obtain the powder intensity.

The Debye model is difficult to apply to disordered carbons effectively. First, for a disordered system like carbon, it is difficult to evaluate the distance between each atom when turbostratic disorder and strain are included. Secondly, due to the limitation of the ability of contemporary computers, this method practically becomes almost impossible on a realistic size of atom group even if all interatomic distance are known.

To show that the TCA is an accurate approximation, we will compare the powder intensity for a small 2D graphite layer calculated using the exact Debye method and calculated using the TCA. The TCA is expected to become worse as the layer size becomes smaller, because the diameter of the reciprocal space rods gets larger. Since the Debye calculation works well for small layer size, this comparison will provide a good test of the TCA.

Since the distance between each atom in a graphite layer is easily worked out, the intensity calculation using the Debye equation is straightforward job. In the TCA calculation of a single graphite layer, the intensity expression in equation (3.35) becomes;

$$I_{hk}(s) = \frac{\alpha_{hk}^2}{4\pi s} \int \eta(s, V, \varphi)^2 d\varphi dV = \frac{\sqrt{\pi}\alpha_{hk}^2 L_a^4 \omega}{\sqrt{24}\pi s a^4} \int e^{-2(sc\cos\varphi - s_0)^2} \omega^2 d\varphi \quad (3.38)$$

where for the simplicity, we let the carbon atom scattering factor,  $f = 1$ . Fig 3.10 shows the comparison between the two calculations for  $11 \times 11$  and  $31 \times 31$  unit cells ( $L = 10 \times 2.46\text{\AA}$  and  $30 \times 2.46\text{\AA}$  respectively since  $a$  is  $2.46\text{\AA}$  for graphite).

As we mentioned in section 3.1, the layer width  $L$  only gives a rough estimate of  $L_a$  in our X-ray theory. The corresponding  $L_a$  in TCA can be calculated by fitting TCA calculation to that of the Debye model, which has been done by a small fitting program adjusting  $L_a$ , background and scale factor. The result shown in figure 3.10 is the comparison  $L_a$  for the two cases  $21.4\text{\AA}$  and  $57.44\text{\AA}$  respectively. The relation between  $L$  and  $L_a$  is determined roughly by the equal area rule. For example,  $L_a$  from an equal area disc ( $L_a \simeq 0.5L$ ) or square ( $L_a \simeq 0.93L$ ) is quite different (see figure 3.11). Between the disc and square, the constant will be between 0.5 and 0.93. This coefficient in reference [15] has been chosen to be  $1/1.2$ . On the other hand, the exact relation between  $L$  and  $L_a$  is not essential since  $L_a$  is a rough estimate of carbon

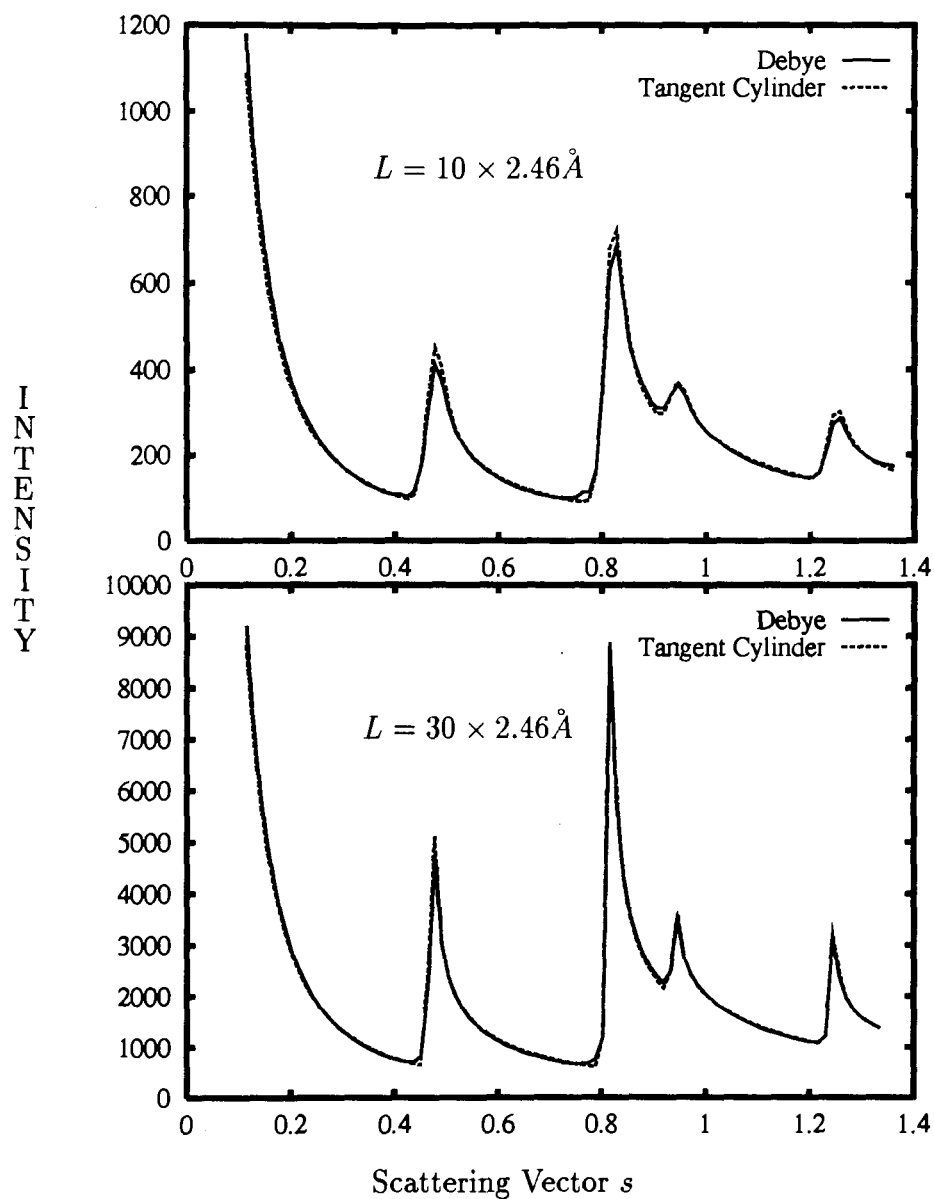


Figure 3.10: The comparison of the Debye calculation with that of the tangent cylinder approximation for a small size graphite layer.

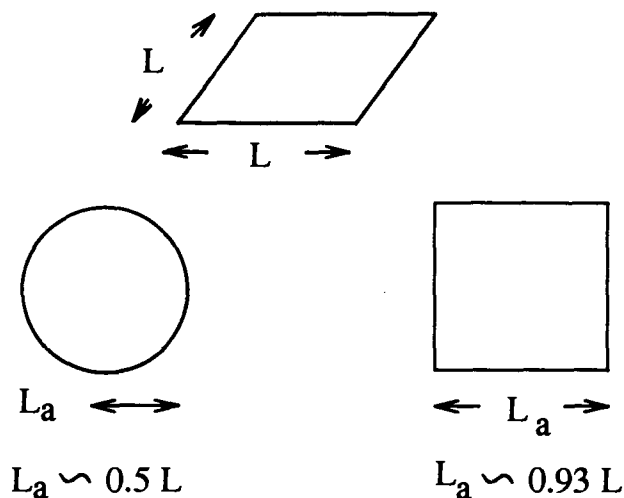


Figure 3.11: Equal area rule to determine  $L_a$  depending on the choice of polygon shape

layer size. The agreement between TCA and Debye calculations is quite acceptable. It should be noticed that the fit of  $30 \times 30$  is better than that of  $10 \times 10$  because of bigger layer size.

### 3.4 The Measured Intensity

To model the measured intensity in a quantitative fashion, a number of other important factors, such as absorption, sample thickness, polarization, thermal factor, preferred orientation etc., must be taken into account as follows.

#### 3.4.1 Absorption and Sample Thickness

The penetration of the X-rays into the carbon sample affects the position and shape of peaks, because X-rays scattering from particles below the sample surface are not strongly attenuated. This effect causes asymmetric Bragg peaks for thick samples.

The intensity of the incident X-ray beam in the carbon sample will decay as;

$$I(\theta, t) = I_0 e^{-\mu t / \sin(\theta)} \quad (3.39)$$



where  $\mu$  is the linear absorption coefficient,  $t$  is the depth within the sample and  $\theta$  is the incident angle. X-rays scattered from a carbon particle at depth  $t$  at the Bragg angle will be similarly attenuated by the carbon above. Thus the intensity of x-rays scattered from a layer of carbon particles of thickness  $dt$  at depth  $t$  will be reduced by a factor

$$e^{-2\mu t/\sin(\theta)} \tag{3.40}$$

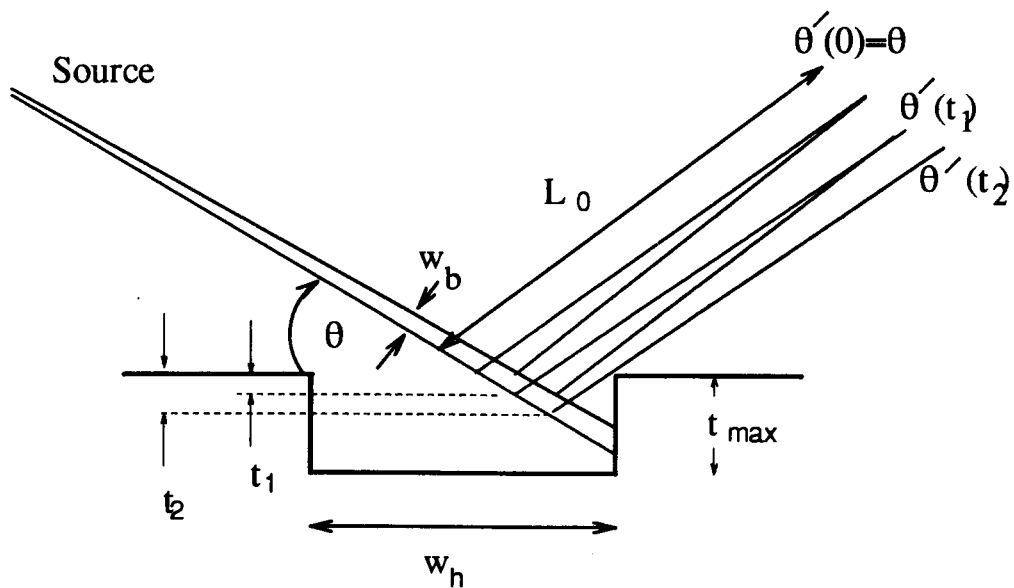


Figure 3.12: Schematically showing the sample holder and related parameters

compared to an identical layer of carbon at the sample surface. In addition, this layer of carbon of thickness  $dt$  at depth  $t$ , is displaced by a distance  $t$  from the goniometer axis. Assuming a divergent incident beam, pseudo focusing geometry and a detector arm using fixed receiving slits (which we have at SFU), the diffracted X-rays from *this* layer of carbon are observed at  $\theta'(t)$ , where

$$\theta'(t) = \theta - t\cos(\theta)/L_0. \tag{3.41}$$

$L_0$  is the goniometer radius. Thus, if  $I(\theta, 0)$  is the intensity of X-rays scattered at angle  $\theta$  by a carbon layer of thickness  $dt$  located at  $t = 0$ , then  $I(\theta, t) = I(\theta', 0)e^{-2\mu t/\sin(\theta)}$

is the intensity of x-rays diffracted through Bragg angle  $\theta$  by carbon at depth  $t$  which is measured at angle  $\theta'$ . Using equation ( 3.41) to solve for  $t$ , we obtain

$$I(\theta', t) = e^{-2\mu[L_0(\theta-\theta')]/\cos(\theta)\sin(\theta)} I(\theta, 0) \quad (3.42)$$

and for  $\theta' > \theta$ ,  $I(\theta') = 0$ . Thus to get the intensity of an infinitely thick sample, we convolute this expression with  $I(\theta)$  ( $I(s)$  is easily converted to  $I(\theta)$  using the definition of  $s$ ) given by equation ( 3.42). The absorption length of perfect graphite is only about  $9\text{cm}^{-1}$ , so samples of one or two millimeters depth are not thick enough to be considered infinitely deep.

To deal with finite depth samples, we introduce the sample depth,  $t_{max}$  such that  $I(\theta', t) = 0$  for  $t > t_{max}$ . In addition, at small Bragg angles, the incident x-ray beam will not penetrate all the way to the bottom of the sample holder if the width of the sample well is less than  $t_{max}/\sin(\theta)$ . A simple geometrical factor based on the dimensions of the sample holder,  $W_h$  and the width of the incident beam,  $W_b$ , is included to take this effect into account. Figure 3.12 shows the sample holder, incident and diffracted beams to show how the geometrical correction is developed. With reference to figure 3.12, there are 3 cases:

- a) when  $t < t_1$ , where  $t_1 = 0.5(W_h - W_b/2\sin\theta)\tan\theta$   
then  $I(\theta', t) = e^{-2\mu t/\sin(\theta)} I(\theta, 0)$ ;
- b) when  $t_1 < t < t_2$ , where  $t_2 = 0.5(W_h + W_b/2\sin\theta)\tan\theta$   
then  $I(\theta', t) = e^{-2\mu t/\sin(\theta)} I(\theta, 0)(t_2 - t)/(t_2 - t_1)$ ; and
- c) When  $t > t_{max}$ ,  $I(\theta', t) = 0$ .

Case (c) takes precedence over the other 2 cases. To calculate the resultant peak shape, we simply convolute our expression for  $I(\theta', t)$  with  $I(\theta)$  from equation 3.42. When the absorption is weak, we must take account of the effect of the sample configuration on the peak shapes. For all the calculations shown, we have assumed that the width of the beam,  $W_b$ , is 1.5mm, which corresponds to  $\frac{1}{2}$  degree divergence slits on the Philips diffractometer.

### 3.4.2 Polarization Factors

The polarization correction for monochromated X-rays is

$$P(\theta) = (1 + \cos^2(2\theta)\cos^2(2\theta_1))/2 \quad (3.43)$$

where  $\theta_1$  is monochromator angle, which for our machine is  $\theta_1 = 13.3^\circ$ .

### 3.4.3 Preferred Orientation and $00l$ Peaks

Some carbons consist of plate-like particles which will not orient themselves randomly when loaded in an x-ray sample holder. When the plates lie flat, the intensity of the  $00l$  reflections will be enhanced over  $hk0$  reflections. We account for this by inserting a preferred orientation correction in equation. ( 3.35)

$$po(\varphi) = e^{-PO\cos^2(\varphi)} \quad (3.44)$$

where  $PO$  is a refineable parameter. This has been shown by Ergun (1976) [35], to be effective.

### 3.4.4 Thermal Motion

The effects of thermal vibration are taken into account by including an isotropic temperature factor,  $B$ , as a refineable parameter. The scattering intensity is then attenuated by a factor

$$\exp\left(-2B\frac{\sin^2\theta}{\lambda^2}\right) \quad (3.45)$$

## 3.5 Summary

The total powder intensity corresponding to an experimental measurement should sum all the intensity from each rod in reciprocal space. However, when dealing with practical carbon X-ray profiles, the miller indices ( $kh$ ) are usually less than 3 because the highest scattering angle is limited to less than  $150^\circ$  normally. As a consequence, we only need to count the rods up to maximum  $h$  or  $k = 3$ . The rods that we count

with small  $hk$  are shown in figure 3.12. Referring to the figure, we write the final intensity expression used in our work with a brief explanation of each symbol used.

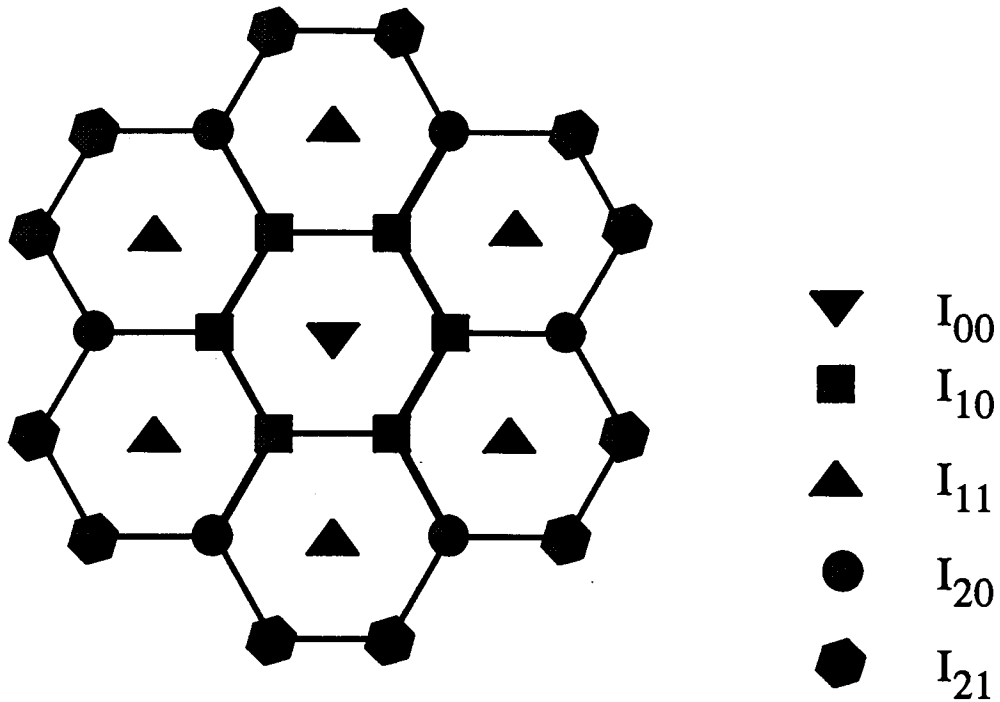


Figure 3.13: Showing the reciprocal rods with Miller index less than 3

$$I(\theta) = \int d\theta' I(\theta, \theta') / I_0(\theta) \times [I_{00}(\theta') + 6I_{10}(\theta') + 6I_{11}(\theta') + 6I_{20}(\theta') + 12I_{21}(\theta') + \dots] \quad (3.46)$$

and

$$I_{hk}(\theta) = I_{hk}(s) = \frac{M}{4\pi s} f(s)^2 \alpha_{hk}^2 \frac{L_a^4}{a^4} \frac{\omega^2}{\omega + \zeta_{s0}} \times P(\theta) e^{-B \sin^2(\theta)/\lambda^2} \int_{-\pi/2}^{\pi/2} d\varphi G_{hk}(s, \varphi) e^{-2(s \cos \varphi - s_0)^2 / (\omega + \zeta_{s0})^2} e^{-P O \cos^2(\varphi)} \quad (3.47)$$

where

$I(\theta)$  is the final calculated intensity which is directly

	comparable with experiment, within an arbitrary overall scale factor.
$I(\theta, \theta')/I_0(\theta)$	is the convolution function for the absorption and sample size correction.
$s$	is the magnitude of the scattering vector, $s = 2\sin(\theta)/\lambda$
$hk$	are Miller indices labeling a Bragg rod
$M$	is the average number of carbon layers stacked along the $z$ direction
$L_a$	is the average layer radius.
$f(s)$	is the atomic scattering factor for carbon.
$\alpha_{hk}$	is the unit cell structure factor for a single carbon layer.
$P(\theta)$	is the polarization correction.
$\zeta$	is a dimensionless in-plane strain parameter.
$B$	is the isotropic temperature factor.
$\varphi$	is the angle between the scattering vector, $\vec{s}$ , and basal plane.
$PO$	is the preferred orientation parameter.
$G_{hk}(s, \varphi)$	is the modulation function which takes turbostratic disorder, and strain along the $Z$ direction into account. (see equation 3.25)
$\vec{s}_0 = h\vec{b}_1 + k\vec{b}_2$	is the the reciprocal lattice vector for the $hk$ rod.

We have discarded the constant factor in equation (3.47) which can be absorbed in an over all scale factor during the analysis , and also divided by  $ML_a^2$ .

# Chapter 4

## Models and Algorithm

In the last two chapters, we have examined the structural model in detail and the general calculation of powder diffraction intensity of disordered carbons. In order to compute the intensity, a calculable expression for the phase factor  $q$  must be worked out first. In this chapter, we will evaluate  $q$  in different cases based on the random translation assumption described in chapter 2. Also, we explain the algorithm used in our fitting program, which basically closely follows the treatment in *Numerical Recipes*[16].

The modulation function  $G(\vec{s})$  in ( 3.26) has been expressed in terms of the average phase factor

$$q = \langle e^{2\pi i \vec{s} \cdot \Delta \vec{r}} \rangle \quad (4.1)$$

where  $\Delta \vec{r}$  is the translations vector between adjacent layers. For crystalline 2H graphite, two alternating registered translations are:  $\Delta \vec{r}_1 = \vec{v}_1 + d_{002} \hat{u}_z$  and  $\Delta \vec{r}_2 = \vec{v}_2 + d_{002} \hat{u}_z$ . The c-axis displacement between adjacent layers is  $d_{002} = c/2$ . For disordered carbons, though,  $\Delta \vec{r}$  is random. The c-axis displacement  $d_{002}$  is not fixed but changing as  $d_{002} + \delta$ , where  $\delta$  is usually small and random.

In order to average  $q$ , a probability distribution  $p(\Delta \vec{r})$  as a function of the translation vectors  $\Delta \vec{r}$  is needed. Theoretically,  $p(\Delta \vec{r})$  is a function depending on all three coordinates of  $\Delta \vec{r}$  ( two of them parallel to the layer, one perpendicular to the layer).

In our simple model, the detailed form of  $p(\Delta\vec{r})$  on the three coordinates is not needed.

To see how this happens, recall the random translation model for the one layer model first (see section 2.21), in which we have introduced a probability  $P$  to describe the probability of a random shift between adjacent layers. We assume that the registered shift vectors  $\Delta\vec{r}_1$  and  $\Delta\vec{r}_2$  are selected with equal probability in a random fashion. Then clearly, each of the two possible registered translations has the probability  $\frac{1}{2}(1 - P)$  to appear in the stacking. Therefore, equation (4.1) turns into

$$q = \frac{1}{2}(1 - P) \langle e^{2\pi i\vec{s}\cdot(\vec{v}_1+(d_{002}+\delta\hat{u}_z)} + e^{2\pi i\vec{s}\cdot(\vec{v}_2+(d_{002}+\delta\hat{u}_z)} \rangle + P \langle e^{2\pi i\vec{s}\cdot\Delta\vec{r}_{random}} \rangle \quad (4.2)$$

Since  $\langle e^{2\pi i\vec{s}\cdot\Delta\vec{r}_{random}} \rangle = 0$ , if all random translations are considered to have equal probability, we obtain

$$q = \frac{1}{2}(1 - P) \langle e^{2\pi i\vec{s}\cdot(\vec{v}_1+(d_{002}+\delta\hat{u}_z)} + e^{2\pi i\vec{s}\cdot(\vec{v}_2+(d_{002}+\delta\hat{u}_z)} \rangle \quad (4.3)$$

For graphitic carbons, we use the two layer model. In this case, one has three possible translations between adjacent layer packages as discussed in section 2.2.2 of chapter 2.

1. 3R type registered translation,  $\Delta\vec{r}_{3R} = 2\vec{v}_1 + (2d_{002} + \delta)\hat{u}_z$  with probability  $P_t$ ,
2. zero translation in the basal direction,  $\Delta\vec{r}_0 = (2d_{002} + \delta)\hat{u}_z$  with probability  $1 - P - P_t$ . (This leads to *ABABAB* or 2H stacking)
3. random translation  $\Delta\vec{r}_{random} = \vec{v}_{random} + (2d_{002} + \delta)\hat{u}_z$  with probability  $P$ .

where we assume that the translation between *A* and *B* within a package is  $\vec{v}_1 + d_{002}\hat{u}_z$ . Therefore, the corresponding equation (4.1) can be written as

$$q = (1 - P - P_t) \langle e^{2\pi i\vec{s}\cdot\Delta\vec{r}_0} \rangle + P_t \langle e^{2\pi i\vec{s}\cdot\Delta\vec{r}_{3R}} \rangle \quad (4.4)$$

where again the random term gives zero. From equations (4.3) and (4.4), we find that a probability distribution which only depends on  $\delta$  is enough for carrying out the average of the phase factor  $q$ . In the next sections, we will use the distribution for  $p(\delta)$  presented in chapter 2 to work out the average phase factor,  $q$ , for the one and two layer models respectively.

## 4.1 One layer model

We start with the simplest case,  $h = k = 0$ , that is, ignoring the basal effects and focusing on the c-axis disorder only. Since the basal related components are all equal to zero and  $\vec{s} = Z\hat{u}_z$ , equation (4.3) becomes,

$$q = (1 - P) \langle e^{2\pi i Z \cdot (d_{002} + \delta \hat{u}_z)} \rangle \quad (4.5)$$

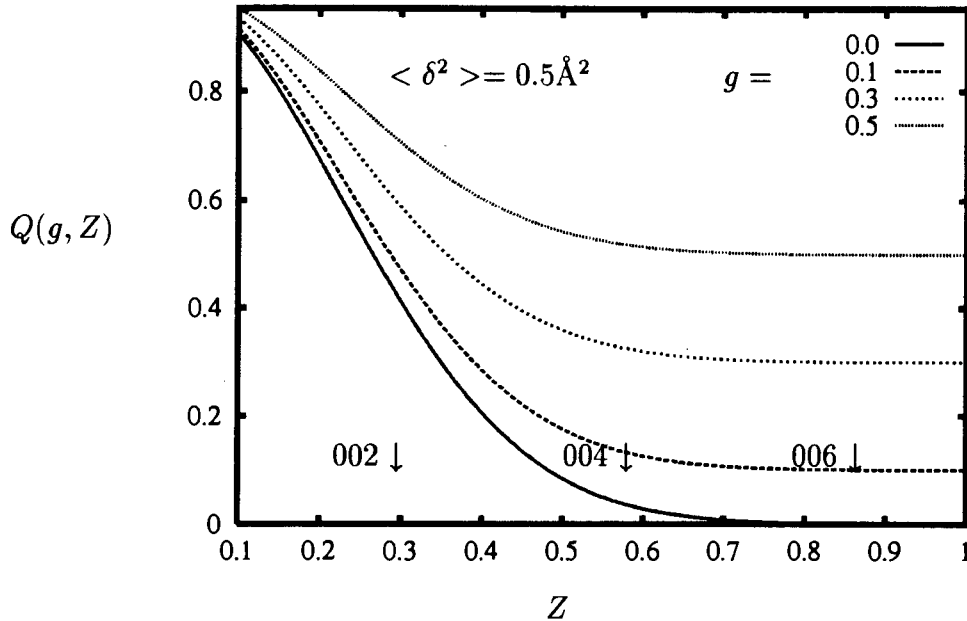


Figure 4.1: Showing the dependence of  $Q(g, Z)$  on  $g$  and  $Z$

The simple strain distribution,  $p(\delta)$ , described in chapter 2 will be used here for the averaging calculation,

$$p(\delta) = g\delta_D(\delta) + (1 - g) \frac{1}{\sqrt{2\pi \langle \delta^2 \rangle}} e^{-\frac{\delta^2}{2\langle \delta^2 \rangle}} \quad (4.6)$$

where  $g$  is the fraction of low strain regions in disordered carbons and its value is between 0 and 1 (refer to chapter 2 for details). The quantity  $\langle \delta^2 \rangle$ , given by



$$\langle \delta^2 \rangle = \int_{-\infty}^{+\infty} \delta^2 \frac{1}{\sqrt{2\pi \langle \delta^2 \rangle}} e^{-\delta^2/(2\langle \delta^2 \rangle)} d\delta, \quad (4.7)$$

is the mean squared fluctuation in c-axis spacing ( $\langle \delta \rangle = 0$ ). Substituting this into (4.5);

$$\begin{aligned} q &= (1 - P) \int_{-\infty}^{+\infty} \exp[2\pi i Z(d_{002} + \delta)] p(\delta) d\delta \\ &= (1 - P) e^{2\pi i Z d_{002}} (g + (1 - g) e^{-2\pi^2 Z^2 \langle \delta^2 \rangle}) \\ &= (1 - P) e^{2\pi i Z d_{002}} Q(g, Z) \end{aligned} \quad (4.8)$$

where the function  $Q(g, Z)$  is basically a kind of Fourier transform of  $p(\delta)$ . Figure 4.1 shows how  $Q$  depends on  $g$  and  $Z$ .

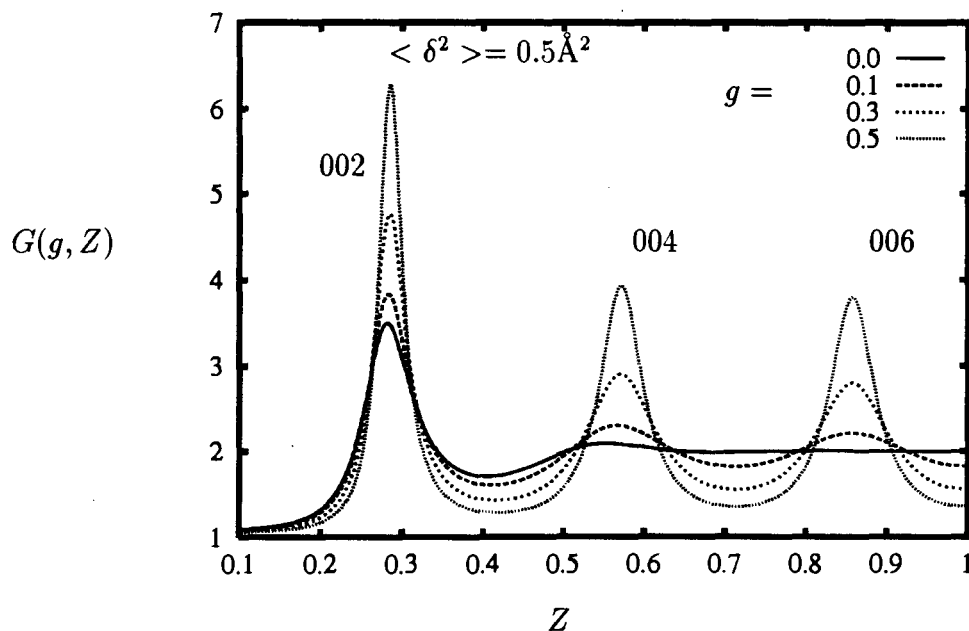


Figure 4.2: Showing how  $G$  depends on  $g$  and  $Z$ , for  $M = 20$  and  $d_{002} = 3.5 \text{ \AA}$ , with  $\langle \delta^2 \rangle = 0.5 \text{ \AA}^2$

It is easily seen from figure 4.1 that when  $g = 0$  and  $\langle \delta^2 \rangle$  is large,  $Q(g, Z)$  decreases so quickly that the (004), (006) peaks etc. are smeared out due to the big  $\langle \delta^2 \rangle$ . Large  $\langle \delta^2 \rangle$  is often needed to fit the (002) peak shape. Consequently,  $g$  plays an important role for highly strained carbons in slowing down the exponential decay and preventing the (004) and (006) etc. peaks from disappearing. Figure 4.2 shows the effect of  $g$  on  $G(q, Z)$ .

The calculation for  $h$  or  $k \neq 0$  is trivial; equation (4.7) is multiplied by a phase factor,  $\cos[\frac{2}{3}\pi(h - k)]$ , from the basal translations. Hence the final average phase for the one layer model is

$$q = \{P\delta_{h0}\delta_{k0} + (1 - P)\cos[\frac{2}{3}\pi(h - k)]\}e^{2\pi i Z d_{002}}Q(g, Z) \quad (4.9)$$

where  $\delta_{ij}$  is the Kronecker delta symbol.

When either  $P$  or  $\delta$  becomes large, the magnitude of  $q$ ,  $|q|$ , may become (subject to  $hk$ ) negligible. The resulting singularity in the logarithm of equation (3.28) for the average over crystal sizes, can cause problems during the calculations. However, when either  $P$  or  $\delta$  is large, the harmonics in the modulation function are no longer present anyway, and averaging over  $M$  becomes unnecessary. Therefore we only apply equation (3.28) when  $|q| > \frac{1}{2}$ , otherwise the un-averaged version, equation (3.25), is used in the calculation.

## 4.2 Two Layer Model

A similar calculation for the two layer model will be carried out in this section. For graphitic carbons, the highly strained areas are negligible, therefore a simple Gaussian distribution with a small width  $\sqrt{\langle \delta^2 \rangle}$  is good enough to model the layer spacing fluctuation. The Gaussian distribution is,

$$p(\delta) = \frac{1}{\sqrt{2\pi \langle \delta^2 \rangle}} e^{-\frac{\delta^2}{2\langle \delta^2 \rangle}} \quad (4.10)$$

The average of  $q$  using this function is

$$q = \{P\delta_{h0}\delta_{k0} + 1 - P + P_t[e^{4i\pi(\frac{1}{3}h + \frac{2}{3}k)} - 1]\}e^{4\pi i Z d_{002} - 2\pi^2 \langle \delta^2 \rangle Z^2} \quad (4.11)$$

For the two layer model, we also have to modify the scattering amplitude of one layer,  $\Phi(\vec{s})$ , into that of the two layer package,  $\Phi'(\vec{s})$ , which appears in the intensity formula in the form of  $|\Phi'(\vec{s})|^2$  (two layer model) or  $|\Phi(\vec{s})|^2$  (one layer model). According to the definition of the scattering amplitude, the relation between  $|\Phi'(\vec{s})|^2$  and  $|\Phi(\vec{s})|^2$  is as follows

$$\Phi'(\vec{s}) = \sum_1^2 \Phi_m(\vec{s}) e^{2\pi i \vec{s} \cdot \vec{R}_m} = \Phi_m(\vec{s}) (1 + e^{2\pi i \vec{s} \cdot (\vec{a}_1/3 + 2\vec{a}_2/3 + d_{002} \hat{u}_z)}) \quad (4.12)$$

which gives

$$|\Phi'(\vec{s})|^2 = 4|\Phi(\vec{s})|^2 \cos^2 \pi \left( \frac{1}{3}h + \frac{2}{3}k + Zd_{002} \right) \quad (4.13)$$

### 4.3 Comparing the Two Models

Next, we are going to examine the effect of  $P$  and  $P_t$ , which describe turbostratic and 3R-type disorder respectively, on the intensity. It is time for us to compute the total intensity since we have worked out the complete expressions for  $q$  and  $|\Phi'(\vec{s})|^2$ . Let us first look at the difference in intensity between the one layer model and the two layer model. Fig 4.4 compares diffraction profiles calculated by the two models. We use  $d_{002} = 3.38\text{\AA}$ ,  $a = 2.46\text{\AA}$ ,  $L_a = 200\text{\AA}$ ,  $g = 0$ ,  $L_c = 150\text{\AA}$ ,  $P_t = 0$ ,  $\delta = 0.01\text{\AA}$ ,  $\mu = 2.0$ , and  $g = 1$ . Figure 4.3(a) shows results for four different choices of  $P$  calculated using the one layer model. Figure 4.3 (b) shows results for three corresponding choices of  $P$  using the two layer model. The major differences between the models are as follows:

1. At large  $P$ , the two layer model cannot reproduce the 2-dimensional line shape expected for the (100) peak of a completely turbostratic carbon.
2. At small  $P$ , the single layer model cannot reproduce the (102) and (103) peaks observed in more crystalline graphites while the 2-layer model can. The shape of the (100)/(101) region is also more accurately reproduced for graphitic carbons by the two-layer model.

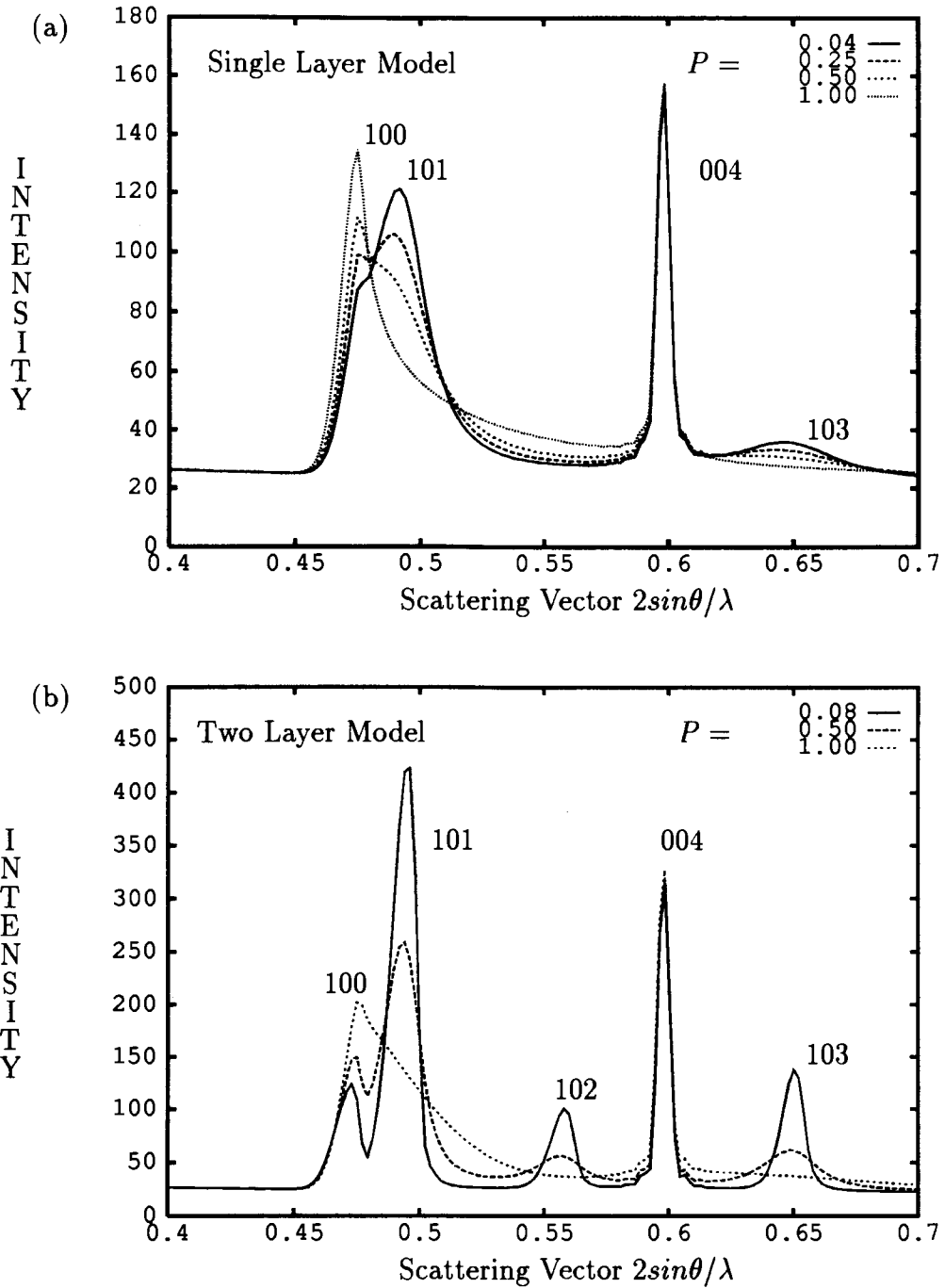


Figure 4.3: The comparison of one layer model with two layer model by changing  $P$

Figure 4.4 shows diffraction profiles calculated with the two layer model for selected values of  $P$  and  $P_t$ . Both  $P_t$  and  $P$  can broaden the (102) and (103) peaks, but they have a completely different effect on the (111) peaks.  $P_t$  has no effect at all on (110) and (112) (see figure 4.4 (a)), and  $P$  only broadens the (112) peak and does not affect the (110) peak as  $P$  increases (see figure 4.4 (b)). Why is this?  $P$  and  $P_t$  should affect 3D mixing peaks like (101) and (111) etc. The reason why  $P_t$  has no effect on the (111) peaks can be seen by looking at the expression for  $q$  in (4.12). When  $h = k = 1$ , the term containing  $P_t$  cancels out so  $P_t$  cannot affect  $G$ . The calculations presented in figure 4.4, used  $d_{002} = 3.38\text{\AA}$ ,  $a = 2.46\text{\AA}$ ,  $L_a = 200\text{\AA}$ ,  $L_c = 270\text{\AA}$  ( $M = 80$ ) and  $\delta = 0.01\text{\AA}$ .

## 4.4 Levenberg-Marquardt Method

In this section we will illustrate the mathematical algorithm and programming techniques involved to implement the structure refinement program. Basically we follow the treatment in *Numerical Recipes* edited by William H. Press *et. al* [16].

Generally speaking, the procedure to fit a set of data to a *model* that depends on a set of adjustable parameters is always the same: (1) choosing or designing a merit function that measures the agreement between data and calculation; (2) adjusting the model parameters to achieve a minimum in the merit function, that is, finding best-fit parameters. Conventionally, smaller values of the merit function represent closer agreement. The toughest part is the process of the adjustment, which is intrinsically a problem of minimization in multi-dimensional space.

### 4.4.1 Least Square Merit Function

The first question is how to define the merit function for measuring the agreement between data and model. Mathematically, this is called a problem of *maximum likelihood estimation*. The best merit function for most problems is the least square form [16],

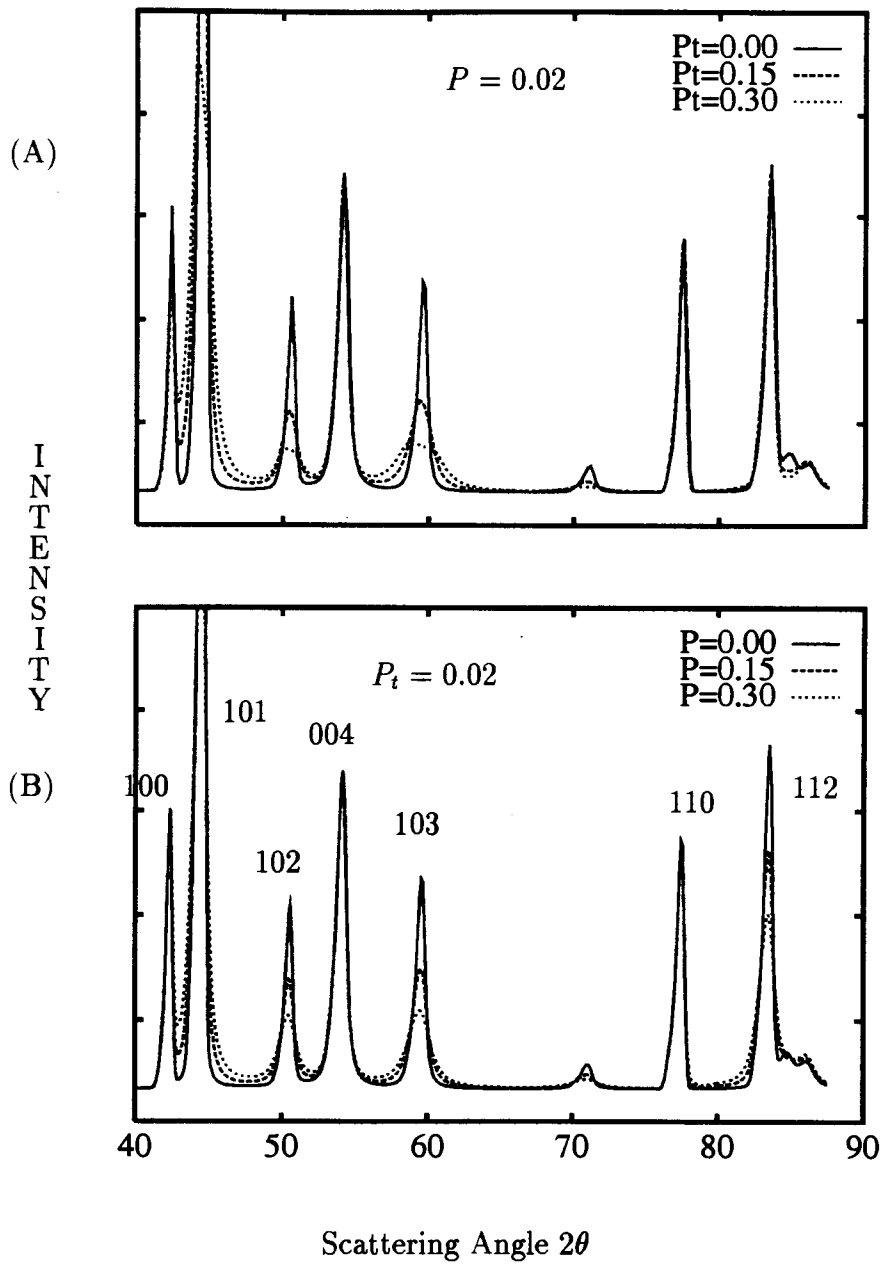


Figure 4.4: Comparing the intensities calculated with the two layer model at different selected  $P$  and  $P_t$

$$\chi^2(\vec{a}) = \sum_{i=1}^N \left[ \frac{I_i - I(s_i; \vec{a})}{\sigma_i} \right]^2 \quad (4.14)$$

where  $I(s_i, \vec{a})$  is a formal function for calculating the data at  $s_i$ , which depends on the parameter vector  $\vec{a}$  and probably does not have an analytic expression in most cases.  $I_i$  and  $\sigma_i$  are data and error measured at  $s_i$ .

#### 4.4.2 How To Minimize A Nonlinear Model

$I(s_i, \vec{a})$  used in our model is a strongly nonlinear function of the parameters  $a_k$ ,  $k = 1, 2, \dots, m$ , and there is no analytic formula to present. To minimize such a nonlinear problem by adjusting the parameters, an iterative method is appropriate. An effective iterative procedure must be able to improve the trial solution each time, that is, lower  $\chi^2$  until the decrease of  $\chi^2$  stops or effectively stops. Theoretically, if the parameters are sufficiently close to the minimum, one can approximate  $\chi^2$  by a quadratic form, that is;

$$\chi^2(\vec{a}) = \gamma - \vec{d} \cdot \vec{a} + \frac{1}{2} \vec{a} \cdot [\vec{D}] \cdot \vec{a} \quad (4.15)$$

$\vec{d}$  is an N-vector and  $[\vec{D}]$  is an  $m \times m$  matrix and  $\gamma$  is a constant. If the approximation is good, then the minimizing problem becomes standard, and  $\vec{a}_{min}$  can be found from the current trial parameter  $\vec{a}_{cur}$  by

$$\vec{a}_{min} = \vec{a}_{cur} + [D]^{-1} \cdot [-grad\chi^2(\vec{a}_{cur})] \quad (4.16)$$

However, ( 4.15) may be a poor local approximation to the shape of the function that we are trying to minimize at  $\vec{a}_{cur}$ . In this case, all we can do is to take a step down the gradient in the steepest descent direction, that is;

$$\vec{a}_{next} = \vec{a}_{cur} - constant \times grad\chi^2(\vec{a}_{cur}) \quad (4.17)$$

where we must choose a small enough constant to guarantee that we do not exhaust the downhill direction. To use equations ( 4.16) or ( 4.17), the gradient and the second

derivative matrix  $[D]$  (Hessian matrix) of the  $\chi^2$  function must be computed at any arbitrary set of parameters  $\vec{a}$ .

### 4.4.3 Gradient and Hessian Matrices

Let us take a close look at the gradient and Hessian matrices here. For this purpose, we introduce two new variables to simplify the notation. The first one is half of the negative gradient of  $\chi^2$  with respect to each of parameters

$$\beta_k = -\frac{1}{2} \frac{\partial \chi^2}{\partial a_k} = \sum_{i=1}^N \frac{I_i - I(s_i; \vec{a})}{\sigma_i} \frac{\partial I(s_i; \vec{a})}{\partial a_k} \quad (4.18)$$

The second is half of the second derivatives of  $\chi^2$ ,

$$\alpha_{kl} = \frac{1}{2} \frac{\partial^2 \chi^2}{\partial a_k \partial a_l} = \sum_{i=1}^N \frac{1}{\sigma_i^2} \left[ \frac{\partial I(s_i; \vec{a})}{\partial a_k} \frac{\partial I(s_i; \vec{a})}{\partial a_l} - [I_i - I(s_i; \vec{a})] \frac{\partial^2 I(s_i; \vec{a})}{\partial a_k \partial a_l} \right] \quad (4.19)$$

The matrix  $[\alpha]$  is usually called the *curvature matrix*. Note that the components  $\alpha_{kl}$  of the Hessian matrix (4.19) depend both on the first derivatives and on the second derivatives of  $\chi^2$ . However, the second derivative terms can be dismissed. The reason is that these terms are all multiplied by the random number  $[I_i - I(s_i; \vec{a})]$ . Therefore, the sum of the second derivative terms tend to cancel out eventually [16]. Hence the Hessian matrix can be simplified as;

$$\alpha_{kl} = \sum_{i=1}^N \frac{1}{\sigma_i^2} \left[ \frac{\partial I(s_i; \vec{a})}{\partial a_k} \frac{\partial I(s_i; \vec{a})}{\partial a_l} \right] \quad (4.20)$$

It can be shown that this approximation for  $[\alpha]$  has no effect at all on what final set of parameters  $\vec{a}$  is reached, but only affects the iterative route that is taken in getting there [16]. The condition when  $\chi^2$  is a minimum, that is,  $\beta_k = 0$  for all  $k$ , is independent of how  $[\alpha]$  is defined.

As a consequence, in terms of  $\alpha$  and  $\beta$ , when equation (4.16) becomes a set of linear equations

$$\sum_{l=1}^M \alpha_{kl} \delta a_l = \beta_k \quad (4.21)$$



From this equation, we can evaluate the increments  $\delta a_l$  ( $\vec{a}_{cur} - \vec{a}_{min}$ ) given  $\alpha$  and  $\beta$ , then add it to the current approximation giving the next approximation. Equation ( 4.17), the steepest descent formula, can also be written as

$$\delta a_l = constant \times \beta_l \quad (4.22)$$

where the *constant* is a function of  $l$ .

#### 4.4.4 Adjusting Parameters

Up to now, we still do not know when we should use the inverse-Hessian matrix (equation ( 4.16)) or the steepest descent method (equation ( 4.17)). Fortunately, we do not have to make such a decision in practice. Levenberg and Marquardt have found an elegant way [54] to smoothly unify the two methods. This method, called the Levenberg-Marquardt method, works very well in practice and has become the standard of nonlinear least-squares routines.

The method is based on two elementary, but important, insights. Consider the *constant* in equation ( 4.17). What is the order of magnitude? There is no information about it. The gradient tells only the slope, not how far the slope extends. Levenberg-Marquardt's first insight is that the components of Hessian matrix really imply some information about the order-of-magnitude scale of the problem, that is  $1/\alpha_{kk}$ , the reciprocal of the diagonal element.<sup>1</sup> Therefore they replace equation ( 4.17) by

$$\delta a_l = \frac{1}{\lambda \alpha_{ll}} \beta_l \quad (4.23)$$

where  $\lambda$  is a dimensionless constant to slow down the step. Levenberg-Marquardt's second insight is to introduce a new matrix  $[\alpha']$ ,

---

<sup>1</sup>The argument is:  $\chi^2$  is dimensionless quantity, which is evident from its definition. On the other hand,  $\beta_k$  has the dimensions of  $1/\alpha_k$ , which have units like  $\text{cm}^{-1}$ , or whatever. (In fact, each component of  $\beta_k$  can have different dimensions!) As to the constant of proportionality between  $\beta_k$  and  $\alpha_k$ , there is one obvious quantity with these dimensions, that is,  $1/\alpha_{kk}$ , the reciprocal of the diagonal element, which sets the scale of the constant. But that scale might itself be too big. So let's divide the constant by some (dimensionless) factor  $\lambda$ , with the possibility of setting  $\lambda \gg 1$  to cut down the step.

$$\begin{aligned} [\alpha'_{jj}] &= [\alpha_{jj}](1 + \lambda) \\ [\alpha'_{jk}] &= [\alpha_{jk}] \end{aligned} \quad (4.24)$$

to combine ( 4.16) and ( 4.17) into one equation.

$$\sum_{l=1}^M [\alpha'_{kl}] \delta a_l = \beta_k \quad (4.25)$$

When  $\lambda$  is very large, the matrix  $\alpha'$  is forced into being diagonally dominant, so equation ( 4.25) turns out to be identical to ( 4.17). On the other hand, as  $\lambda$  approaches zero, equation ( 4.25) goes over to ( 4.16). As a result, given an initial guess of parameters  $\vec{a}$ , the Levenberg-Marquardt recipe can be summarized as follows:

1. Compute  $\chi^2(\vec{a})$
2. (\*) Solve the linear equations ( 4.25) for  $\delta\vec{a}$  and evaluate  $\chi^2(\vec{a} + \delta\vec{a})$ .
3. If  $\chi^2(\vec{a} + \delta\vec{a}) > \chi^2(\vec{a})$ , increase  $\lambda$  by a factor of 10 (or any other substantial factor) and go back to (\*)
4. If  $\chi^2(\vec{a} + \delta\vec{a}) < \chi^2(\vec{a})$ , decrease  $\lambda$  a factor 10, update the trial solution  $\vec{a} \leftarrow \vec{a} + \delta\vec{a}$ , and go back to (\*)

It is common to find the parameters wandering around near the minimum in a flat valley of complicated topology. The reason is that Levenberg-Marquardt's method simply generalizes the method of normal equations, hence has the same problem when near to the degeneracy of the minimum. Outright failure by a zero pivot is possible, but unlikely. For sufficiently large  $\lambda$  the matrix  $[\alpha']$  is positive definite and can have no small pivots. Thus the method does tend to stay away from zero pivots, but at the cost of a tendency to wander around doing steepest descent in very un-step degenerate valleys.

In our practical refinement program, we stop the program on the first occasion that  $\chi^2$  decreases by a negligible amount, say  $10^{-3}$ , to prevent such wandering, and

don't stop after a step where  $\chi^2$  increase. Besides, we have made a simple program to estimate the initial trial parameters  $\vec{a}_{ini}$  to make sure that  $\vec{a}_{ini}$  is already close to  $\vec{a}_{min}$  precluding the program from going crazy due to the nonlinear behavior. Finally, once the acceptable minimum has been found, one needs to set  $\lambda = 0$  to compute  $\vec{a}_{min}$ . The process to get  $a_{min}$  is shown by program flow diagram in figure 4.6.

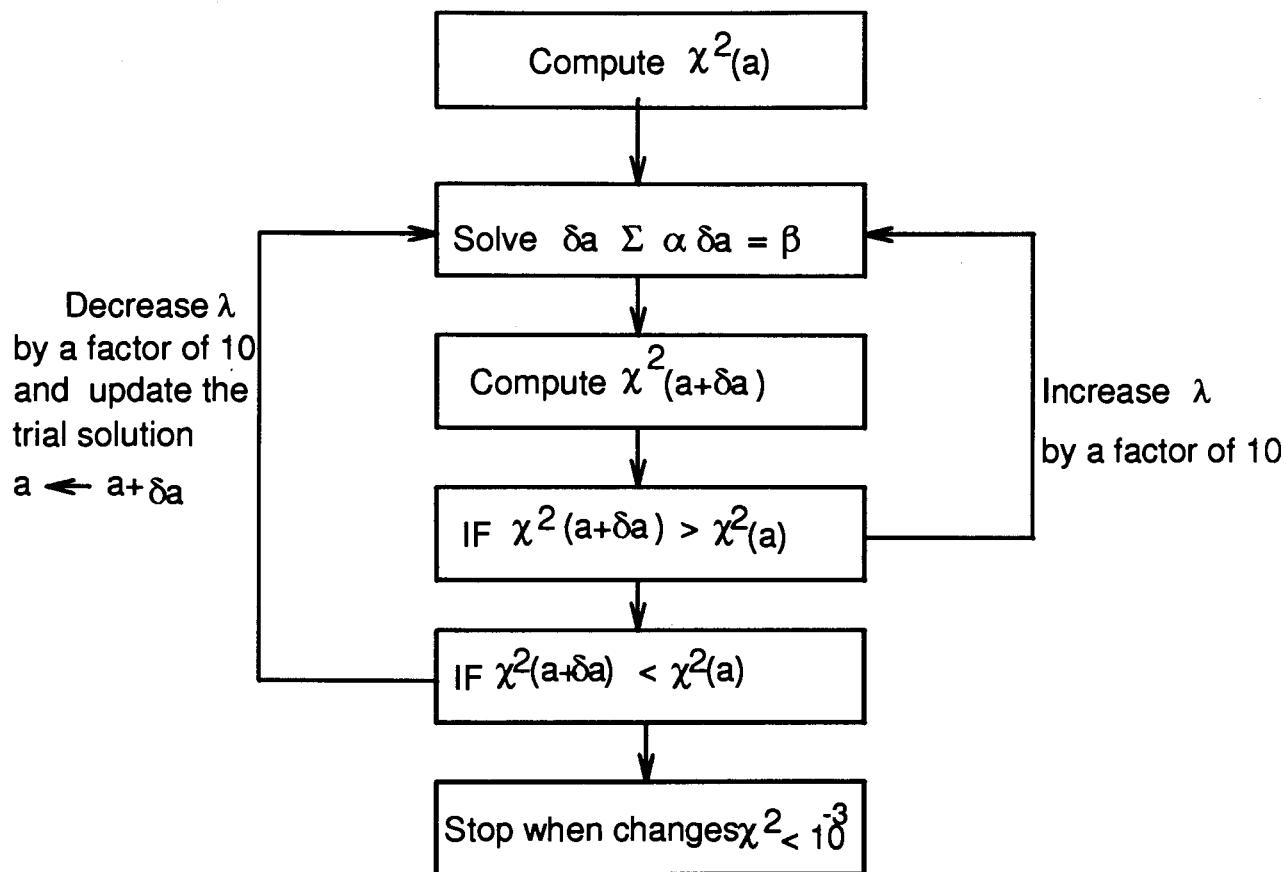


Figure 4.5: The flow diagram for L-M fitting method

#### 4.4.5 Correlations and Standard Errors

Obviously the measurement errors in the data must introduce some uncertainty in the determination of these parameters. If the data are independent, then each contributes

its own bit of uncertainty to the parameters. Consideration of the propagation of errors shows that the standard uncertainty of the estimated parameters  $\vec{a}_{min}$  can be written :[16]

$$\sigma^2(a_j) = \sum_{i=1}^N \sigma_i^2 (\partial a_j / \partial I_i)^2 \quad (4.26)$$

where  $I_i = I(s_i, \vec{a})$  and  $\sigma_i$  is the measurement errors at  $s_i$ . It has been proven for a linear model by using least square minimization that [16, 55]

$$\sigma^2(a_j) = [\alpha]_{jj}^{-1} \quad (4.27)$$

The matrix  $C_{jk} = [\alpha]_{jk}^{-1}$  is called the covariance matrix because its off-diagonal elements  $C_{jk}$  give the the correlation between  $a_j$  and  $a_k$  [16, 55]. However the formal covariance matrix  $C_{jk}$  that comes out of the least square  $\chi^2$  minimization has a clear quantitative interpretation only if

1. the measurement errors  $\sigma_i$  are normally distributed
2. the model is a linear function of its parameters
3. the sample size is large enough that the uncertainties in the fitted parameters  $\vec{a}$  do not extend outside a region in which the model could be replaced by a suitable linearized model [16]

If one of the conditions listed above is not satisfied, which is very common in real fitting problems such as our X-ray fitting (extremely nonlinear function), we are still "allowed" to : [16]

1. fit for parameters by minimizing  $\chi^2$
2. use the covariance matrix  $C_{jk}$  as the *formal covariance matrix* of the fit

It is difficult to obtain a quantitative estimate of the standard errors of  $\vec{a}$  for an extremely nonlinear system. The interested reader can refer to chapter 15 of [16]. We have implemented methods described there.

For a typical fit such as in figure 1.5 (two layer model), the covariance matrix and the formal standard errors will be given at the end of fitting by an output file like the following;

CHISQ= 61.04565824336		No of Iers= 8		
Description	Parameters	Errors	Steps	Labels
Scale factor	363.7146	0.231217	5.000000	1
Background	913.5301	1.200901	5.000000	1
Debye Factor	0.3852	0.001890	0.010000	1
In-plane strain	0.0000	0.000000	0.010000	0
Pt	0.1281	0.001151	0.010000	1
c	3.3822	0.000014	0.010000	1
a	2.4617	0.000032	0.010000	1
P	0.5303	0.001677	0.010000	1
La	196.9209	1.798934	3.000000	1
c-axis strain	0.0914	0.000183	0.010000	1
Prefered Orientation	0.1614	0.001800	0.010000	1
Absorption factor	4.0000	0.000000	0.001000	0
MO	37.4750	0.051050	3.000000	1

## CORRELATION MATRIX

1.00	0.17	0.55	NA	0.06	-0.01	0.14	-0.05	0.36	-0.01	-0.12	NA	-0.01
0.17	1.00	0.48	NA	0.21	0.03	-0.10	-0.27	0.02	-0.22	-0.06	NA	-0.07
0.55	0.48	1.00	NA	0.17	0.03	-0.10	-0.22	-0.01	-0.16	-0.62	NA	-0.07
NA	NA	NA	NA	NA	NA	NA	NA	NA	NA	NA	NA	NA
0.06	0.21	0.17	NA	1.00	0.02	-0.05	-0.84	-0.06	-0.04	0.01	NA	-0.01
-0.01	0.03	0.03	NA	0.02	1.00	-0.01	-0.02	0.00	-0.10	-0.02	NA	-0.04
0.14	-0.10	-0.10	NA	-0.05	-0.01	1.00	0.09	0.40	0.02	0.06	NA	0.01
-0.05	-0.27	-0.22	NA	-0.84	-0.02	0.09	1.00	0.15	0.04	-0.02	NA	0.02
0.36	0.02	-0.01	NA	-0.06	0.00	0.40	0.15	1.00	0.00	0.05	NA	0.00
-0.01	-0.22	-0.16	NA	-0.04	-0.10	0.02	0.04	0.00	1.00	0.11	NA	0.68

```

-0.12 -0.06 -0.62 NA  0.01 -0.02  0.06 -0.02  0.05  0.11  1.00 NA  0.06
NA    NA    NA    NA  NA    NA    NA    NA    NA    NA    NA    NA    NA
-0.01 -0.07 -0.07 NA -0.01 -0.04  0.01  0.02  0.00  0.68  0.06 NA  1.00
    
```

The first line gives  $\chi^2$  and the number of iterations for the calculation. The next thirteen rows list the parameters, standard errors and the step for computing the derivative relative to each parameter. Finally a correlation matrix is given. The NA (Not Applicable) in matrix indicates that the corresponding parameter was fixed during the adjustment. Negative elements in the matrix mean these two parameters prefer to change in opposite direction during the adjustment, otherwise in the same direction.

In order to see relative percentage of the correlation of two parameters, we have normalized off-diagonal elements with respect to diagonal elements, that is,  $\sqrt{C_{jj}C_{kk}}$  in the above matrix. Table 4.2 summarizes the parameters which appear in the output file.

Table 4.1: The meaning of parameters in the output file

Position	Parameters (in two-layer)	Parameters (in one-layer)
1	scale factor	scale factor
2	background constant	background constant
3	Debye temperature factor	Debye temperature factor
4	inplane strain factor $\zeta = 0$	inplane strain factor $\zeta$
5	$P_t$	$g$
6	$c$	$c$
7	$a$	$a$
8	$P$	$P$
9	$L_a$	$L_a$
10	$\sqrt{\langle \delta^2 \rangle}$	$\sqrt{\langle \delta^2 \rangle}$
11	preferred orientation factor	preferred orientation factor
12	absorption factor	absorption factor
13	$M_0$	$M_0$

Some of the formal standard errors seem too small compared to what we expect by common sense. In this case one has to multiply these numbers by a more or less arbitrary factor according to the confidence level chosen for this parameter (see [16]). Usually the errors won't become larger than 10% in our calculation.

Finally I want to make a few short comments about our refinement program. The program is written in FORTRAN 77 and is presently operated on a SUN SPARC IPC desk-top workstation (about \$6000 US). A typical structure solution uses about twenty minutes of CPU time. Similar running times are expected for the program if it is operated on a 486 IBM PC machine. At the end of refinement, a graphical comparison between the data and the calculation is available as well as the values of the structural parameters and their formal standard deviations etc.. We have used the program to fit over 50 kinds of disordered carbons from Canadian, US and Japanese sources, including cokes, heat treated cokes, carbon fibers, synthetic graphites and mesocarbon microbeads, and have been able to fit every one acceptably (see next chapter for examples). We believe that this program is useful for carbon manufacturers and researchers to get structural information.

*“Give me four parameters, I can fit an elephant.”*

— Anonymous

## Chapter 5

### Examples of Fits

X-ray diffraction data were collected using a Phillips diffractometer with fixed slits and a diffracted beam monochromator whose wavelength discrimination is insufficient to remove  $K_{\alpha 2}$  radiation. We used  $Cu K_{\alpha}$  radiation for all of the results described in this thesis. The goniometer radius is 173mm, the incident beam divergence was 1/2 degree and the receiving slit width was 0.2mm for most of the measurements shown here. A set of Soller slits is used in the incident beam for collimation in the scattering plane. The instrumental resolution of this equipment is about 0.15 degrees full width half maximum. Even though our equipment can resolve  $K_{\alpha 1}$  and  $K_{\alpha 2}$  peaks above about  $2\theta = 50$  degrees on well crystallized samples, we *have not* included the two wavelengths in our refinement program because all the samples we studied have much broader peaks; the program uses the weighted average  $Cu K_{\alpha}$  wavelength,  $\lambda = 1.54178\text{\AA}$  [26].

The sample holder we use and its effects on peak shapes has been described in section 3.4 in chapter 3 where we discuss the penetration of the X-rays into the sample. The sample holder has a depth of 2.5 millimeters so that sufficient carbon can be loaded to give a good signal in a reasonable time even for disordered carbons. The disadvantage of this method is that the finite depth of the sample and the penetration of the X-rays within it leads to broadening of the peaks which are, however, treated by



Table 5.1: Selected Carbons Fitted and Plotted For Examples

Carbons	Description of Carbons	HTT°C	Data and Fit Shown in Figures
S 550	Petroleum Pitch Heated to 550	550C	Figure 5.1
S 900	Petroleum Pitch Heated to 900	900C	Figure 1.2
S 1100	Petroleum Pitch Heated to 1100C	1100C	Figure 5.2
S 2000	Petroleum Pitch Heated to 2000C	2000C	Figure 5.3
S 2850	Petroleum Pitch Heated to 2850C	2850C	Figure 1.4 (1-layer model)
S 2850	Petroleum Pitch Heated to 2850C	2850C	Figure 1.5 (2-layer model)
Conoco 2100	Petroleum Needle Coke Heated to 2100	2100C	Figure 5.4
Conoco 2200	Petroleum Needle Coke Heated to 2200	2200C	Figure 5.5
Conoco 2300	Petroleum Needle Coke Heated to 2300	2300C	Figure 5.6
Osaka 1	Osaka Gas Commercial Carbon	Unknown	Figure 5.9
Osaka 2	Osaka Gas Commercial Carbon	Unknown	Figure 5.10
Osaka 9	Osaka Gas Commercial Carbon	Unknown	Figure 5.11
Osaka 16	Osaka Gas Commercial Carbon	Unknown	Figure 5.12
KH 1200	A Special Hard Carbon	1200	Figure 5.13
KH 2000	A Special Hard Carbon	2000	Figure 5.14
KH 2850	A Special Hard Carbon	2850	Figure 5.15
FA 600	Synthesized from Polyfurfuryl Alcohol at Moli	600C	Figure 5.16
FA 900	Synthesized from Polyfurfuryl Alcohol at Moli	900C	Figure 5.17
FA 1100	Synthesized from Polyfurfuryl Alcohol at Moli	1100C	Figure 5.18
G2300	A Synthetic Graphitic Carbon at 2300C	2300C	Figure 5.19
G2500	A Synthetic Graphitic Carbon at 2500C	2500C	Figure 5.20
G2800	A Synthetic Graphitic Carbon at 2800C	2800C	Figure 5.21

the program. Alternative measuring schemes could include a thin layer of powder on a glass slide or on a zero background sample holder. In the former case, the scattering from the quartz or glass overlaps with the (002) peak from disordered carbons and is unacceptable. For zero background holders, the count rates from thin layers of disordered carbons is much lower than from our thick samples. Since it is not too difficult to calculate the effect of the thick samples on the peak shapes, we decided to use thick samples for our work. However our refinement program can operate on thin samples in zero background holders by adjusting geometrical factors which account for the sample holder shape. For the results shown in the next sections, the absorption length was calculated from the measured density of our packed samples using the methods described in Cullity (1956) [26] and was not refined.

For crystalline samples where  $M$  is large and  $\sqrt{\langle \delta^2 \rangle}$  is small, the 002 peak width measured for the sample on a zero background holder can approach the instrumental resolution. Theoretically, to correctly determine  $M$  and  $\sqrt{\langle \delta^2 \rangle}$  for crystalline carbons, we need to include the effects of the instrument resolution in the program. However, most of the carbons we have studied do not have such large  $M$  and small  $\sqrt{\langle \delta^2 \rangle}$ . The instrumental resolution of the equipment (0.15 degree) was therefore neglected for all carbons in our studies.

To illustrate the effectiveness of our method, we have selected some carbons for discussion here. These carbons are from different sources and vary in their heat treatment temperature. Table 5.1 lists a summary of some of the carbons which we have studied and which will be discussed here.

## 5.1 Petroleum Pitch Series

We obtained petroleum pitch samples heated to different temperatures from Moli Energy (1990) Ltd.. These are soft carbons and we distinguish these carbons by their heat treatment temperature (HTT) as S1100, S2000 etc., where 1100°C and 2000°C stand for the HTT. In the next sections we use a similar naming system to indicate different HTT carbons of the same group (see the table 5.1).

Figure 5.1 shows the measured, calculated and difference profiles (using the one

layer model) for S550. This is a very disordered carbon containing substantial hydrogen with very small crystallite size. The values of the refined parameters are given in table 5.2. (We use a constant background for all fits.) For this carbon  $P$  and  $M$  were fixed at  $P = 1$  and  $M = 40$ . The parameter  $g$  includes substantial regions of unorganized carbon ( $1 - g$  is about 53% for this carbon), which gives a good fit to the profile in the (002) region. The spacing fluctuations for the unorganized regions of this carbon are large,  $\sqrt{\langle \delta^2 \rangle} = 2.0 \text{ \AA}$ , which is actually so big that the  $d_{002}$  spacing is not so meaningful any more.

Figure 1.4 in chapter 1 shows the data and theory (one layer model) for S900 carbon. The unorganized regions still dominate the carbon grains. The layer size,  $L_a$ , increased to  $17 \text{ \AA}$ . The interlayer spacing fluctuation,  $\sqrt{\langle \delta^2 \rangle}$ , is still quite large ( $1.02 \text{ \AA}$ ), but it has substantially decreased compared to S550.

Figure 5.2 shows the data, theory and difference (one layer model) for S1100. There is still random disorder between every pair of layers, but the layer extent,  $L_a$ , has increased a lot ( $L_a = 31.02 \text{ \AA}$ ) so that the shape of the two dimensional peak (100) can now be discerned.

Figure 5.3 shows the effect of higher heating temperature. S2000 shows much sharper (002), (004) and (006) peaks due to an increase in  $L_c$  and a decrease in  $\sqrt{\langle \delta^2 \rangle}$ . (We have set  $g = 0$  to exclude unorganized regions and use a Gaussian distribution for interlayer spacing fluctuations.)

The left hand edge of the (100) peak has sharpened substantially compared to S1100 as a result of an increase in  $L_a$  to about  $111 \text{ \AA}$  as shown in table 5.2. The (100) and (110) peaks still have predominantly 2D shapes and no mixed index peaks are observable. The program is capable of measuring  $L_a$  for 2D peaks where naive application of the Scherrer equation would give spurious results.  $P$  is refined to 0.76 which indicates that there is slightly more intensity to the right side of the (100) peak than that predicted for  $P = 1$ .

The interlayer spacing,  $d_{002}$ , has continued to decrease and the a spacing has further increased compared to S1100. The refinement results clearly give substantial insight into the graphitization process for this particular type of carbon. Apparently, increases in  $L_a$  and  $L_c$  and decreases in  $\sqrt{\langle \delta^2 \rangle}$  occur before the turbostratic disorder

Figure 5.1: The Diffraction Pattern of Petroleum Pitch 550°C

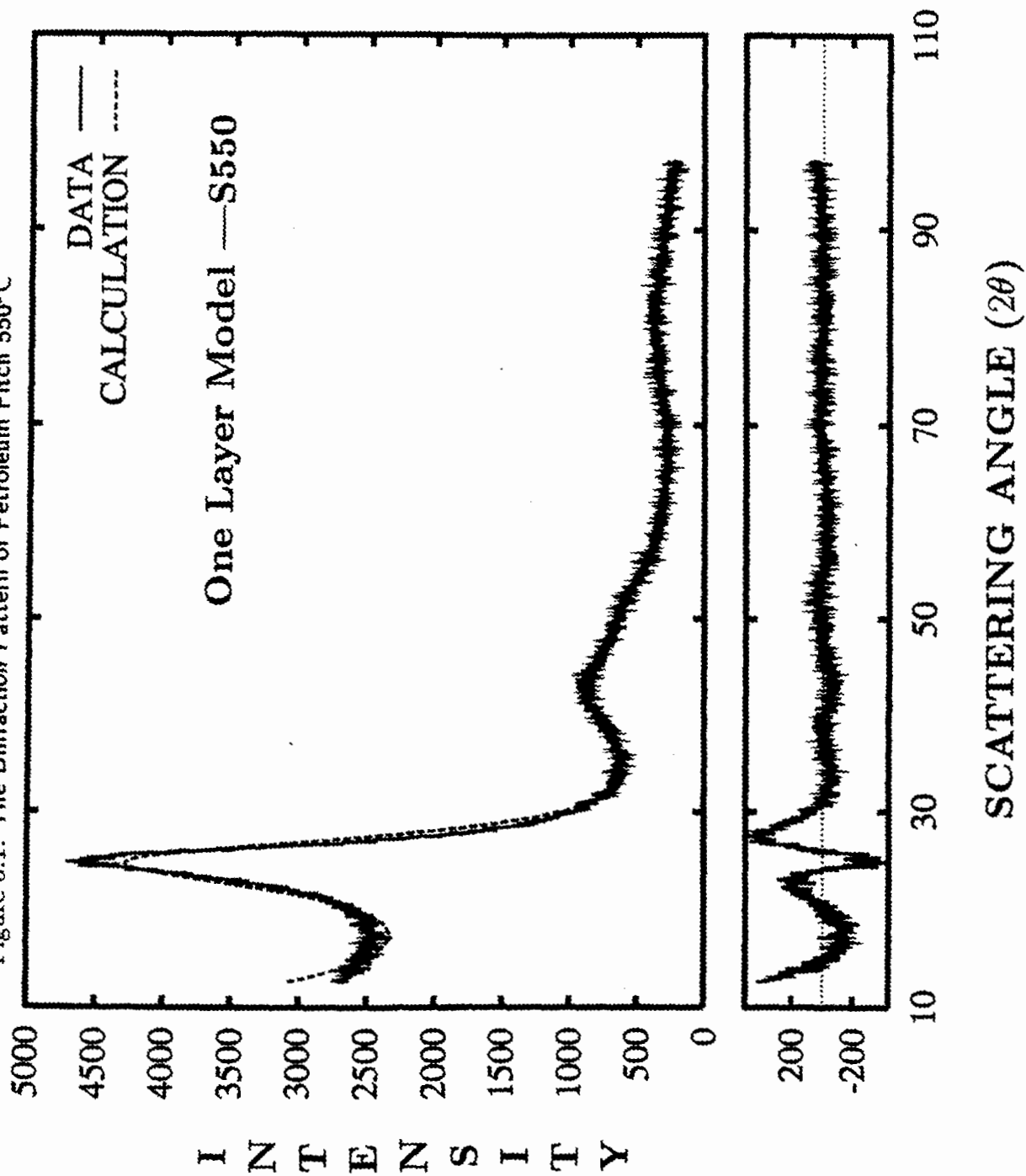


Figure 5.2: The Diffraction Pattern of Petroleum Pitch 1100°C

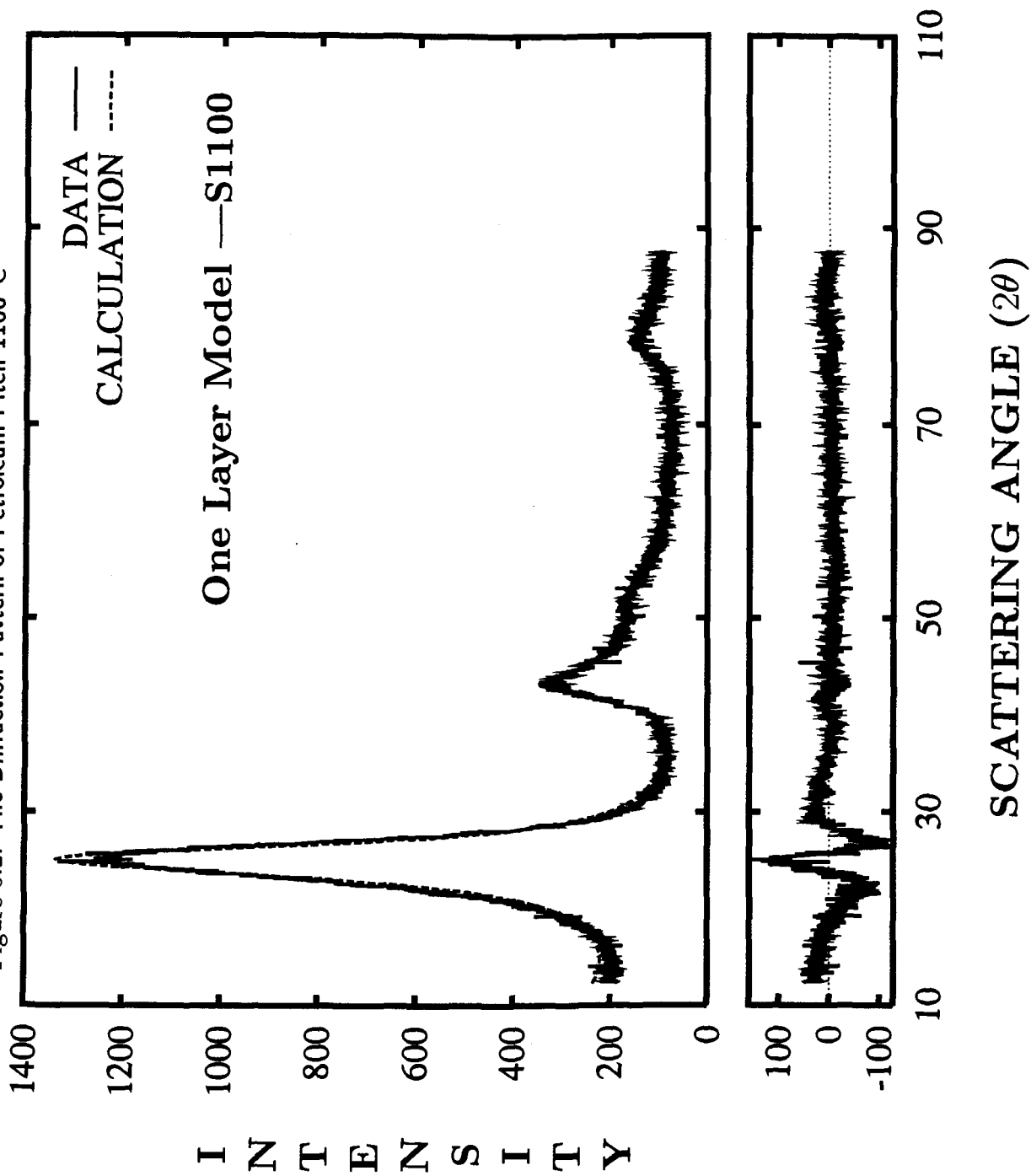
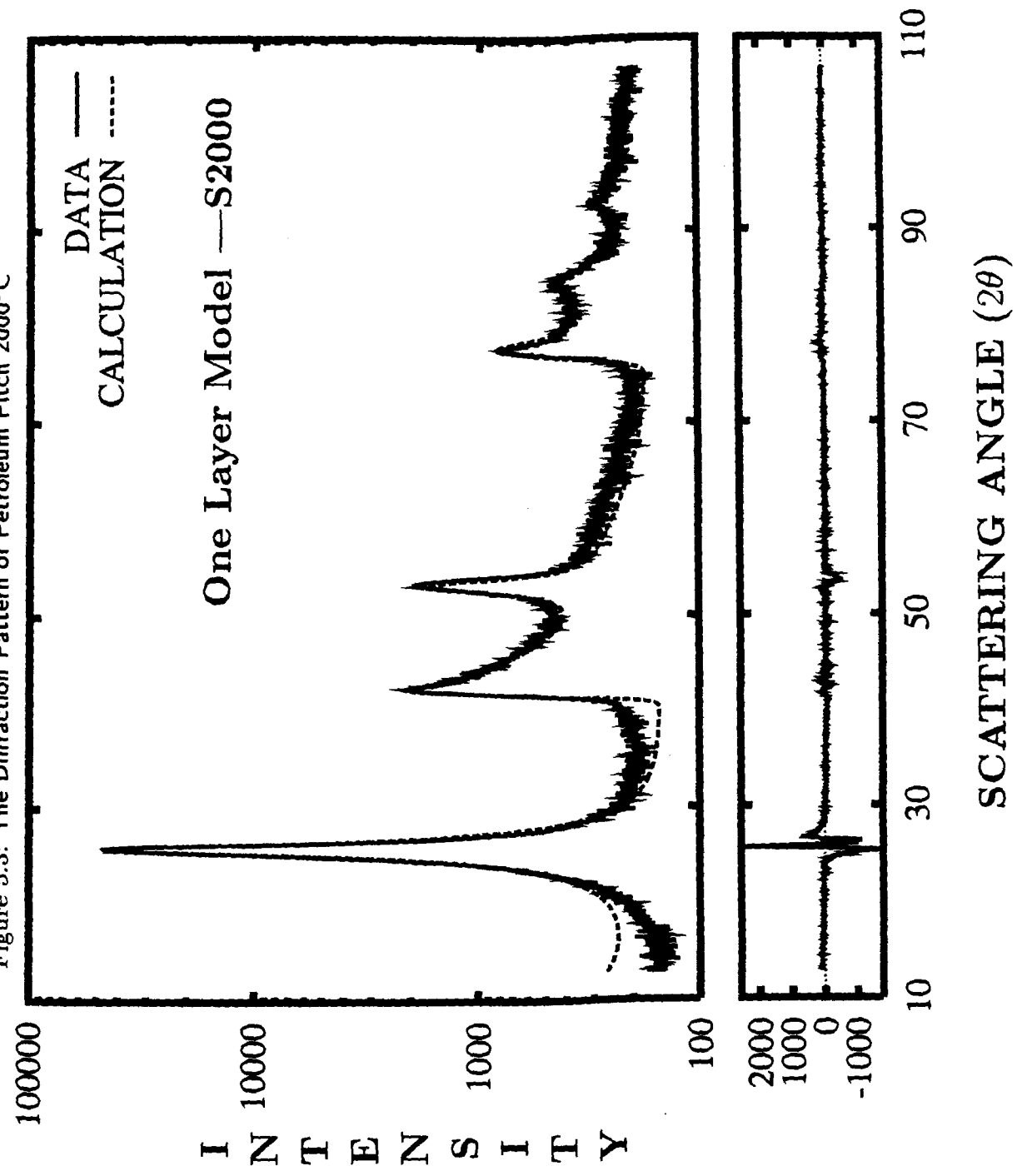


Figure 5.3: The Diffraction Pattern of Petroleum Pitch 2000°C



can be substantially relieved.

Figure 1.4 in chapter 1 shows measured and calculated (one layer model) patterns for S2850. Now, the mixed index peaks are clearly observed and the refinement indicates that only about 28% of adjacent layer pairs show the random shifts characteristic of turbostratic disorder. The fit, however, is poor in the (100)/(101) area because of the use of one layer model for this highly graphitic carbon. Figure 1.5 in chapter 1 shows the fits to the same data when the two layer model is used. The agreement is extremely good near (100), (101), (103) and also at higher angle regions since  $P_t$  is simultaneously refined. The two layer model works much better for this carbon.

In the last section of chapter 4, we examined the output file and discussed the correlation among parameters and the way to estimate the standard error of each parameter. Another output file S2000 is included here for further discussion.

CHISQ= 11.33943118762		Number of Iers = 5		
Description	Parameters	Errors	Steps	Labels
Scale factor	4427.7543	6.189617	0.010000	1
Background	141.9923	0.533237	0.010000	1
Debye factor	0.2804	0.004502	0.001000	1
In-plane strain	0.0035	0.000525	0.000100	1
Organized carbon	0.0000	0.000000	0.010000	0
Layer spacing	3.4300	0.000051	0.001000	1
Interatomic distance	2.4591	0.000153	0.001000	1
Probability P	0.8971	0.003407	0.001000	1
Layer size	105.1832	5.166665	0.010000	1
d-spacing fluctuation	0.1085	0.000362	0.001000	1
Preferred Orientation	0.2691	0.004444	0.001000	1
Absorption factor	4.0000	0.000000	0.001000	0
Number of layers	51.3886	0.197689	0.001000	1

CORRELATION MATRIX

1.00	0.11	0.51	-0.03	NA	-0.03	0.15	-0.04	-0.01	0.02	-0.11	NA	0.02
0.11	1.00	0.52	-0.08	NA	0.00	0.00	-0.01	-0.04	-0.22	-0.10	NA	-0.04
0.51	0.52	1.00	-0.07	NA	-0.01	-0.07	-0.04	-0.06	-0.17	-0.65	NA	-0.05
-0.03	-0.08	-0.07	1.00	NA	0.00	-0.01	-0.09	0.96	0.02	0.01	NA	0.01
NA	NA	NA	NA	NA	NA	NA	NA	NA	NA	NA	NA	NA
-0.03	0.00	-0.01	0.00	NA	1.00	0.00	0.00	0.00	0.01	0.00	NA	-0.02
0.15	0.00	-0.07	-0.01	NA	0.00	1.00	-0.05	0.10	0.01	0.17	NA	0.01
-0.04	-0.01	-0.04	-0.09	NA	0.00	-0.05	1.00	-0.09	-0.03	0.01	NA	-0.03
-0.01	-0.04	-0.06	0.96	NA	0.00	0.10	-0.09	1.00	0.02	0.04	NA	0.01
0.02	-0.22	-0.17	0.02	NA	0.01	0.01	-0.03	0.02	1.00	0.12	NA	0.75
-0.11	-0.10	-0.65	0.01	NA	0.00	0.17	0.01	0.04	0.12	1.00	NA	0.06
NA	NA	NA	NA	NA	NA	NA	NA	NA	NA	NA	NA	NA
0.02	-0.04	-0.05	0.01	NA	-0.02	0.01	-0.03	0.01	0.75	0.06	NA	1.00

The correlation between parameters is not strong for most pairs of parameters. For example, the layer number  $M_0$  (No. 13) and c-axis strain  $\sqrt{\langle \delta^2 \rangle}$  (No. 10) have 71% correlation in this example, which is reasonably acceptable for a strong nonlinear problem. Physically these two parameters should show some correlation since they have a similar effect on  $(00l)$  peaks. To eliminate the uncertainty involved in these strongly correlated parameters, one must include as many peaks as possible from the same family of planes. Since the effect of  $M$  and  $\delta$  on the various  $00l$  peaks is different, the uncertainty in  $M$  and  $\delta$  will be greatly reduced if one can determine values for  $M$  and  $\delta$  which fit all the  $00l$  peaks observed. If the two parameters are correlated very strongly, one may have to change the model, which is difficult.

The other possible strongly correlated pairs should be  $(g, \delta)$ ,  $(L_a, \zeta)$  and  $(P, P_t)$ . In the following parameter tables, we also list these correlations but ignore the rest of the correlation pairs since they are usually small and unimportant physically. The formal errors in  $a$ ,  $d_{002}$  and  $P$  etc. are too small to be believable. The errors indicated in table 5.2 are our estimates of the true errors, where we have taken into account the fact that the theory does not exactly describe the data even if the data were completely free of noise.  $\chi^2$  is also listed in these tables for reference.



Table 5.2: The Structural Parameters and Selected Correlation Percentages for the Five Petroleum Pitch Carbons

Quantity	S550	S900	S1100	S2000	S2850 (1layer)	S2850 (2layer)
$\chi^2$	4.3	37.2	2.1	2.28	73.5	61.0
$d_{002}$ (Å)	3.488(1)	3.479(1)	3.475(2)	3.411(1)	3.382(1)	3.382(1)
$a$ (Å)	2.460(1)	2.450(1)	2.440(1)	2.460(1)	2.463(1)	2.461(1)
$P$	1.0*	1.0*	1.0*	0.76(1)	0.28(1)	0.26(1) <sup>+</sup>
$P_t$	NA	NA	NA	NA	NA	0.128(1)
$g$	0.475(1)	0.405(3)	0.482(7)	0*	0*	0*
$\zeta$	0.03(1)	0.014(1)	0.036(4)	0*	0*	0*
$\sqrt{\langle \delta \rangle^2}$ (Å)	2.00(1)	1.02(1)	0.86(1)	0.080(1)	0.065(1)	0.091(1)
$M$	40*	40*	40*	74(1)	73(1)	74(1) <sup>++</sup>
$L_a$ (Å)	7.3(3)	17(1)	44(6)	111(4)	198(8)	196(2)
$\text{Corr}(M, \delta)$	NA	NA	NA	71%	63%	68%
$\text{Corr}(g, \delta)$	97%	96%	97%	NA	NA	NA
$\text{Corr}(P, P_t)$	NA	NA	NA	NA	NA	84%

\* Fixed during the refinement.

+ Divided by 2 for the comparison with one layer data.

++ Multiplied by 2 for the comparison with one layer data.

## 5.2 Conoco Soft Carbon Series

The Conoco Soft Carbons were made by heating petroleum needle coke (designated XP from Conoco Inc.) under inert gas. The three Conoco samples used here were heated to 2100, 2200 and 2300°C respectively at Conoco's research lab in Ponca City, Oklahoma. We call these carbons Conoco 2100, Conoco 2200 and Conoco 2300.

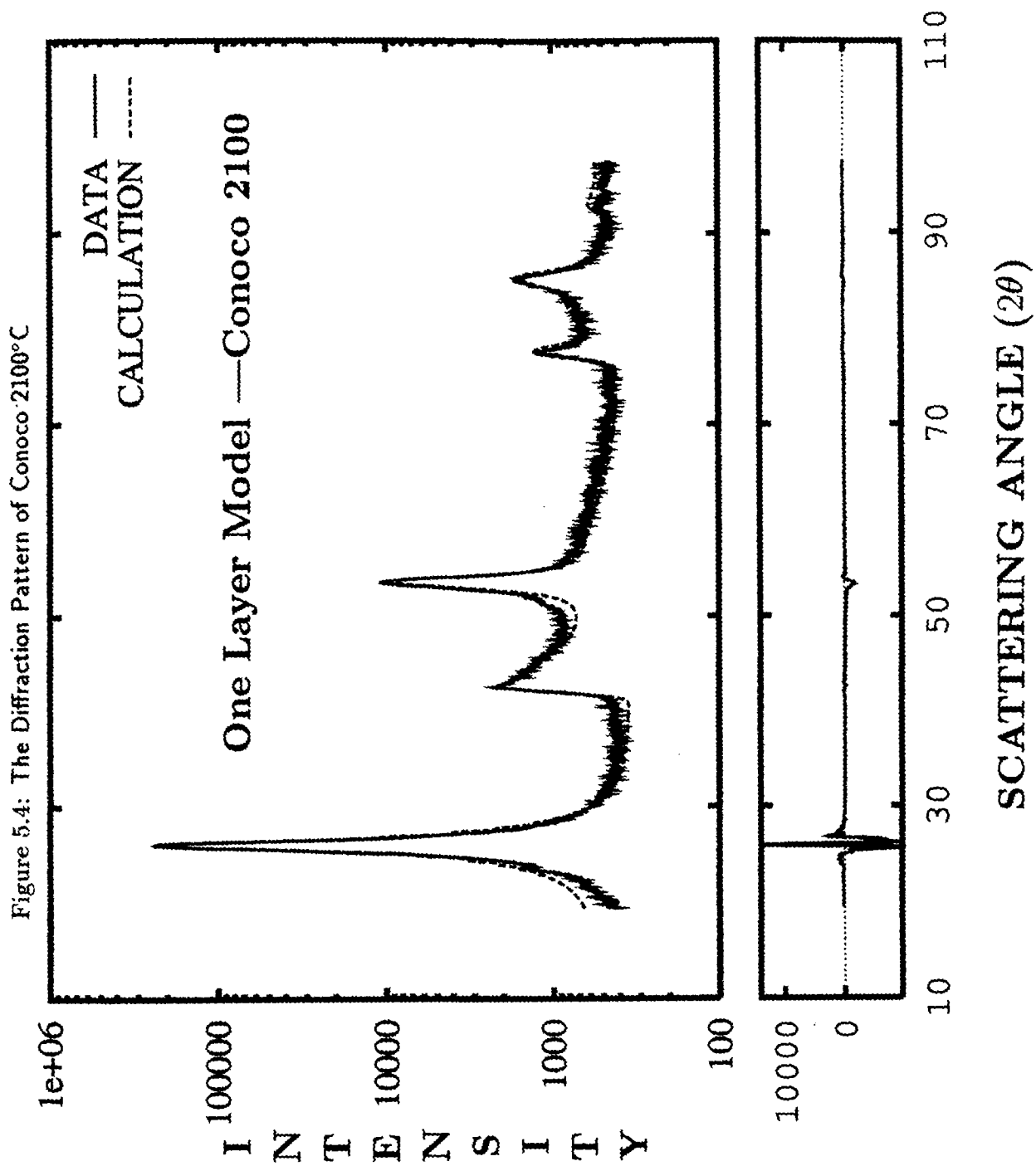
Figures 5.4 to 5.6 show the data, theory and difference (one layer model) for Conoco 2100, Conoco 2200 and Conoco 2300 respectively. The refined parameters for these three carbons are listed in table 5.3. All fits done here have set  $g = 0$ , that is, assuming all the carbon is organized.

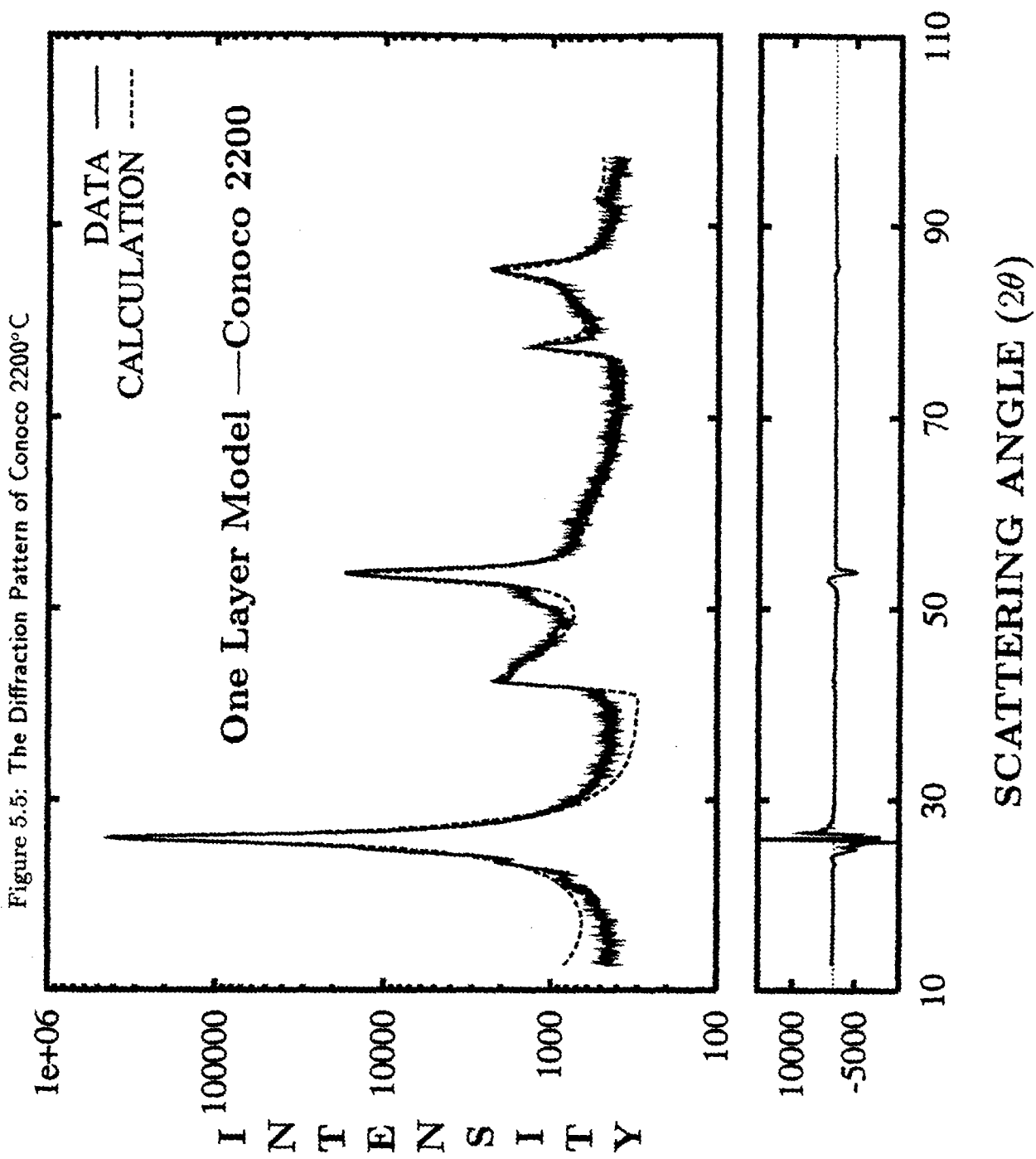
As the heating temperature increases from 2100 to 2300°C, the random disorder between adjacent layers decreases. The (101) shoulder on the right side of (100) begins to appear, which is a signature of the onset of registered stacking. At 2100°C, there is only a hint of a (101) shoulder since the random disorder is still present for about 77% of adjacent layers.

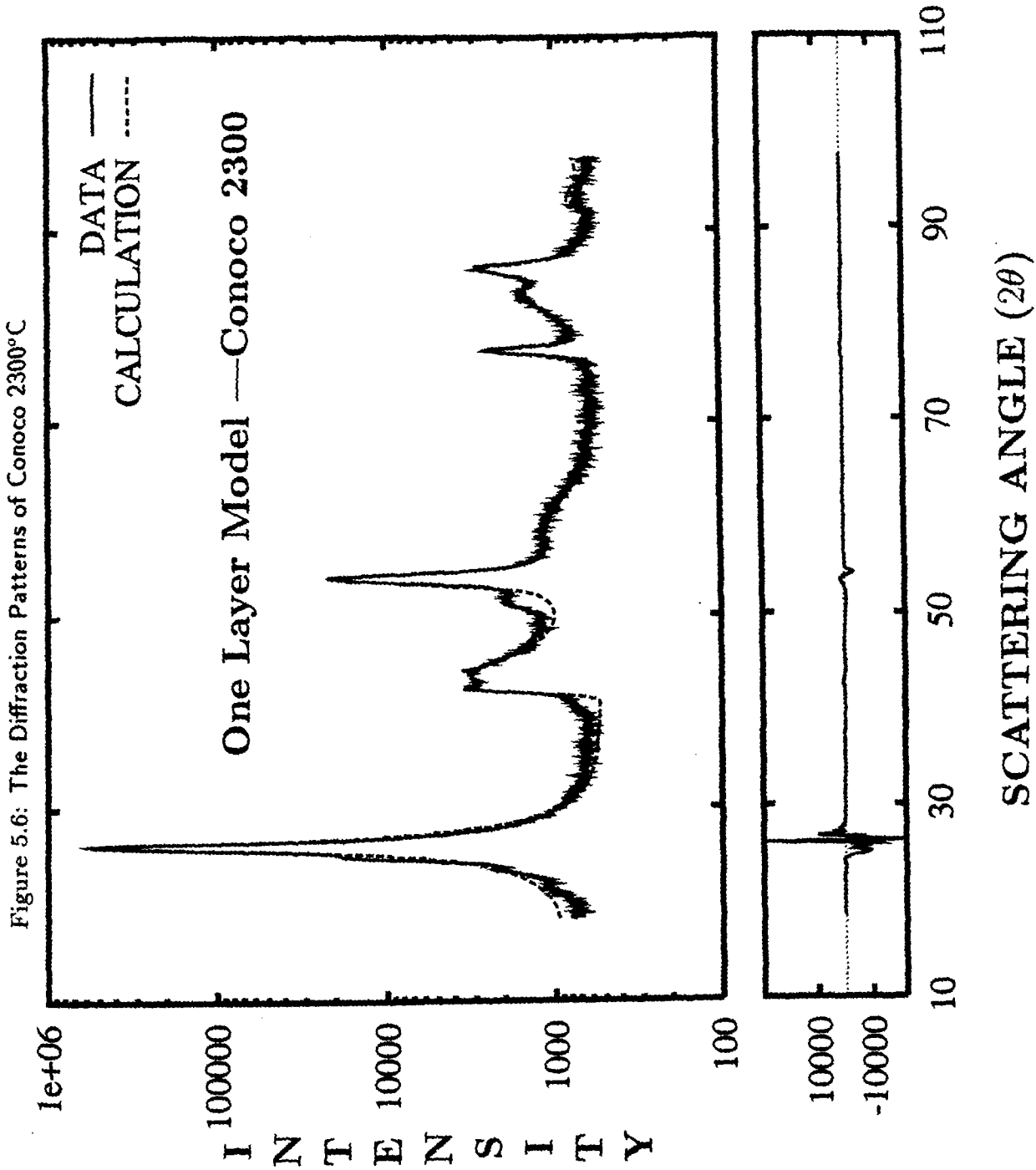
At 2200°C, a tiny shoulder on the right of (100) begins to appear. Upon further heating to 2300°C, the random disorder significantly decreases ( $P = 0.48$ ), and the (101) shoulder is clearly a peak. It is a nice that such a simple model can describe this fine structure.

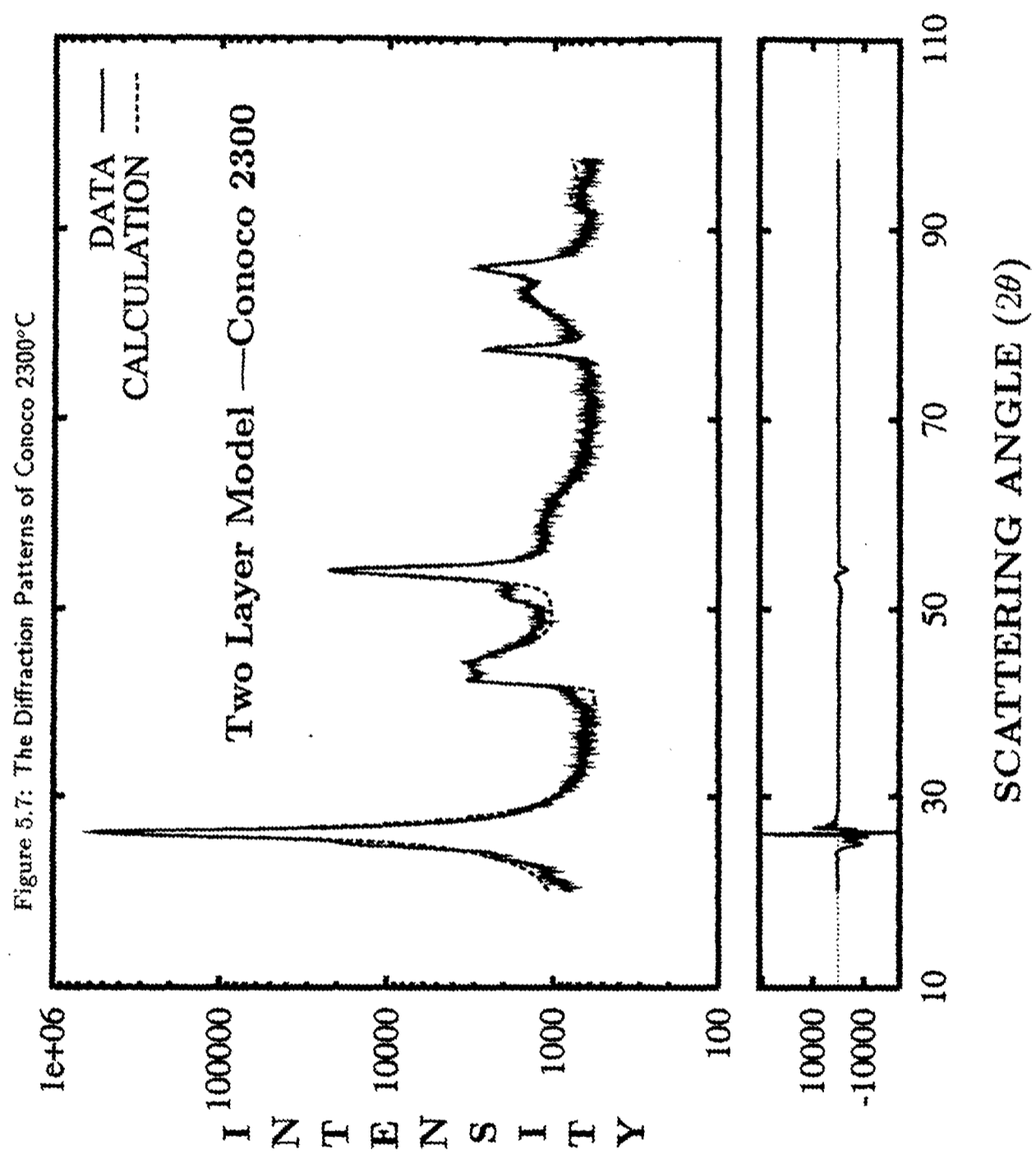
As expected, the one layer model is not the best for some of the graphitic carbons. These carbons are all in the range of crossover between regions where the one layer model is best (less than 2200°C) and regions where the two layer model is best (greater than 2200°C) (see chapter 2). For the Conoco 2100 data, the one layer fitting is better than that of the two layer model, but for Conoco 2300, the two layer model works better. Figure 5.7 shows the data, calculation and difference profiles for Conoco 2300 fitted with the two layer model. The fit is better than that of the one layer model (figure 5.6) in the range of (100)/(101) and (110)/(112). To illustrate, figure 5.8 shows the (100)/(101) range for clarity and comparison. The two layer model fits the 3D mixing fine structure of graphitic carbons (usually above the 2200°C) much better than the one layer model does.

The carbon sheets in the Conoco carbons are so close to perfect graphite layers









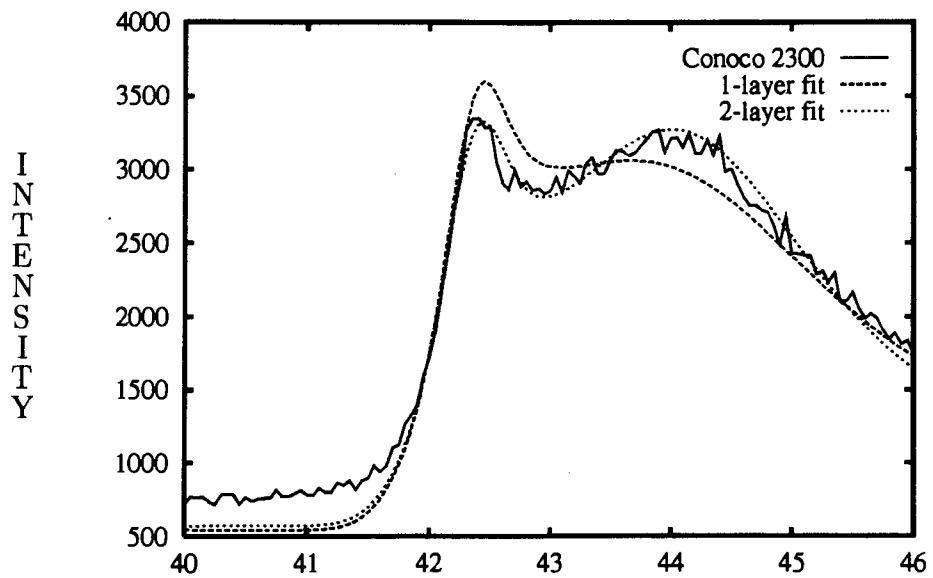


Figure 5.8: Blow-up For Comparison between one and two layer fitting

that in-plane strains are negligible. We simply set  $\zeta = 0$  during the fitting. The correlation between  $M$  and  $\delta$  is acceptable for these carbons as well.

### 5.3 Osaka Carbon Series

The Osaka carbons from Osaka Gas Ltd. are commercial carbons and are given designation numbers by the manufacturer. The detailed manufacturing information, such as HTT, is unknown to us. However, from the X-ray fitting studies, we can tell these are basically low temperature heated soft carbons. Turbostratic disorder between layers is present in all these carbons. For illustration, we have selected four carbons from about 15 Osaka carbons available as examples. Figure 5.9 shows the data, theory and difference profiles (one-layer model) for a typical Osaka carbon, Osaka 1.

The fits are remarkably good. The adjacent layers are randomly stacked ( $P = 1$ ), and the fraction of unorganized carbon,  $1 - g$ , is high (about 0.77). The  $c$ -axis strain (layer spacing fluctuation) is only about  $1\text{\AA}$ , which is close to that of S900.

From our experience, we can tell that Osaka 1 is a low temperature heated carbon with HTT around  $700^\circ\text{C}$  or so (similar  $\sqrt{\langle \delta^2 \rangle}$  to S900, but larger  $1 - g$ ). Figures 5.10 to 5.12 show three more examples. The structural parameters and selected correlations between them all are summarized in table 5.4 for all the Osaka carbons. The correlations between  $g$  and  $\delta$  are quite large, which is typical for those carbons.

### 5.4 A Hard Carbon Series

The first hard carbon series is from a Japanese Company, which we can not reveal for proprietary reasons. The polymer precursor to these samples was not revealed by the manufacturer. But they did release the HTT of these hard carbons. We have samples at three different HTT, that is, 1200, 2000 and  $2850^\circ\text{C}$ . We call them hard carbon 1200, hard carbon 2000 and hard carbon 2850 respectively.

Figures 5.13 to 5.15 show the data, calculation and difference profiles for the three hard carbons. The corresponding refined parameters are listed in table 5.5. All three



Table 5.3: The Structural Parameters and Selected Correlation Percentages for the Three Conoco Carbons

Quantity	Conoco 2100	Conoco 2200	Conoco 2300 (1-layer)	Conoco 2300 (2-layer)
$\chi^2$	36.5	77.1	81.5	81.6
$d_{002}$ (A)	3.402(1)	3.408(1)	3.385(1)	3.385(1)
$a$ (A)	2.456(1)	2.462(1)	2.462(1)	2.462(1)
$P$	0.774(3)	0.736(2)	0.481(2)	0.417(2) <sup>+</sup>
$P_t$	NA	NA	NA	0.019(2)
$g$	0*	0*	0*	0*
$\zeta$	0*	0*	0*	0*
$\sqrt{\langle \delta \rangle^2}$ (A)	0.070(1)	0.071(1)	0.059(1)	0.083(1)
$M$	55.9(1)	69.7(1)	76.5(1)	76.0(1) <sup>++</sup>
$L_a$ (A)	91(1)	88(1)	178(3)	138(2)
Corr( $M, \delta$ )	61%	64%	61%	66%
Corr( $P, P_t$ )	NA	NA	NA	89%

\* Fixed during the refinement.

+ Divided by 2 for the comparison with one layer data.

++ Multiplied by 2 for the comparison with one layer data.

Table 5.4: The Structural Parameters and Selected Correlation Percentages for the Four Osaka Carbons

Quantity	Osaka 1	Osaka 2	Osaka 9	Osaka16
$\chi^{2+}$	1.3	1.2	2.7	1.5
$d_{002}(\text{Å})$	3.474(2)	3.519(2)	3.443(1)	3.477(2)
$a(\text{Å})$	2.427(1)	2.439(1)	2.429(1)	2.436(1)
$P$	1*	1*	1*	1*
$g$	0.23(1)	0.38(1)	0.51(1)	0.24(1)
$\zeta$	0.002(2)	0.019(4)	0.006(3)	0.000(1)
$\sqrt{\langle \delta >^2}(\text{Å})$	1.02(1)	1.26(1)	0.87(1)	1.17(1)
$M$	40*	40*	40*	40*
$L_a(\text{Å})$	14(1)	26(2)	18(1)	14(1)
$\text{Corr}(\zeta, \delta)$	4%	2%	0%	13%
$\text{Corr}(g, \delta)$	95%	90%	96%	93%

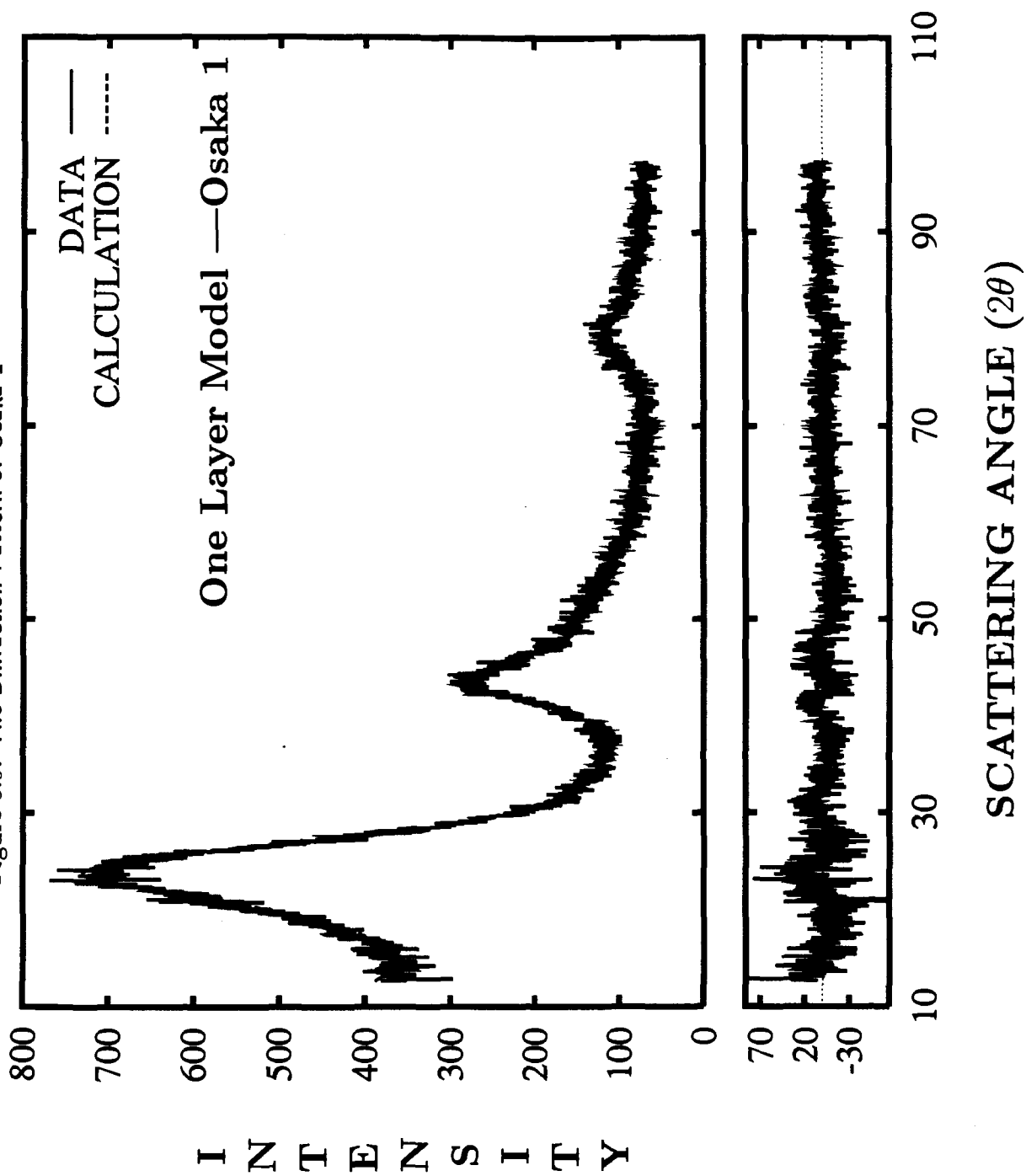
\* Fixed during the refinement. + these  $\chi^2$  are small because a low counting time was used to collect the data. The signal to noise rate is relatively small here.

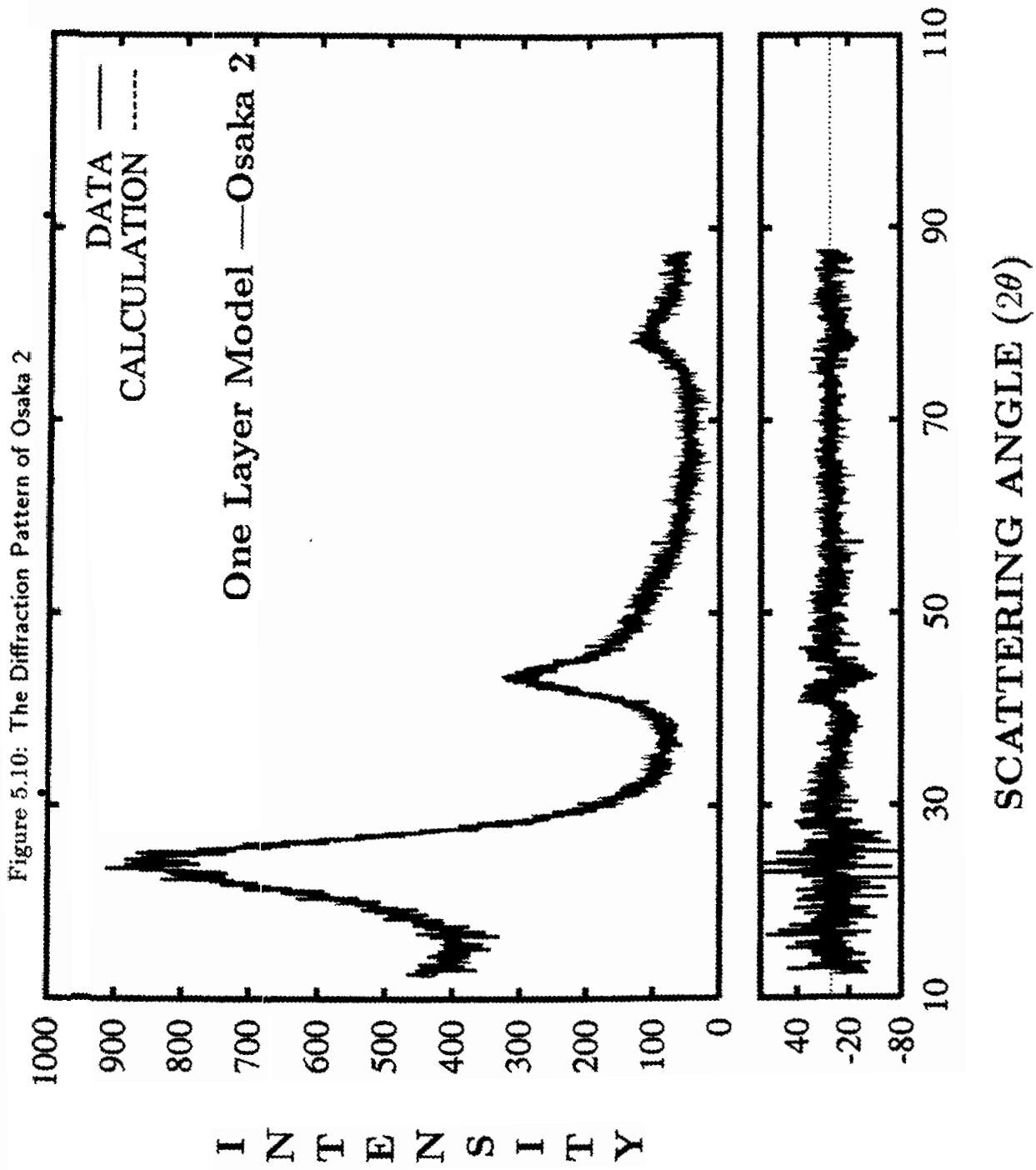
Table 5.5: The Structural Parameters and Selected Correlation Percentages for the Three Hard Carbons

Quantity	Hard 1200	Hard 2000	Hard 2850
$\chi^2$	2.0	4.3	28.4
$d_{002}(\text{Å})$	3.537(1)	3.463(1)	3.460(1)
$a(\text{Å})$	2.444(1)	2.449(1)	2.461(1)
$P$	1*	1*	1*
$g$	0.26(1)	0.55(1)	0.822(1)
$\zeta$	0.0132(2)	0.010(1)	0*
$\sqrt{\langle \delta >^2}(\text{Å})$	1.00(1)	0.91(1)	1.8(1)
$M$	40*	40*	40*
$L_a(\text{Å})$	24(1)	51(1)	45(1)
$\text{Corr}(g, \delta)$	88%	90%	74%
$\text{Corr}(L_a, \zeta)$	96%	96%	NA*

\* Fixed during the refinement.

Figure 5.9: The Diffraction Pattern of Osaka 1





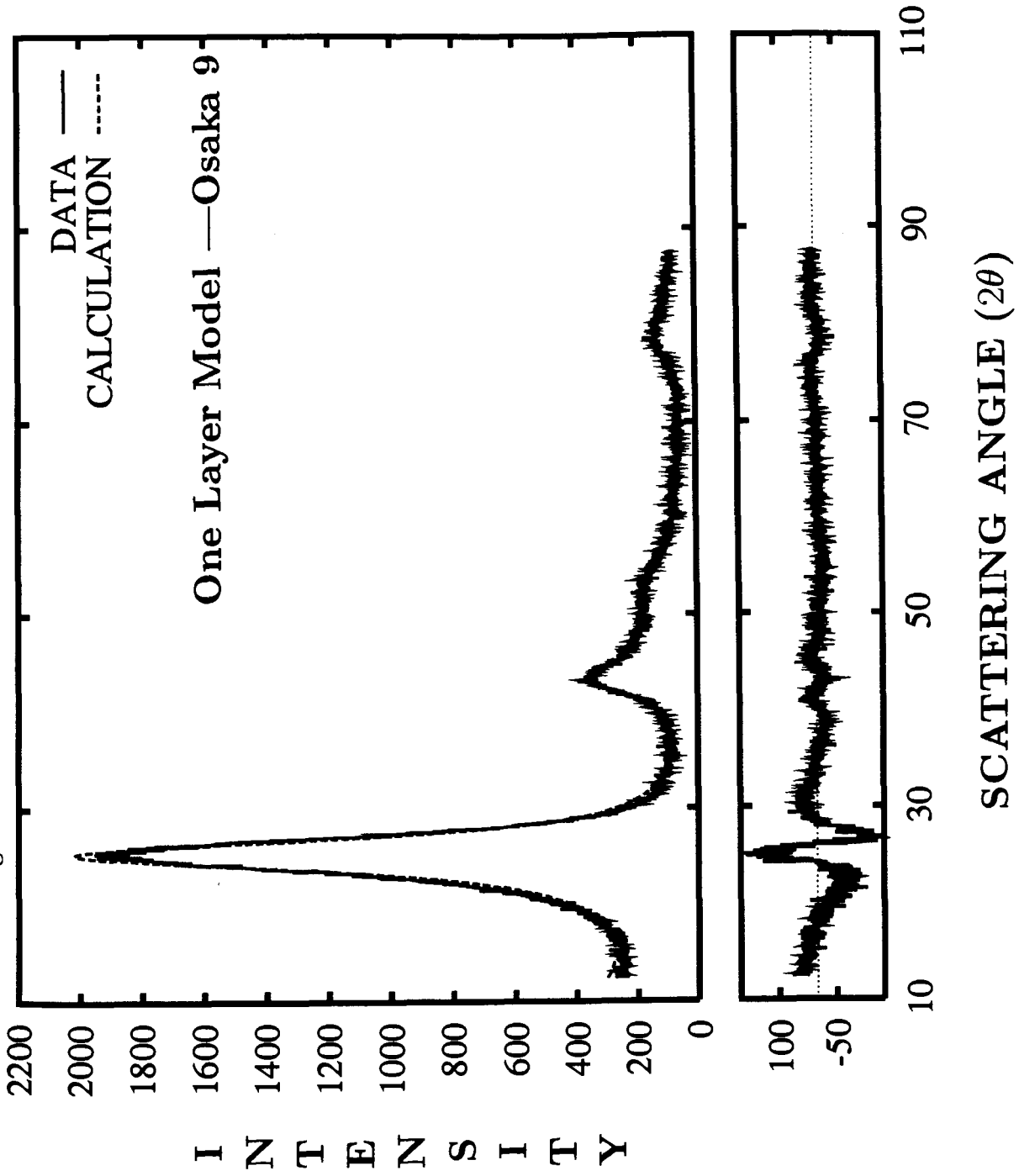
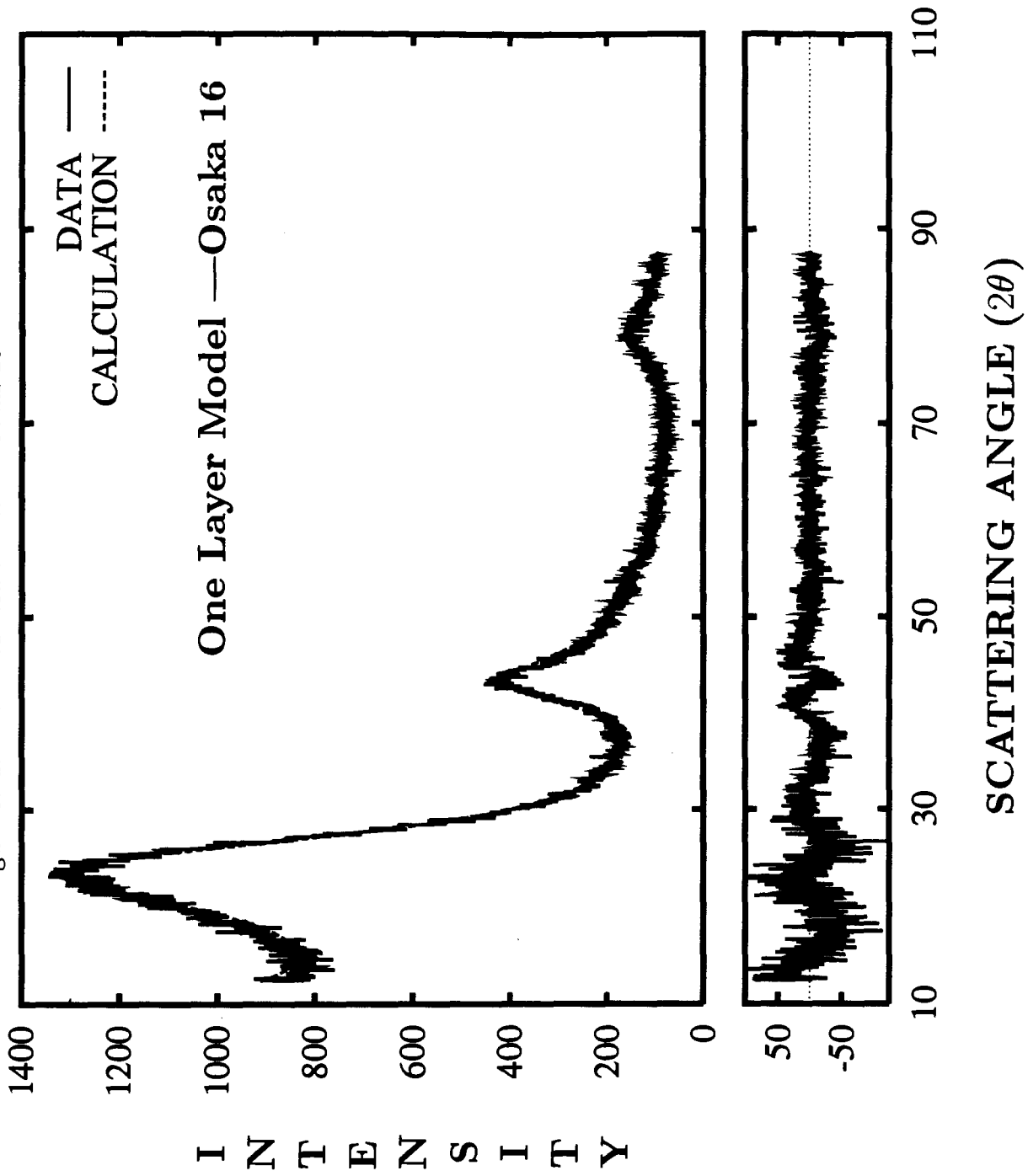


Figure 5.11: The Diffraction Pattern of Osaka 9

Figure 5.12: The Diffraction Pattern of Osaka 16



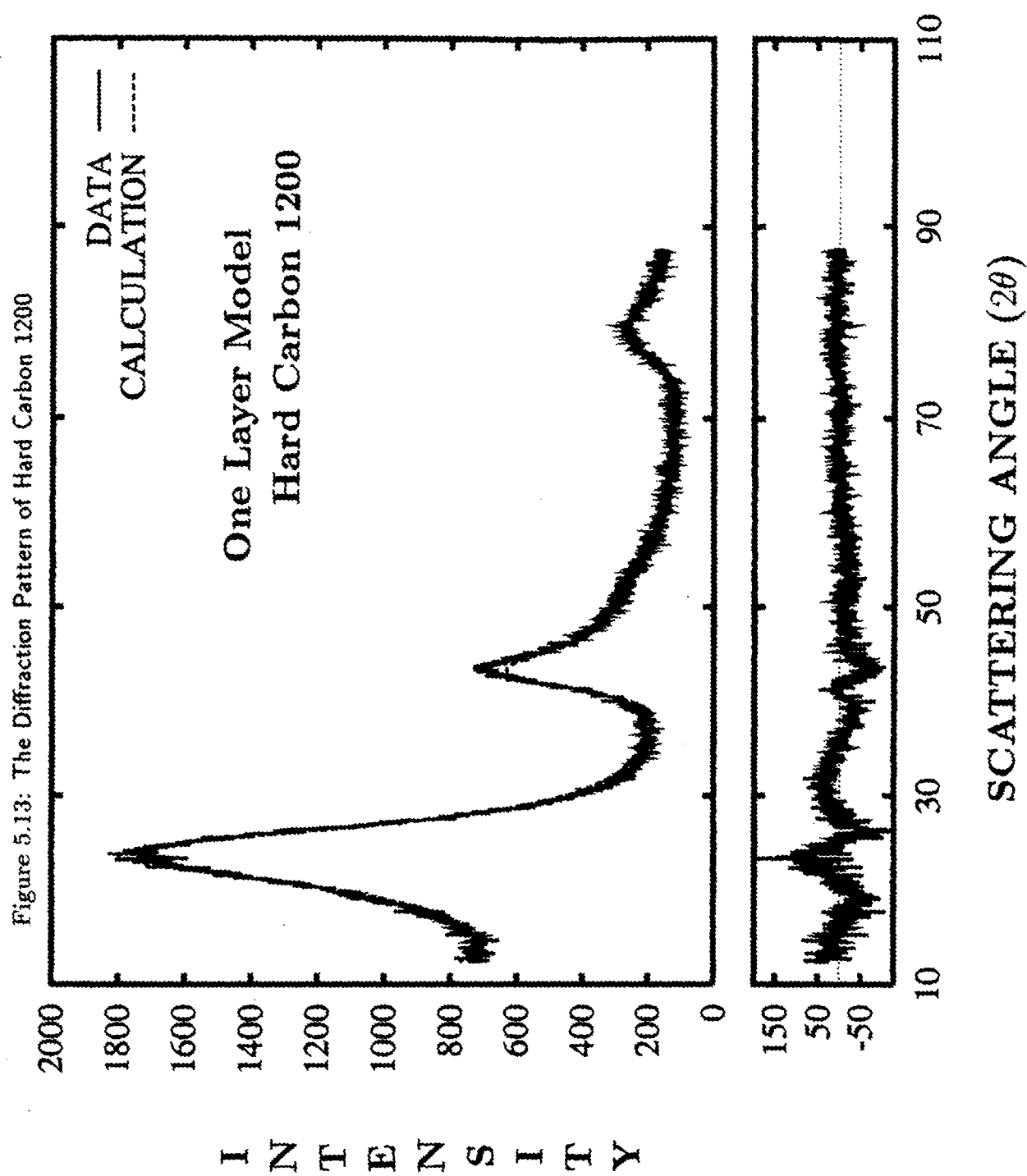
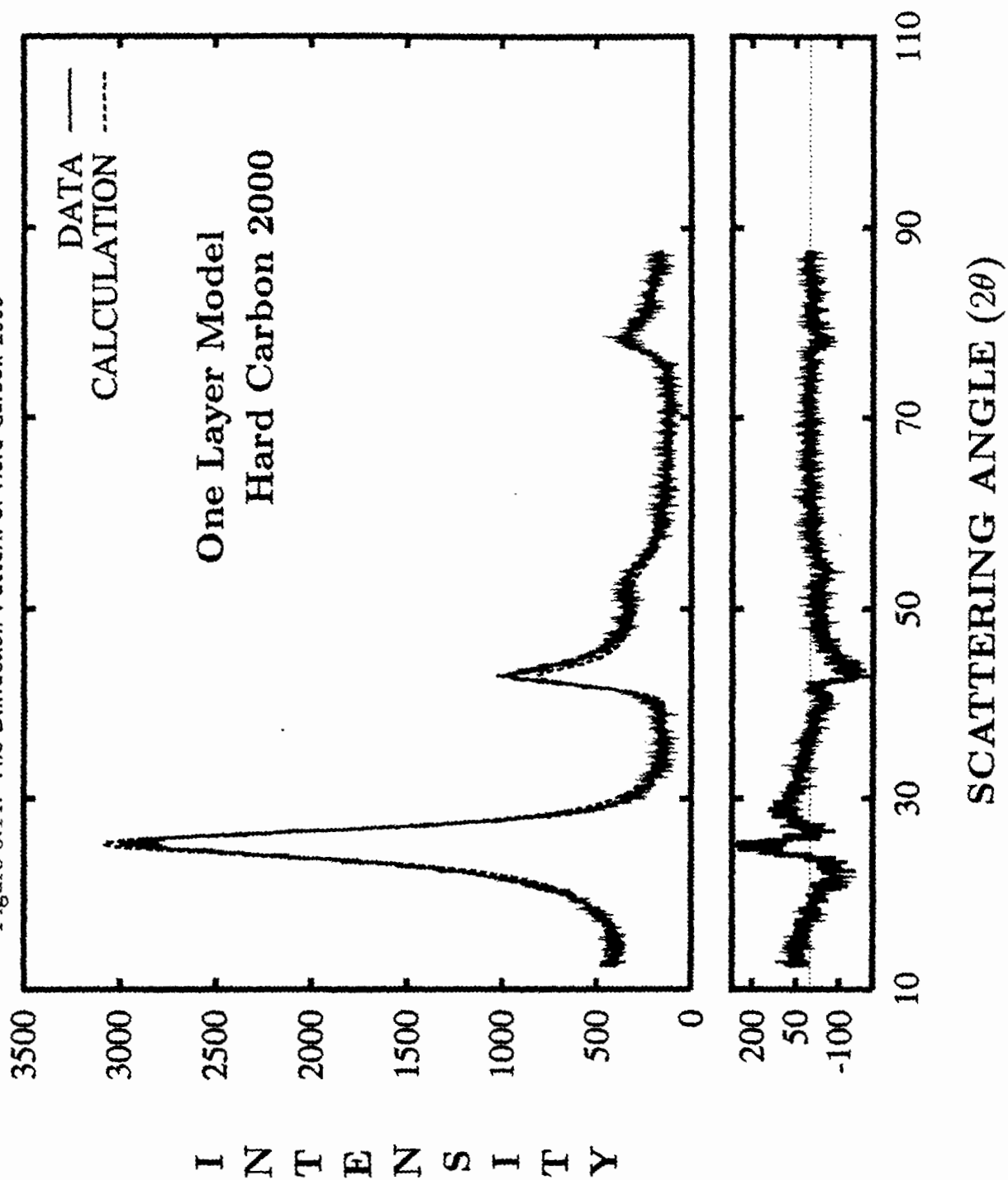
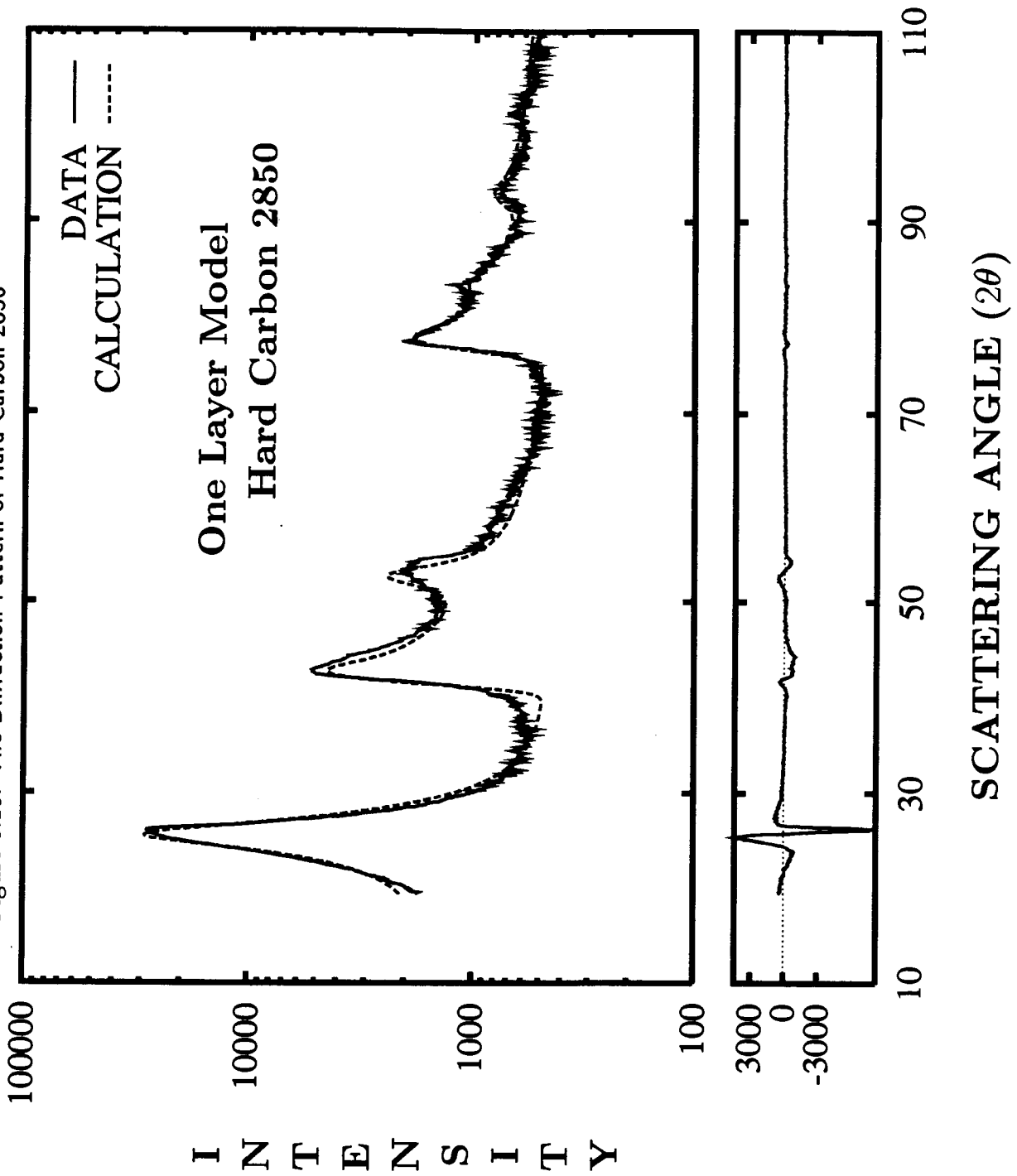


Figure 5.14: The Diffraction Pattern of Hard Carbon 2000







carbons have a high percentage of unorganized carbon. We can see that the fit for hard carbon 2850 is poor, particularly in the area of (00 $l$ ) peaks. This carbon has extremely asymmetric (00 $l$ ) peaks compared with other samples. Our model may be too simple for a highly asymmetric X-ray profile. For this complicated, highly strained hard carbon, the model only reflects the basic structural features and the refined parameters may not be reliable.

## 5.5 Hard Carbons Synthesized From Furfuryl Alcohol At Moli

Zhong et al [56] have synthesized another hard carbons series at Moli Energy (1990) Ltd.. These carbons were made by the pyrolysis of various polyfurfuryl alcohol (PFA) precursors. Liquid furfuryl alcohol (FA) is polymerized using phosphoric, oxalic or boric acid as catalysts. The monomer was mixed with 50% by volume of benzene and polymerized at 85°C by adding 5% volume of the chosen acid.

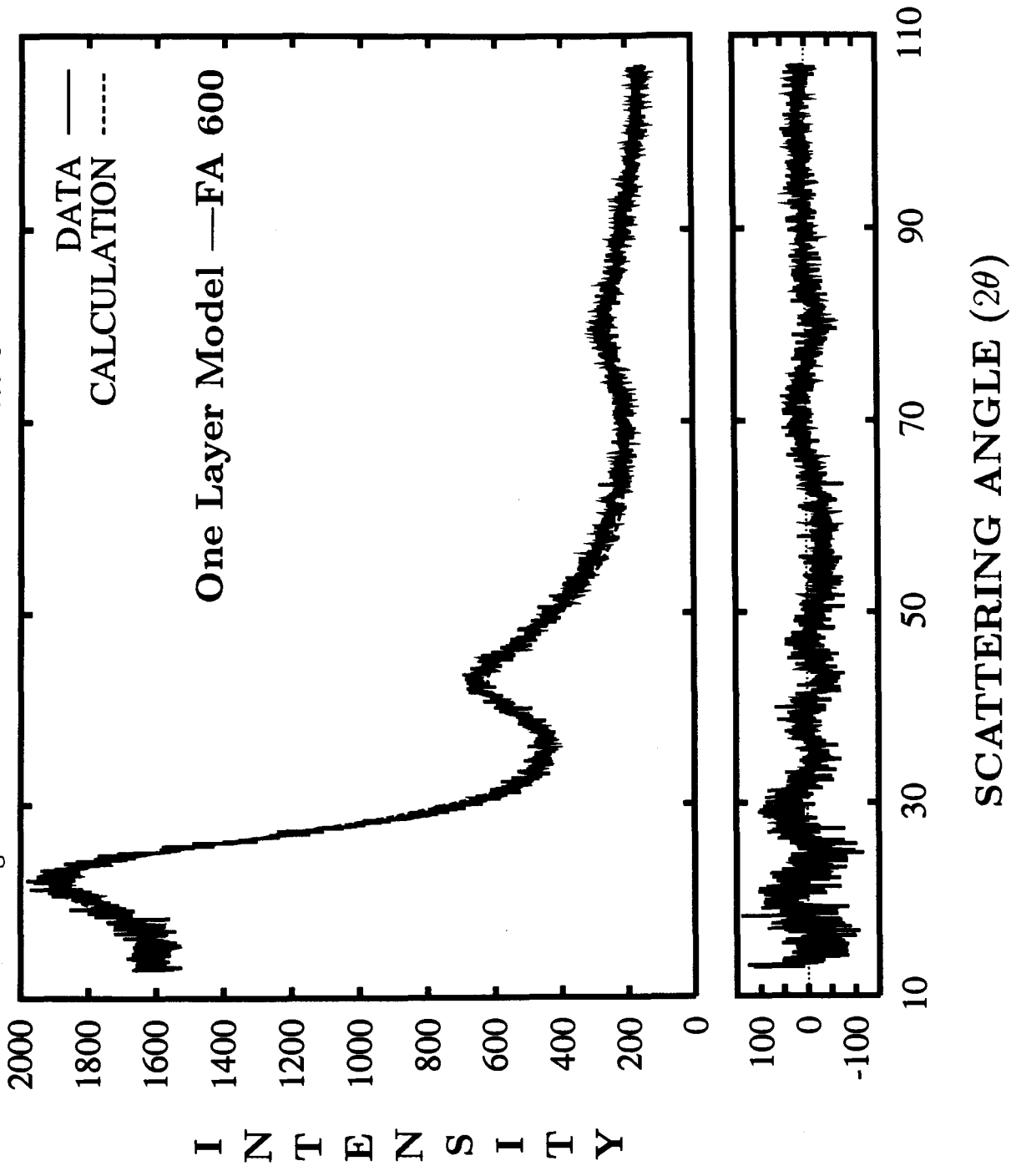
Table 5.6: The Structural Parameters and Selected Correlation Percentages for the Three FA Hard Carbons

Quantity	FA 600	FA 900	FA 1100
$\chi^2$	2.0	1.2	3.4 <sup>+</sup>
$d_{002}$ (Å)	3.408(1)	3.443(1)	3.503(3)
$a$ (Å)	2.428(1)	2.429(1)	2.441(1)
$P$	1*	1*	1*
$g$	0.13(1)	0.07(1)	0.20(1)
$\zeta$	0.107(1)	0.041(1)	0.027(1)
$\sqrt{\langle \delta \rangle^2}$ (Å)	1.18(1)	0.99(1)	1.06(1)
$M$	40*	40*	40*
$L_a$ (Å)	20	21(2)	29(3)
Corr( $g, \delta$ )	36%	95%	94%
Corr( $L_a, \zeta$ )	97%	97%	97%

\* Fixed during the refinement.

+ Data collected with better signal to noise than the other samples.

Figure 5.16: The Diffraction Pattern of FA 600°C



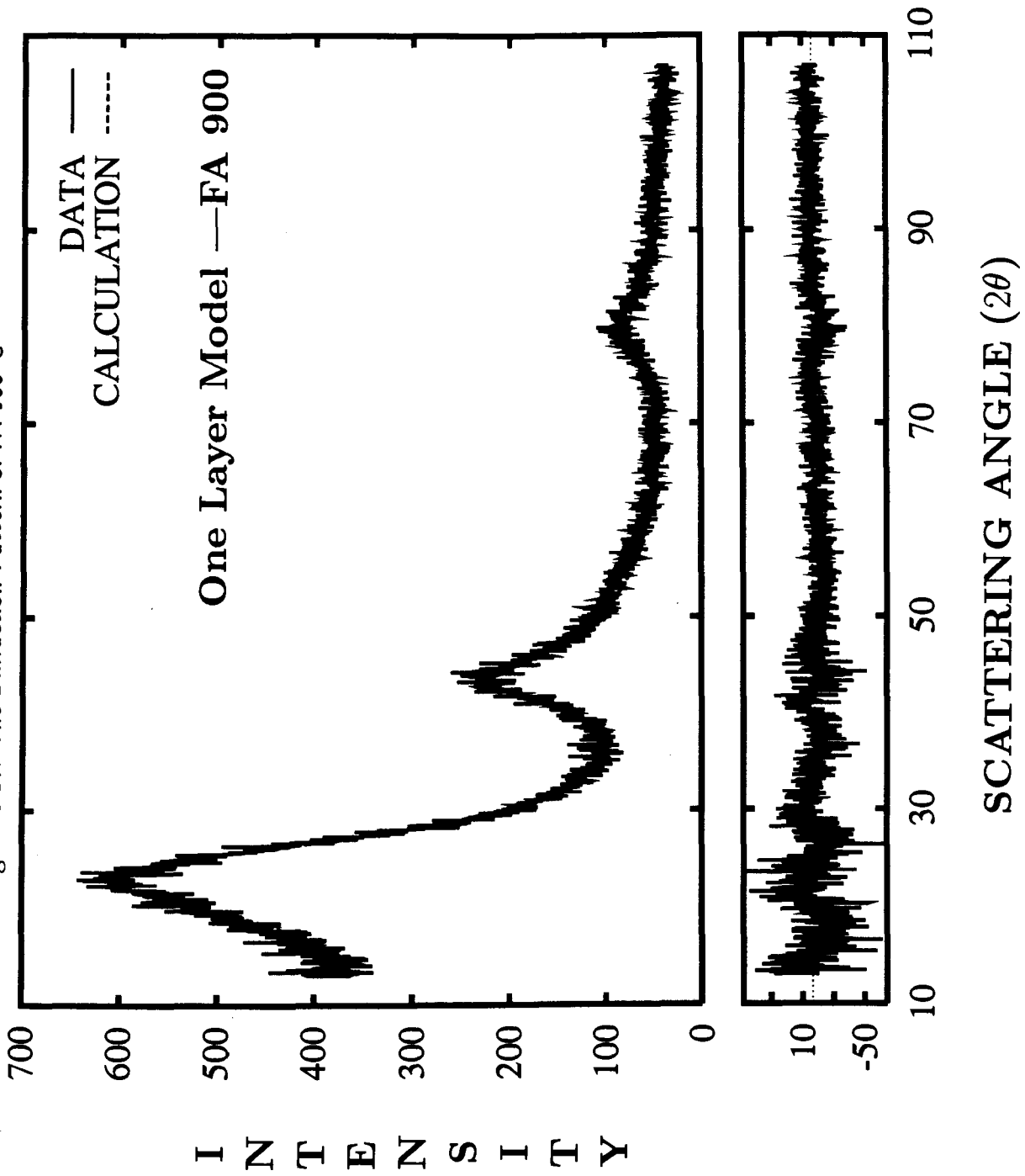


Figure 5.17: The Diffraction Pattern of FA 900°C

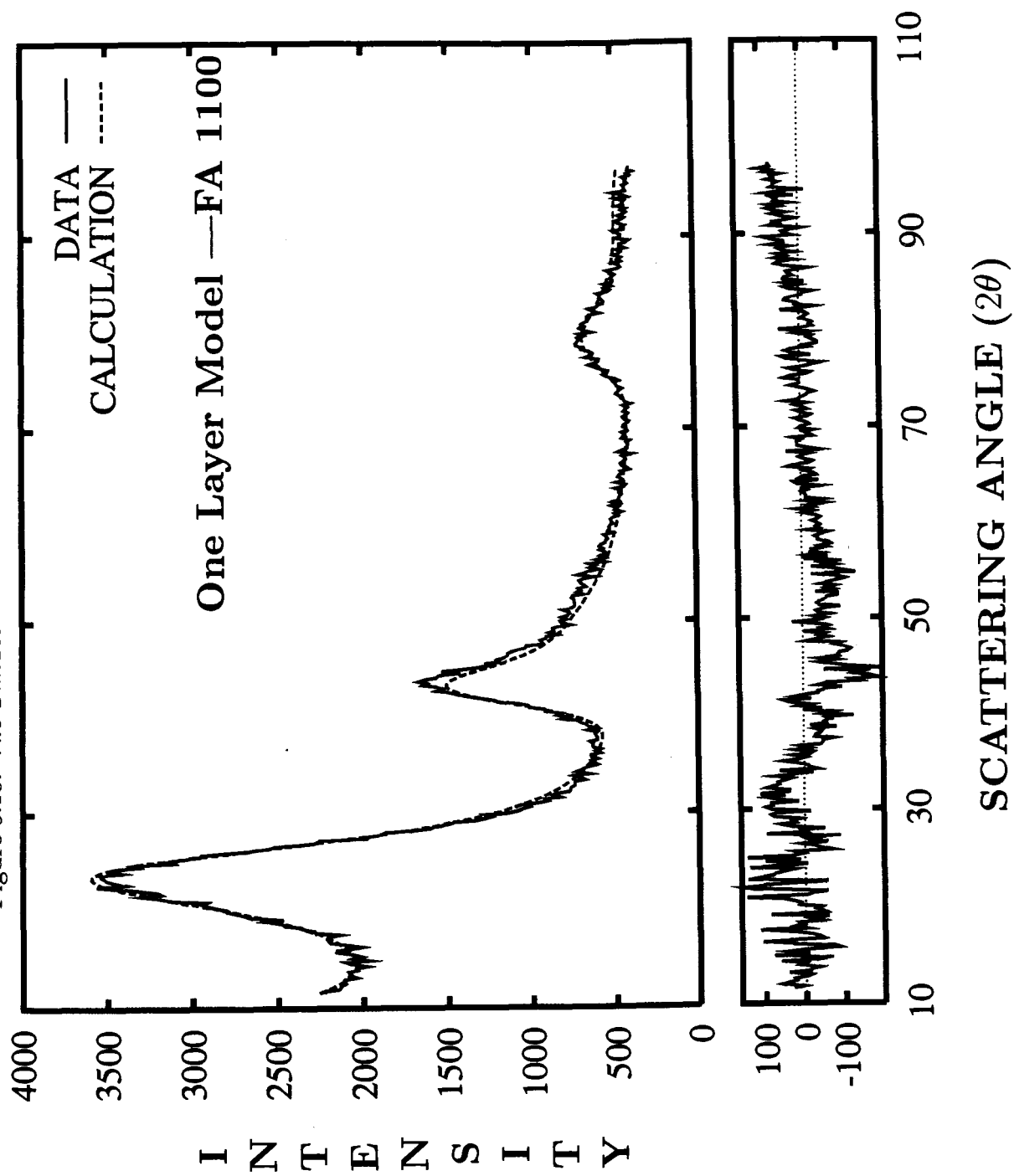


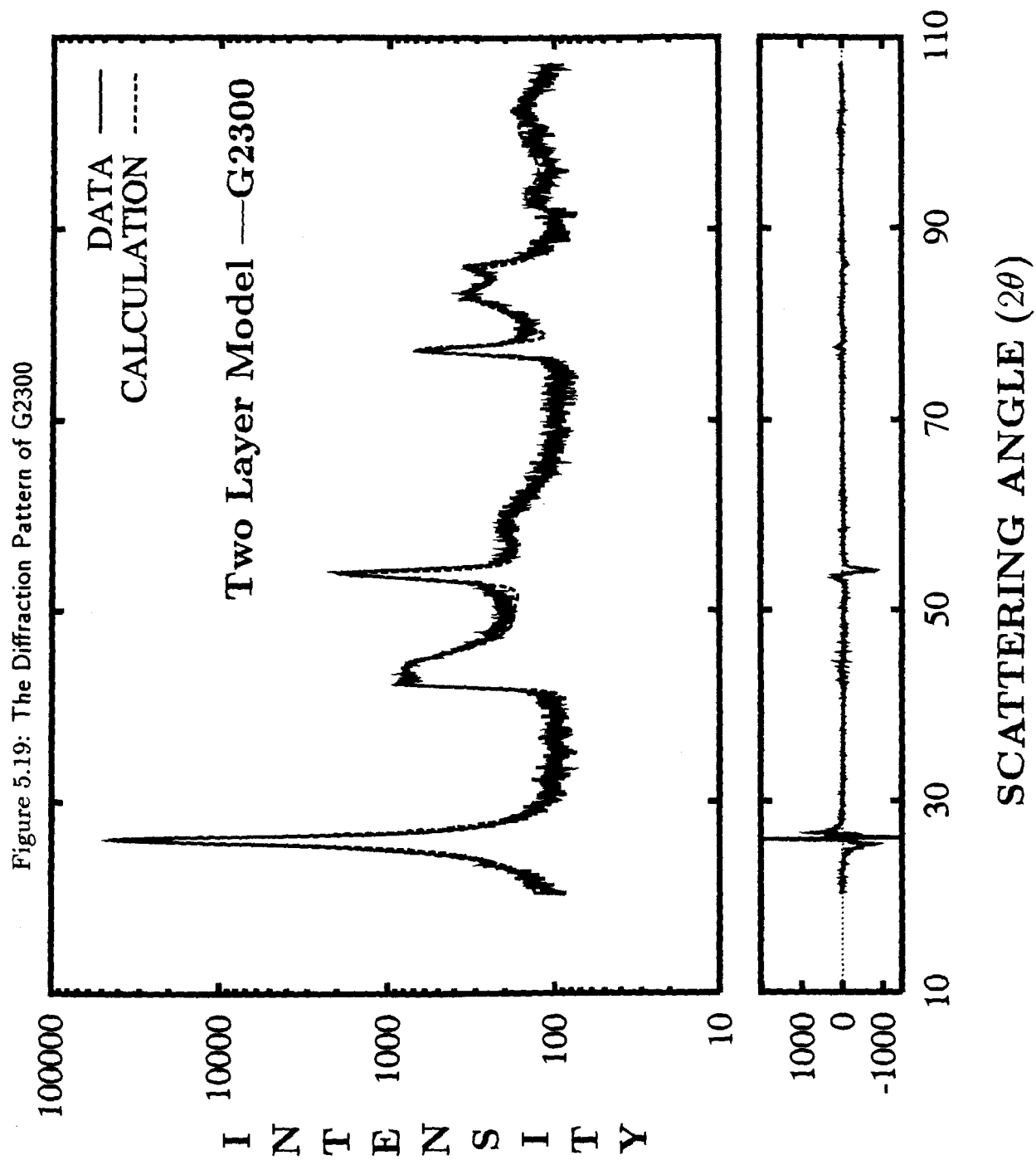
Figure 5.18: The Diffraction Pattern of FA 1100°C

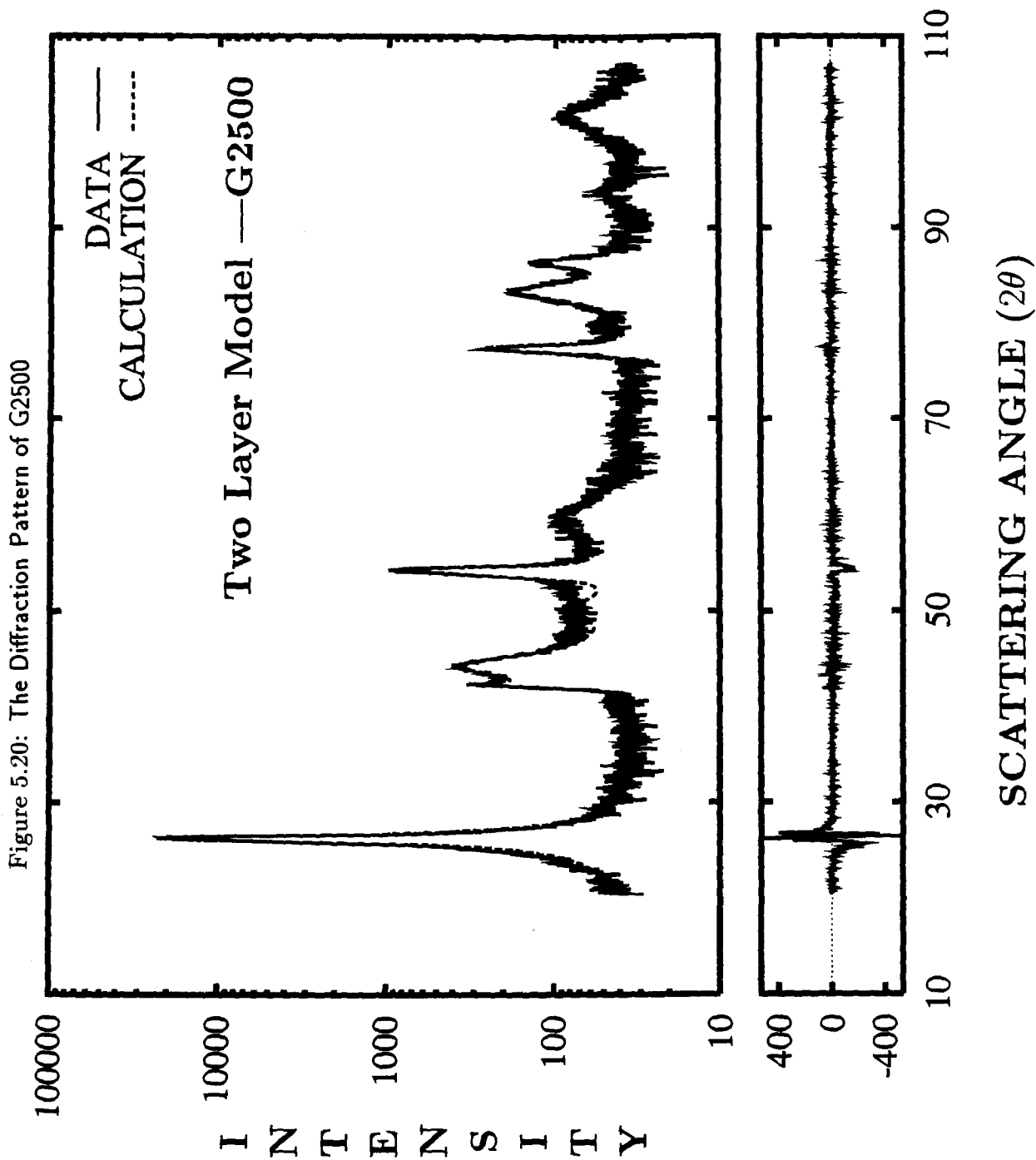
The resulting solid black polymer was then heated in argon at 600, 900 and 1100°C for 2 hours, similar to that described in reference [57]. The product was then ground using a mortar and pestle to below 200 mesh (less than 75  $\mu\text{m}$  particle size). The carbon made using phosphoric acid catalyst shows the best cell performance [56]. Therefore, we will only show these carbons made with phosphoric acid catalyst as examples here. We call these carbons FA600, FA900 and FA1100. Figures 5.16 to 5.18 show the data, theory and difference profile (one layer model) for FA 600, FA 900 and FA 1100. All X-ray patterns have been fitted by fixing  $P = 1$  and  $M = 40$ . The correlation between  $g$  and  $\delta$  is high as for other low temperature carbons. The reason for the high correlation between  $L_a$  and  $\zeta$  is that the X-ray patterns of these highly disordered carbon strongly depend on the structure of layer through the second strong peak (100) in these X-ray profiles. Both  $L_a$  and  $\zeta$  describe the layer structure. The parameters and fits are reasonably acceptable (see the table 5.6).

## 5.6 A Graphitic Carbon Series

Finally, we will show a series of graphitic carbons studied using the two-layer model. These graphitic carbons were made at Moli Energy by heating the same raw material (Osaka 10) to different temperatures, 2100, 2300, 2400, 2500, 2600, 2700 and 2800°C. We will call them G2100 etc., respectively. 2800°C is the highest temperature attainable in Moli's furnace. From our experience with the Conoco carbons, we know that soft carbons heated above 2200°C are well described by the two layer model. The electrochemical data collected by A.K. Sleight at Moli also shows that there is a clear transition in cell capacities around 2200°C (see the next chapter). We show the refined results of three selected carbons from this series, G2300, G2500 and G2800, in figures 5.19 to 5.21. The fits are excellent. In table 5.7, we list the refined parameters for all 6 graphitic carbons examined by the two layer model. G2100 is not listed in the table since it is not suited to the two layer model. It can be fitted well using the one layer model.

Graphitic carbons are presently believed to give the best performance for lithium ion cell anodes. This will be discussed further in the next chapter.







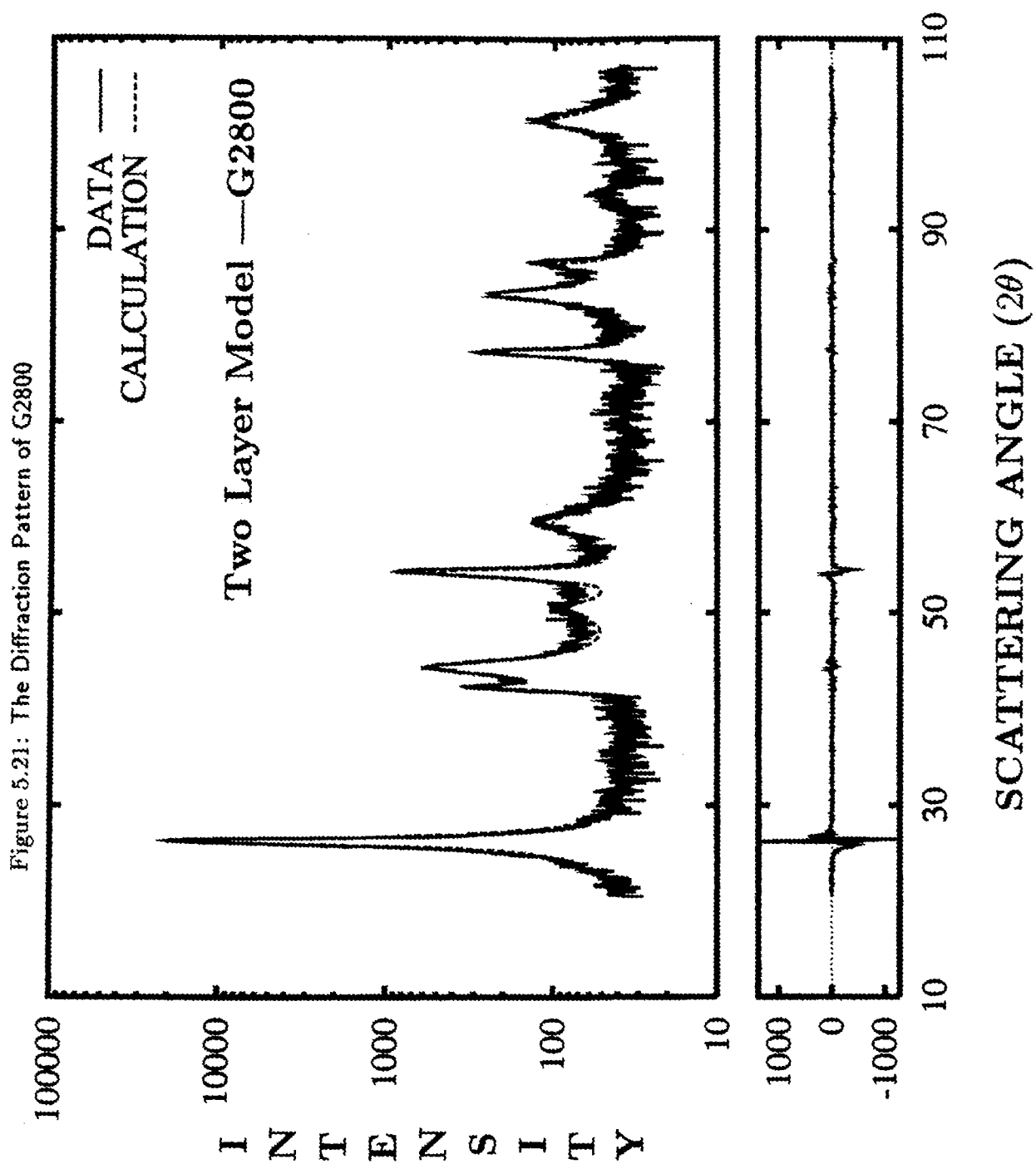


Table 5.7: The Structural Parameters and Selected Correlation Percentages of the Six Graphitic Carbons Studied by the Two Layer Model

Quantity	G2300	G2400	G2500	G2600	G2700	G2800
$\chi^2$	7.6	8.4	2.9	10.0	27.1	4.6
$d_{002}$ (Å)	3.391(1)	3.374(1)	3.369(1)	3.372(3)	3.368(1)	3.373(1)
$a$ (Å)	2.461(1)	2.459(1)	2.460(1)	2.460(1)	2.460(1)	2.461(1)
$P^+$	0.77(1)	0.61(1)	0.47(1)	0.42(1)	0.38(1)	0.29(1)
$P_t^+$	0.061(4)	0.110(2)	0.141(5)	0.126(3)	0.114(1)	0.128(5)
$g$	NA	NA	NA	NA	NA	NA
$\zeta$	0*	0*	0*	0*	0*	0*
$\sqrt{\langle \delta \rangle^2}$ (Å)	0.077(1)	0.066(1)	0.061(1)	0.059(1)	0.054(1)	0.054(1)
$M$	38(1)	33.1(1)	50(1)	36.4(1)	36.7(1)	48(1)
$L_a$ (Å)	158(5)	153(4)	202(9)	180(4)	195(2)	191(7)
Corr( $M, \delta$ )	66%	62%	60%	58%	59%	
Corr( $P, P_t$ )	45%	42%	13%	16%	15%	18%

\* Fixed during the refinement.

+ The numbers have not been divided by two.

### 5.6.1 Summary and Comment

We have seen that our program works quite well for both soft and hard carbons. This program has been used for about one year on our SUN workstation and can handle all the carbons that we have tried. Although De Courville-Brenasin et al (1981) [58] described a program for disordered layer solids, in their work, the carbon chosen for study apparently was a two phase mixture. Despite this, fits were quite good. The paper describes the method of least squares refinement in detail, but gives only a single comparison with experiment. Therefore, it is difficult to judge the range of applicability of their program.

*“I believe that it is clear to anyone of ordinary skill in the art, that there are 3 general anode classes in this business. These are Li, Li alloys and Li insertion compounds. Which one is ‘best’ may not be obvious but I would fully expect everyone to consider and try using a Li carbonaceous material.”*

— D. Wainwright

## Chapter 6

# Carbon and Lithium Intercalation Cells

In the last chapters, we have studied the structures of various carbons in detail. The main motivation of this work is the search for the most suitable carbon for the anode of lithium ion cells. To predict the best carbon for battery electrodes, we must correlate structural information to electrochemical data for different carbons. This chapter describes the electrochemical measurements. First, test cell construction is described. The meaning of the cell voltage is discussed. A discussion of how carbon structure influences lithium intercalation is included. We will show that carbon structure plays a vital role.

### 6.1 Carbons and Anode Materials

Intercalation reactions involve the reversible insertion of a guest species, such as Li, into a host solid, such as carbon, with no significant alteration of the host structure

during the process (McKinnon & Haering (1982) [59]). Such an intercalation process is of fundamental importance in the so-called rocking chair approach, which uses two highly reversible intercalation compounds as electrodes (see the discussion in chapter one). In order to choose two intercalation compounds as electrodes for such a rocking chair cell, many factors have to be considered, for example, the relative voltage difference between the two compounds, the reversibility of the intercalation in each compound, the cell voltage and its variation versus the amount of intercalated Li in the host, the availability and cost of the compound, etc..

In the search for suitable electrodes, many inorganic materials have been proposed and tested on an empirical basis. Most of these did not survive in the contemporary battery world. Through thousands of tests (see Tsutomu Ohzuku's recent reprint on *Four-volt cathodes for lithium accumulators and the Li ion battery concept*[60]), people began to realize that the best cathode materials are expected to be transition metal dioxides,  $MeO_2$  (or  $LiMeO_2$ ,  $Me$  is transition metal). Among many possible transition metal dioxide choices,  $LiMn_2O_4$ ,  $LiCoO_2$  and  $LiNiO_2$  are the most popular candidates. At the same time, the search for the best anode material is occurring. The choice of anode materials is almost exclusively limited to carbons because of their advantages in many of basic requirements over other materials. Carbons have high reversibility, wide availability and low cost, etc.. The main subject of this chapter is to examine how the structure of carbons influences the intercalation of Li through performance, voltage profiles, reversibility and cell capacities.

## 6.2 Cell Voltage and Chemical Potential

How do we use electrochemical measurements to study the intercalation of Li in a host? The voltage of an intercalation cell is directly proportional to the chemical potential of the guest in the host [59]. It is this relationship that makes intercalation cells useful for studying the physics of intercalation. To see how this arises, consider a cell with a host, say carbon, as one electrode and Li metal as the other. Denote the chemical potential of Li in the host and in Li metal as  $\mu_c$  and  $\mu_c^0$ , respectively.  $Li^+$  has charge  $e$ , thus one  $Li^+$  is intercalated for one electron passed through the external

circuit. Since the electrons move through a potential difference  $V$ , the work done on the cell per ion intercalated is  $W = -eV$ . This work must be equal to the change in free energy of the two electrodes, which is  $\mu_c - \mu_c^0$ , so

$$-eV = \mu_c - \mu_c^0 \quad (6.1)$$

Thus measuring the cell voltage versus charge passed between the electrodes is equiva-

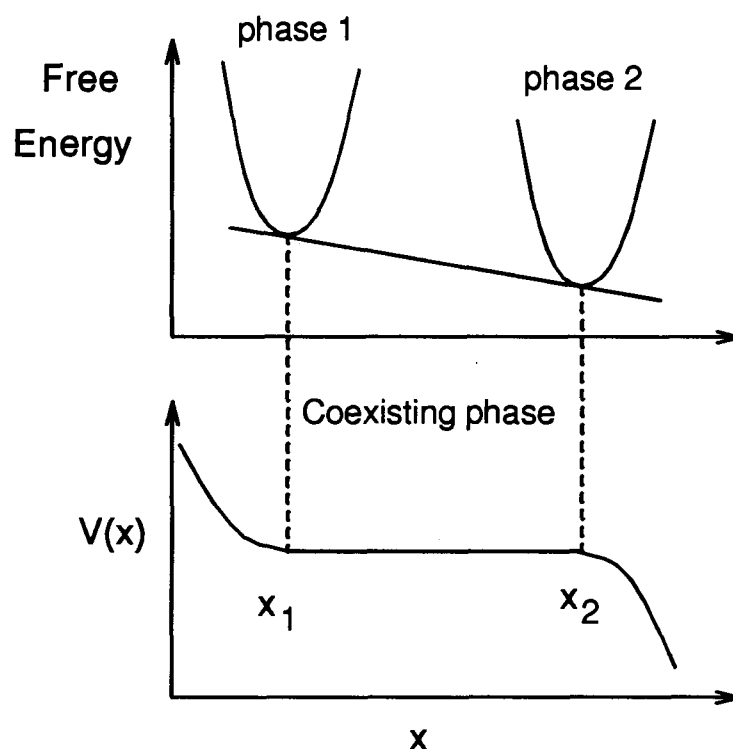


Figure 6.1: The relation between plateaus in  $V(x)$  and first order phase transitions

lent to measuring the chemical potential as a function of  $x$ , the Li concentration of the compound  $Li_xC_6$ . Thermodynamics requires that  $\mu_c$  increase with the concentration of guest ion, so  $V$  decreases as ions are added to positive electrode (carbon).

It is most convenient to measure  $V$  against Li metal since the composition of the lithium anode is fixed, hence  $\mu_c^0$  is constant. One can also scale  $\mu_c^0$  to zero for

simplicity. All changes in the cell voltage as the cell charges or discharges at constant temperature are due to the changes in  $\mu_c$ .

Features in  $V(x)$  typically occur on the scale of millivolts, and voltage is easily measured to microvolts. Thus  $V(x)$  can be measured accurately enough for the derivative  $-\partial x/\partial V$  to be calculated (The negative sign is needed because  $V$  decreases with  $x$ ). Subtle variations in  $V(x)$  are easier to see in the derivative.

The features in  $V(x)$  and  $-\partial x/\partial V$  reveal a great deal about the thermodynamics of a system. Assume that the free energy of the host as a function of  $x$  has two phases, as shown in figure 6.1 ( $< x_1$  is phase 1 and  $> x_2$  is phase 2). For any  $x$  between  $x_1$  and  $x_2$ , the system consists of small regions, called domains, of the two phases. Increasing  $x$  causes the domains of the phase with larger composition ( $x_2$ ) to grow at the expense of the phase of lower composition ( $x_1$ ). Such a transition between two phases is called a first order transition. Since the compositions of the coexisting phases do not change, the chemical potential is constant in this two-phase region.

In an electrochemical cell, the voltage should be constant in a two phase region, and  $-\partial x/\partial V$  should diverge. In practice, kinetic effects generally cause  $V$  to decrease slightly through the two-phase region, and so  $-\partial x/\partial V$  has a peak rather than a divergence.

## 6.3 Electrochemical Cell Construction and Cycling

### 6.3.1 Cathodes

The electrochemical cell is an excellent tool for exploring the intercalation physics of carbons. The cell contains two electrodes and an electrolyte. Figure 6.2 shows the construction of our experimental electrochemical cells. 2325 coin-type cells were constructed using the carbon as the cathode, 125  $\mu\text{m}$  thick lithium foil as the anode (Lithium Corporation of America), porous polypropylene as the separator and a nonaqueous electrolyte (see next section for details). A stainless-steel spacer and a disc spring were included so that about 14 bar of *stack pressure* was exerted on the

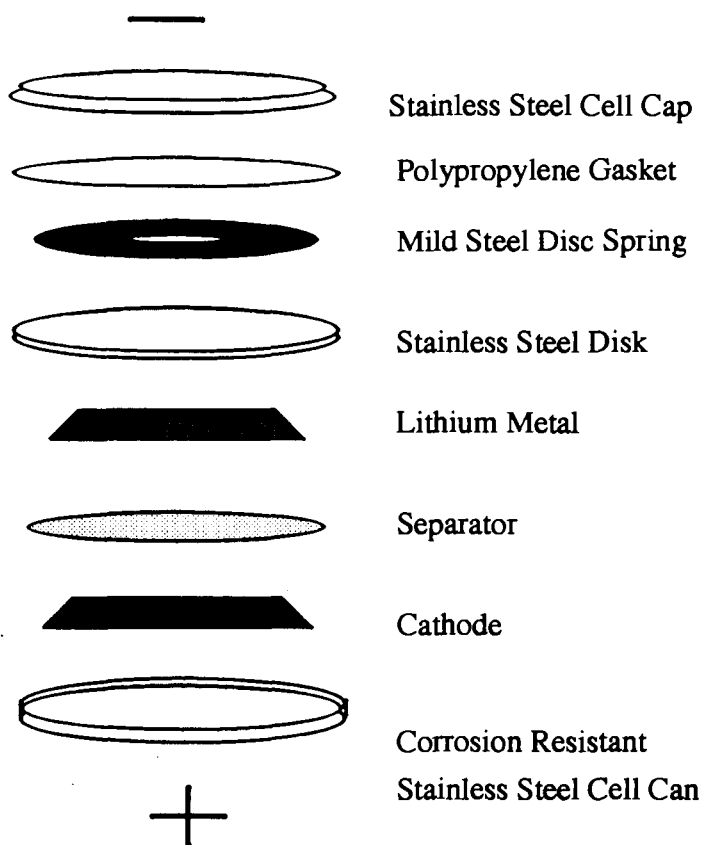


Figure 6.2: Exploded View Of a Typical Lithium Coin Cell

electrode stack to ensure good contact of carbon particles to the current collector. Cell assembly and closure were done in an argon filled glove box.

The carbon cathodes were made as following. First electrode slurries were prepared by mixing 5% by weight Super-S carbon black ( Chemetals Baltimore Md. U.S.A.) with the carbon powder and with binder solution. The binder solution is a 4% by weight solution of EPDM ( ethylene propylene diene terpolymer) in cyclohexane. Enough binder solution was added to the powder so that 2% by weight EPDM remains in the electrode when the cyclohexane evaporates. The slurries were spread on the copper foil substrates with a doctor blade spreader so that the area mass density after drying was about 10-15mg/cm<sup>2</sup>. Then the electrodes were compressed with pressures



of about 100 bar. Our cells usually contain  $1.2\text{cm} \times 1.2\text{cm}$  electrodes with an active mass near 15mg.

The effect of the Super S carbon black is to help provide electrical contact between carbon grains and often improves the cycling behavior of Li/carbon cells after many cycles [61]. The Super S black does itself intercalate Li to about  $\Delta x = 0.5$  in  $\text{Li}_x\text{C}_6$  [62], so that its inclusion to a level of 5% by weight in some electrodes will affect measured values of  $x$  and  $x_{max}$  in those electrodes by about 3%. ( We treat the Super S Black as an inactive material in these studies for simplicity).

### 6.3.2 Electrolyte

Electrolytes are substances that contain mobile ions, which can be solids (like in a solid polymer battery) or liquids. Liquid electrolytes can be divided into two classes: aqueous and nonaqueous. Nonaqueous electrolytes are used in Li ion cells, which is due to the violent reactivity between lithiated carbon and water.

We used two nonaqueous electrolytes in our study. The first, suitable for disordered carbons, was 1 M  $\text{LiN}(\text{CF}_3\text{SO}_2)_2$  salt (3M Corporation) dissolved in a 50:50 volume percent mixture of ethylene carbonate (EC) (Texaco) and dimethoxyethane (DME). DME was distilled from lithium benzophenone. (All solvents were obtained from Moli Energy (1990) Ltd.). The moisture content of the electrolyte was less than 100 parts per million (ppm). For carbons heated to  $2000^\circ\text{C}$  or above, the electrolyte used was a 1M solution of both 12-Crown-4 ether and  $\text{LiN}(\text{CF}_3\text{SO}_2)_2$  (3M Corporation) salt dissolved in a 50:50 volume percent mixture of propylene carbonate (PC) and EC.

Simple electrolytes containing PC as the sole solvent do not work well in Li/graphite cells because Li ions solvated by PC co-intercalate between the graphite layers [8]. Apparently the addition of EC to the electrolyte changes the solvation cloud about the Li ion enough to almost entirely suppress co-intercalation. Since EC is a solid at room temperature, EC containing electrolytes are normally based on multisolvent blends for convenience. The 12-Crown-4 apparently coordinates the  $\text{Li}^+$  ion in such a way so that solvent co-intercalation is minimized [63]. Without 12-C-4, some solvent cointercalation will occur when 1M  $\text{Li}(\text{CF}_3\text{SO}_2)_2/\text{PC}/\text{EC}$  electrolyte

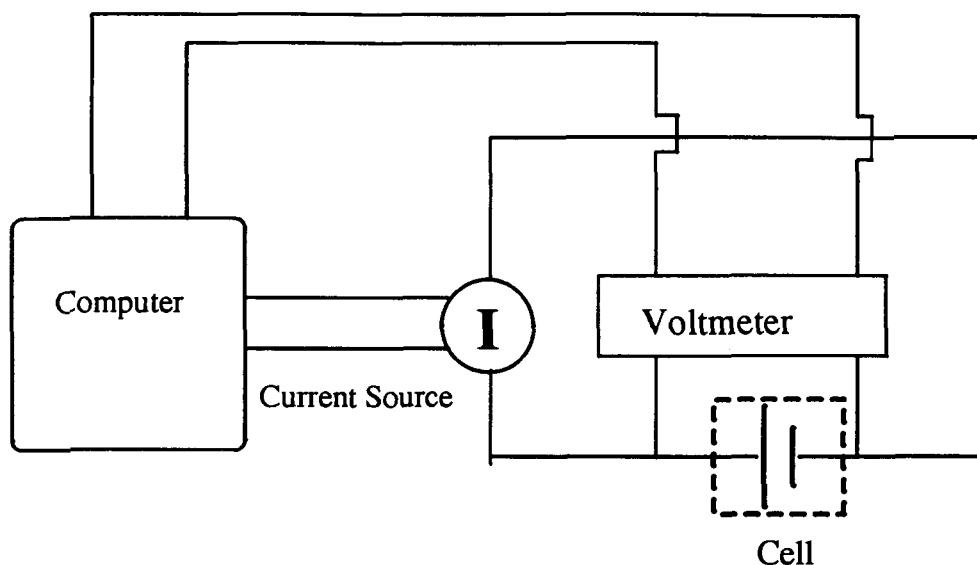


Figure 6.3: Schematic of charger circuit

is used in cells with highly graphitic carbon electrodes (see the discussion in section 6.4). We used the electrolyte with 12-C-4 for all soft carbons heated to 2000C° or above to be sure cointercalation would not be a problem.

Solvent co-intercalation does not occur in petroleum coke or disordered carbons when PC-based electrolytes are used [8, 14].

### 6.3.3 Cycling

All cell testing was done using computer-controlled constant current cyclers. The charge and discharge currents were selected, based on the active mass of the carbon electrode, so that a change,  $\Delta x = 1$ , in  $Li_xC_6$  would take 80 hours. We call this an 80 hour rate. This slow cycling rate was chosen so that the intercalation would be close to equilibrium. For a typical carbon electrode with an active mass of 15 mg, an area of 1.44cm<sup>2</sup>, and a thickness of about 100 microns, an 80 hour rate corresponds to a current of 69.4  $\mu$ A and a current density of 48 $\mu$ A/cm<sup>2</sup>. All data presented in this thesis is for cells tested at 30°C. Data were logged whenever the cell voltage changed by more than 0.005 volts. The derivative,  $dx/dV$ , was calculated from  $V(x)$  by taking

finite differences between adjacent data points. Although  $dx/dV$  is always negative, in our presentations of cell data later, we show  $dx/dV$  to be positive during charge for clarity and for comparison to linear sweep voltammetry. The charger circuits are schematically shown in figure 6.3.

## 6.4 Li Intercalation in Graphite

Li intercalation in graphite was discovered by Herold in 1955 [64]. Since then there have been many studies of  $Li_xC_6$  ( $0 < x < 1$ ) [65, 66]. J. R. Dahn and his co-workers made a series of careful studies on lithium intercalation into petroleum cokes and graphite using nonaqueous electrolyte cells [8] (Some of that work recently has been reexamined by Shu et al [61].) In the following two sections we mainly focus on the discussion of irreversible capacity loss and guest staging.

### 6.4.1 Irreversible Capacity

Figure 6.4 shows the first one and half cycles of a Li/graphite (Lonza KS 44) cell at an 100 hour rate. The electrolyte used in cell was 1 M  $LiN(CF_3SO_2)_2$  and 1 M 12-Crown-4 dissolved in 50:50 volume PC and EC solvent. Right after the cell is assembled, the open circuit cell voltage is typically above 2.5V. During the first discharge, the cell voltage initially drops rapidly until about 0.8V where it shows a plateau for a considerable amount of time. The plateau is attributed to the reaction of Li atoms at the graphite surface with electrolyte to form a passivation film of reaction products [8]. This ionically conducting and electronically insulating film then prevents further reaction with electrolyte.

Several electrolyte decomposition mechanisms have been proposed for PC-based electrolytes [67, 68]. Initially a few possible processes are equally likely [61], then as the reactions proceed, the lithium alkyl carbonate film starts to form on the graphite surface and thickens. Electron transfer through the film to the solvent becomes increasingly difficult. Eventually, when the passivation film thickness reaches a critical value (of order around  $50\text{\AA}$ [8], which is the order suggested by Peled [69]), further

electron transfer is prevented and decomposition reactions stop. The cell reaction starts to change to reversible lithium intercalation.

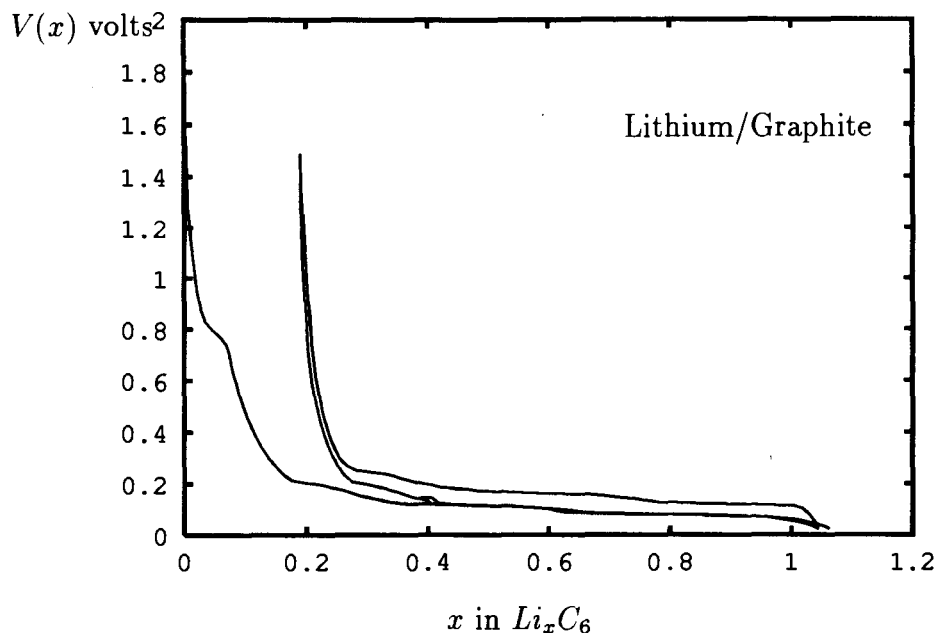


Figure 6.4: The first cycles of a Li/graphite cell at a 100 hour rate. The electrolyte used was 1M  $LiN(CF_3SO_2)_2$  and 12-Crown-4 dissolved in 50:50 PC and EC.

The irreversible capacity loss during the first discharge due to the decomposition of electrolyte depends on the choice of electrolyte [8]. For example, with 12-Crown-4 ether addition, the decomposition reactions are suppressed to 20 to 30% of the theoretical capacity (see e.g. figure 3 in [61]). Crown ethers are good chelating reagents for lithium ions. They will compete with electrolyte solutions for lithium ion coordination sites and win. Furthermore, because of the large sizes of crown ethers, they are not easy to cointercalate into graphite layers, thus preventing excessive amounts of electrolyte decomposition. The offset between charge and discharge in figure 6.4 is caused by the internal resistance of the cell. After the first cycle, all irreversible electrolyte decomposition reactions have stopped. Then, the charge and discharge

capacities of the cell are equal within 2% [8]. The main reversible intercalation of lithium in graphite is below about 0.2V. The plateaus in  $V(x)$  are more easily identified when the derivative  $-dx/dV$  is plotted versus  $V$  (see figure 6.5,  $\frac{I}{|I|}\sqrt{|dx/dV|}$  is used here only for clarity, where  $I$  is the charge (+) or discharge (-) current).

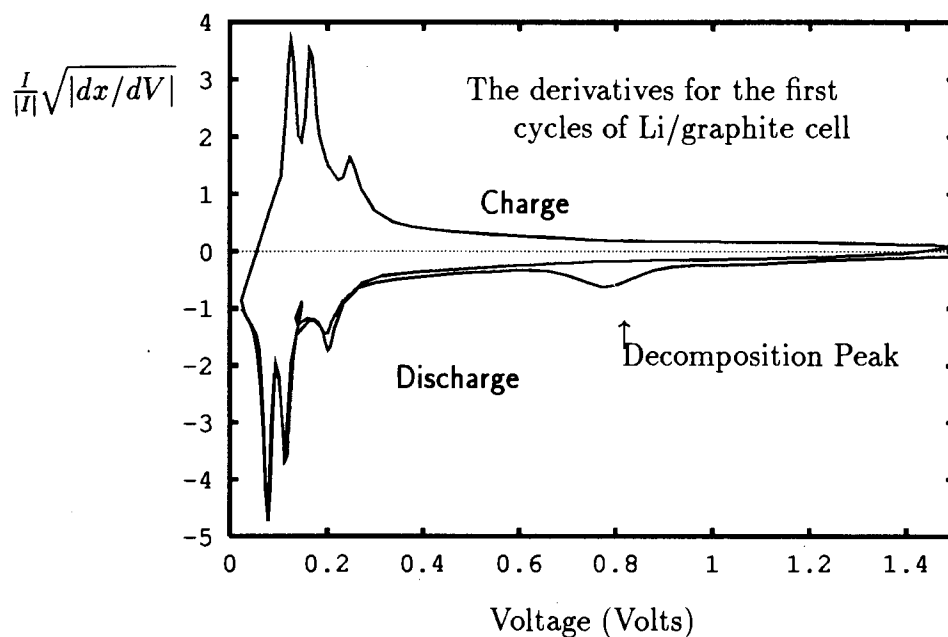


Figure 6.5: The square root of the derivative of  $-dx/dV$  for the first cycles of a Li/graphite cell at a 100 hour rate. The electrolyte used was 1M  $LiN(CF_3SO_2)_2$  and 12-Crown-4 dissolved in 50:50 PC and EC.

As we discussed, plateaus in  $V(x)$  and peaks in  $-dx/dV$  can mean that the intercalation compound exists as a mixture of coexisting phases over some range of  $x$ . However, some peaks in  $-dx/dV$  can be caused by other phenomena, for example, the peak in  $-dx/dV$  during the first discharge near 0.8V corresponds to the reaction of Li and electrolyte at the graphite surface. We will talk about the coexistence phase regions seen at lower voltage in the next section.

### 6.4.2 Staging

What are the coexisting phases regions indicated by the peaks of figure 6.5? Consider a Li/graphite cell which is fully discharged to zero volts, where the graphite electrode has the composition  $Li_1C_6$ , the maximum amount of Li which can be intercalated into graphite. Where exactly do these lithium atoms reside in graphite? Furthermore, what happens if the cell discharges only half way, say to  $Li_1C_{12}$ ? What is the difference between the lithium distribution of the two states,  $Li_1C_6$  and  $Li_1C_{12}$ ? These questions are all related to how the intercalated lithium atoms are arranged.

To answer these questions brings us to another interesting aspect of Li intercalation in graphite — staging, i.e. a particular type of ordering of guests in layer compounds. Simply speaking, stage  $n$  order is a sequence of  $n$  graphite layers and 1 intercalant layer[70] (see figure 6.6).

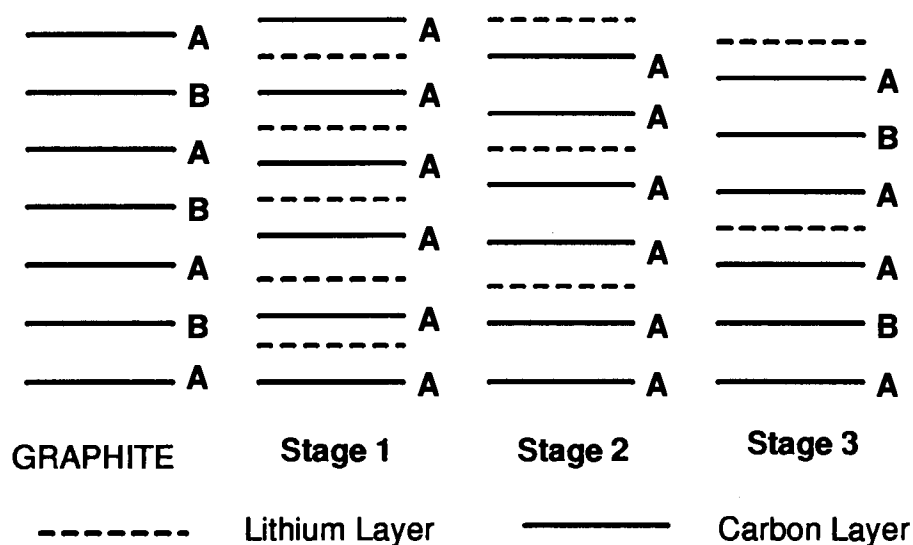


Figure 6.6: Staging of lithium intercalated graphite compounds

Staging is not limited to lithium intercalated graphite, it is a general phenomenon observed in layered intercalated compounds,[71, 72, 73, 74, 75]. We are not planning to discuss the details here, instead, giving some physical arguments to help the reader

understand this phenomenon.

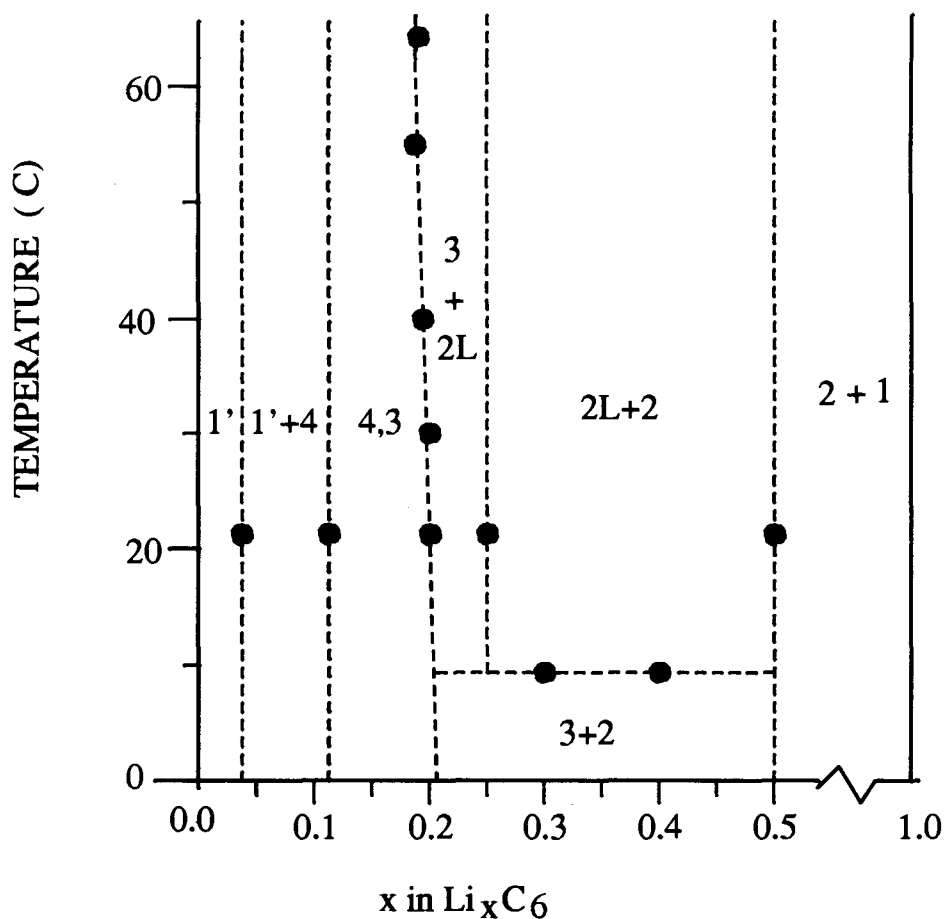


Figure 6.7: A Phase Diagram for  $\text{Li}_x\text{C}_6$  from Dahn (1991)

Since Li prefers to form Li-carbon bonds over Li-Li bonds to reduce energy, lithium will spontaneously intercalate into a graphite host at the beginning. During intercalation, the layers are pushed apart as Li fills the Van der Waals spaces (e.g.  $d_{002}$  changes from  $3.35\text{\AA}$  for graphite to  $3.70\text{\AA}$  in  $\text{LiC}_6$  see [14]). Because of the elastic energy associated with separating the layers, Li will find it *easier* to intercalate into layers already partially occupied. This can be thought of as an attractive interaction between Li atoms in the same gallery. There is simultaneously a short range

screened-coulomb interaction between intercalants which is repulsive.

The combination of the elastic interaction produced by strain and the screened coulomb intercalation between Li atoms produces complicated attractive or repulsive forces between Li atoms depending on their location. Guest atoms intercalated in the same host layer usually attract one another, while guest atoms in different layers usually repel. This leads to an ordered arrangement of guest atoms, that is, staging, where the regions of high and low density alternate in an ordered way.[74]

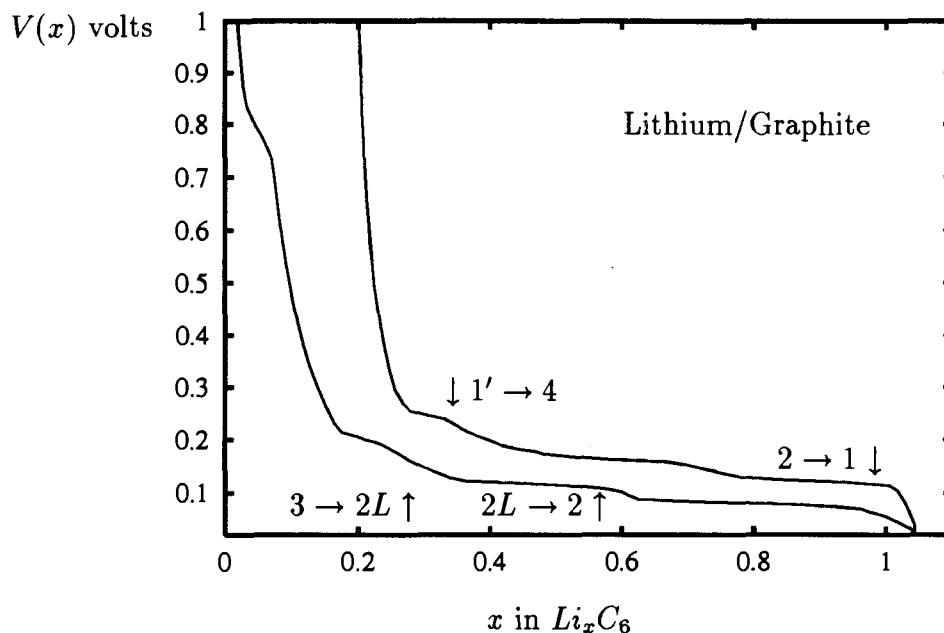


Figure 6.8: Showing the signature of phase transitions between staged phase in the voltage profile of Li/graphite cell

The experimental phase diagram of  $Li_xC_6$  [76] is included (see figure 6.7) for later reference. The phase notations in the figure have been explained in [76]. Considering the phase diagram of figure 6.7, the phase transitions for a complete discharge of lithium/graphite cell is following: (1) dilute stage-1 → stage-4; (2) stage-3 → stage-2L; (3) stage-2L → stage-2 (4) stage-2 → stage-1, which are indicated in figure 6.8 in



a typical lithium/graphite voltage profile.

## 6.5 Lithium Intercalation in Disordered Carbons

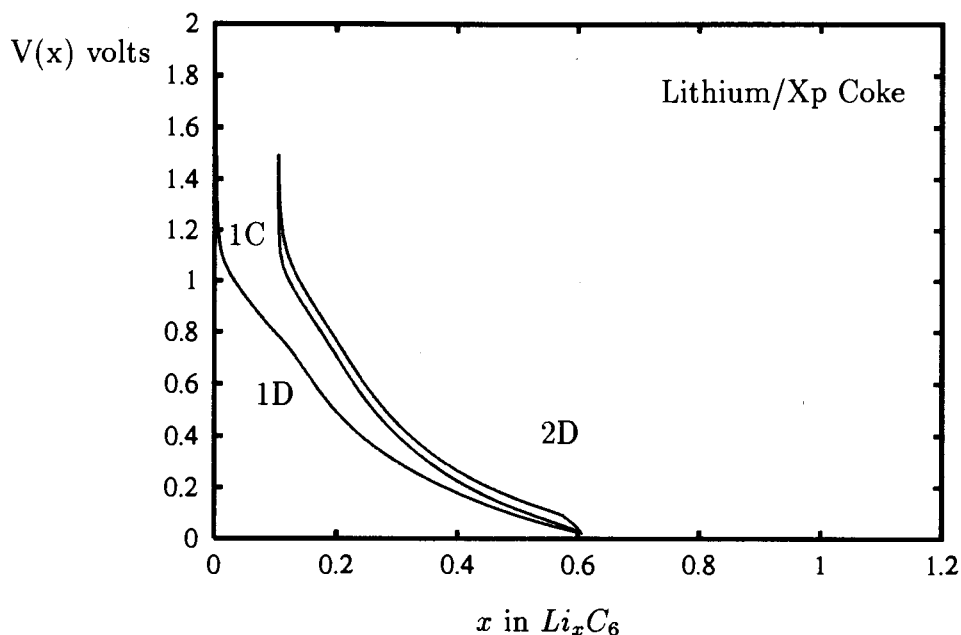


Figure 6.9: The first cycles of a Li/Xp coke cell at a 100 hour rate. The electrolyte used was 1M  $LiN(CF_3SO_2)_2$  dissolved in 50:50 PC and EC. Cell number is 910206.102.

Lithium intercalation in disordered carbons is quite different from that in graphite. Dahn et al. [14] studied Li intercalation in a series of disordered petroleum cokes. Their results show that the staging present in intercalated graphite is absent in intercalated petroleum coke. Recently, A. K. Sleight and U. von Sacken made a series of careful measurements on another highly disordered carbon, RVC (reticulated vitreous carbon), and found that the capacity for lithium intercalation in RVC does not depend on the choice of electrolyte [62].

Figure 6.9 and 6.10 show  $V(x)$  and  $-dx/dV$  for first  $1\frac{1}{2}$  cycles of a Li/xp coke (petroleum coke heated to about  $1300^\circ\text{C}$ ) cell. A solution of 1M  $LiN(CF_3SO_2)_2$  in a

50:50 volume mixture of EC and PC was used as the electrolyte. For disordered carbon, the electrolyte choice is not so critical as in graphite because of the higher voltage compared to graphite [62]. The passivation layer formation (irreversible plateaus) is partially suppressed [62] by more disordered structures. The cell was cycled at a 100 hour rate.

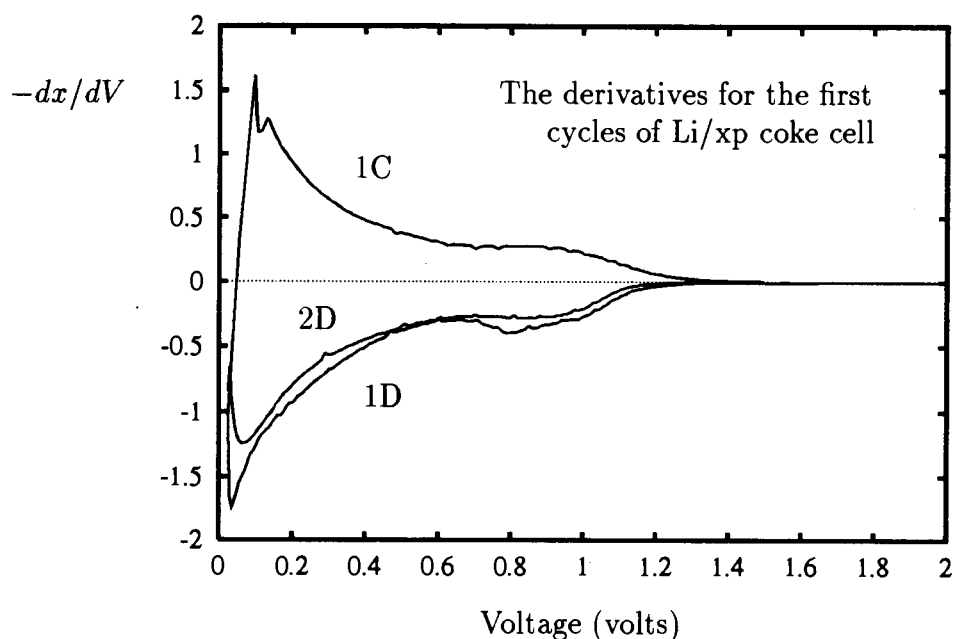


Figure 6.10: The derivative,  $-dx/dV$ , for the first cycles of a Li/xp coke cell at a 100 hour rate. The electrolyte used was 1M  $LiN(CF_3SO_2)_2$  dissolved in 50:50 PC and EC. Cell number is 910206.102.

The voltage curve for Li/coke cells  $V(x)$  is quite different from that in figure 6.4 for Li/graphite cells. First, the maximum reversible amount of Li that is able to intercalate into xp coke ( $x_{max} = 0.5$ ) is much lower than that in graphite ( $x_{max} = 1.0$  theoretically). Second, Li begins to reversibly intercalate in disordered carbons near 1.0 V, which is much higher than corresponding value for graphite (0.25V). Finally the Li/Coke cell shows no evidence of plateaus indicative of two phase coexistence.

Dahn et al [14] further showed that there is no evidence for the formation of staged phases in disordered carbons. What they found is:

1. the 002 peak shifts smoothly as  $x$  changes from  $x = 0$  to  $x = 0.5$  in  $Li_xC_6$ , which indicates a single phase (refer to figure 8 in Dahn's paper [14]);
2. The half-width of the 002 peak does not change significantly, which indicates that the crystalline disorder in coke is unaffected by Li intercalation (figures 8 and 9 in the same paper [14]).

They also discovered that the evidence of staged phases begins to be seen in carbon heated to 2200°C or more [14]. Physically, this can be understood by the turbostratic disorder existing between adjacent layers in disordered carbons:

As a consequence of this configurational disorder in petroleum coke, we expect the site energy to vary from site to site. Clearly if the site energy variation is large enough, Li atoms will reside in the sites of lowest energy while being spatially separated. Therefore *pinning* of Li due to disorder will suppress the formation of staged phases.

Although the voltage profiles vary a lot from one disordered carbon to another, the basic properties that we described here remain similar. In the next sections, we will examine more voltage profiles from different disordered carbons.

## 6.6 Electrochemical Studies On Soft Carbon

In the last two sections we reviewed the behavior of electrochemical cells using graphite or disordered carbons as the cathode and Li as the anode. Carbon has numerous disordered and graphitic forms, which basically can be classified into two groups, soft and hard carbon (see the discussion in chapter 2). In this and the next section, we are going to summarize the electrochemical properties of soft and hard carbon respectively and try to understand the general rules which govern the reversible capacity of the carbon.

Soft carbons are graphitizable carbons, which can be roughly subdivided into disordered soft carbons and graphitic carbons. The vague border between the two classes, from our structural models, is near 2200°C, which is where the staged phase begins to be seen [14]. In this section we focus on the cell behavior of soft carbons.

### 6.6.1 Disordered Soft Carbons

Figures 6.11 to 6.14 respectively show  $V(x)$  and  $\frac{I}{|I|}\sqrt{|dx/dV|}$  for the first discharge, first charge and second discharge of Li/soft-disordered-carbon cells. The selected voltage profiles shown here are for Petroleum Pitch heated to 550, 1200, 2000, and for Conoco coke heated to 2100°C. We plot  $\frac{I}{|I|}\sqrt{|dx/dV|}$  instead of  $-dx/dV$  in these figures only for better viewing of the derivative curves. Petroleum pitch heated to 550°C (figure 6.9) shows little reversible capacity at all, presumably because the material still contains substantial hydrogen and has little electronic conductivity.

Upon heating to 900°C (see figure 1.3 in chapter 1), a reversible capacity of  $x_{max} = 0.64$ , distributed between 0V and 1.3V, develops. The reversible capacity is  $x_{max} = 0.55$  for petroleum pitch heated at 1100°C (data not shown) and  $x_{max} = 0.62$  for petroleum pitch 1200°C (figure 6.11). For xp coke (about 1300C),  $x_{max}$  decreases a bit to 0.5 (figures 6.9 and 6.10 in section 6.5).

Table 6.1: The Reversible Capacity and HTT For Disordered Soft Carbons

Carbons	Petroleum Pitch 550	Petroleum Pitch 900	Petroleum Pitch 1100	Petroleum Pitch 1200	Petroleum Pitch 2000
HTT(°C)	550	900	1100	1200	2000
$x_{max}$	0.08	0.65	0.55	0.62	0.43
Carbons	Xp Coke	Conoco 2100	Conoco 2200	G2100	
HTT(°C)	1300	2100	2200	2100	
$x_{max}$	0.50	0.41	0.45	0.448*	

\* Measured by A.K. Sleight at Moli, the HTT for these carbons are unknown.

When pitch is heated to 2000°C,  $V(x)$  flattens compared to the 1200°C material, and the electrolyte decomposition apparently begins at about 0.8 V (see the peaks

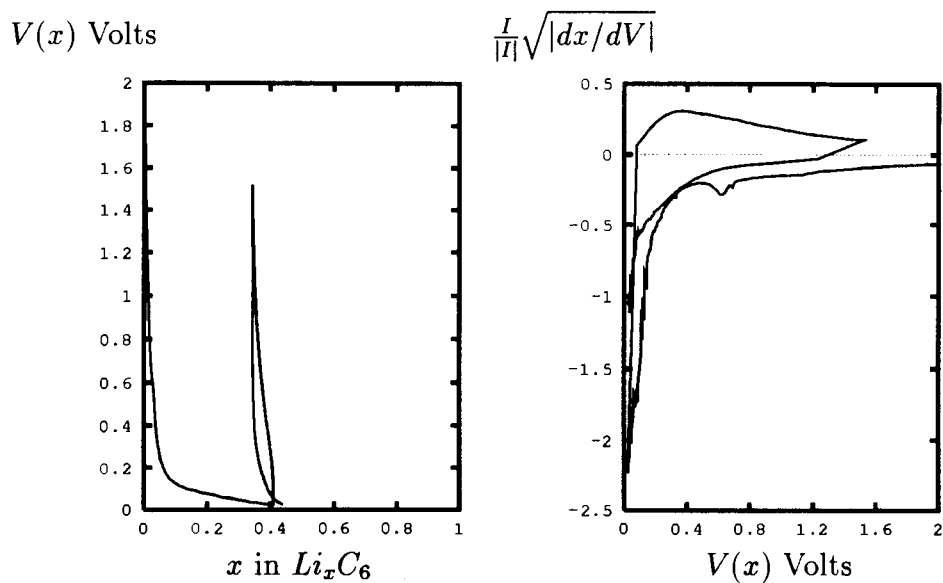


Figure 6.11: The Voltage Curve of Petroleum Pitch heated to 550°C

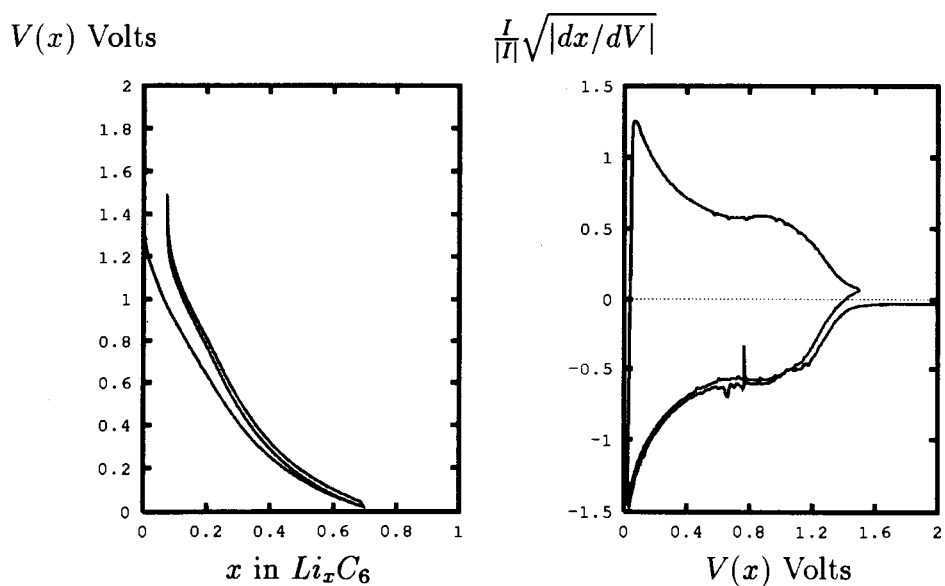


Figure 6.12: The Voltage Curve of Petroleum Pitch heated to 1200°C

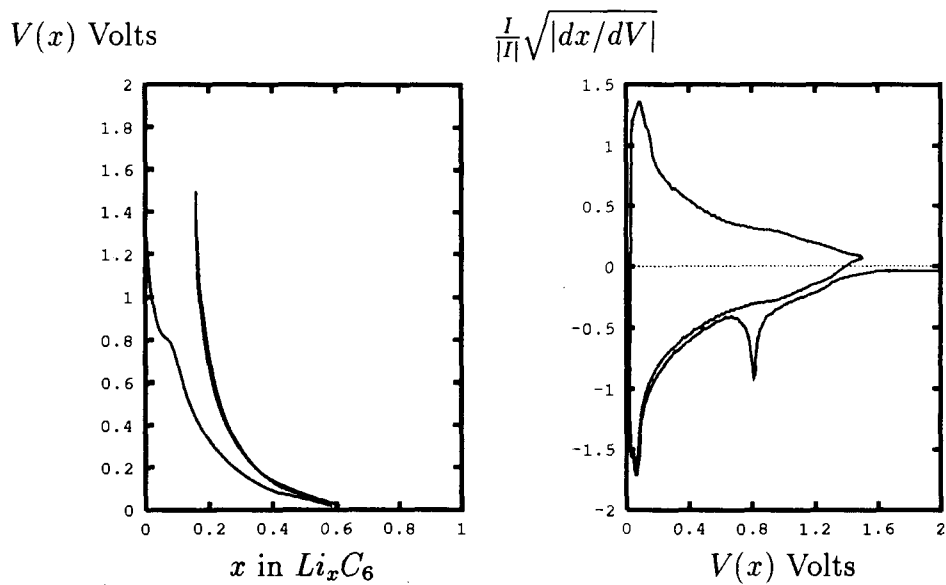


Figure 6.13: The Voltage Curve of Petroleum Pitch heated to 2000°C

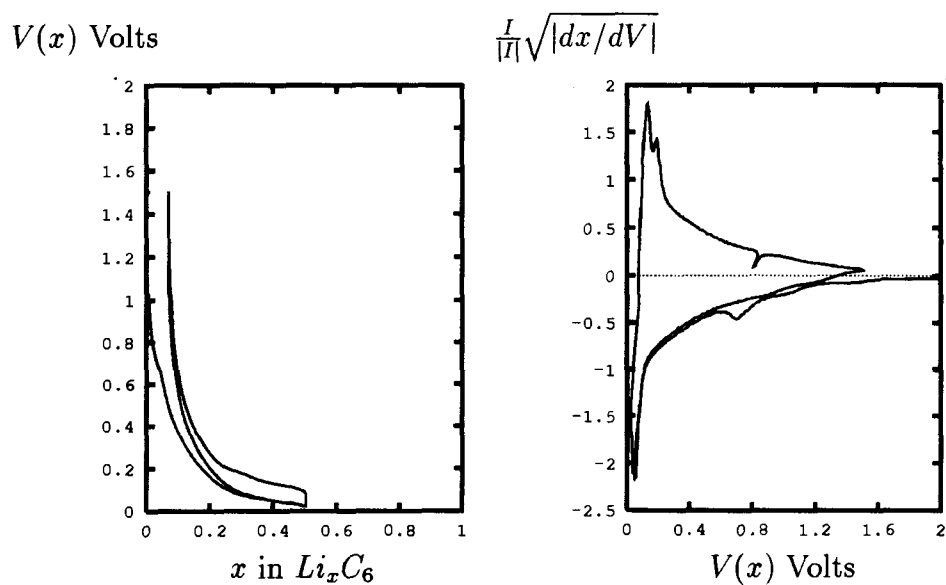


Figure 6.14: The Voltage Curve of Conoco Coke heated to 2100°C

at 0.8V in derivative figure 6.13). Heating pitch to 2000°C results in considerable capacity loss ( $x_{max} = 0.43$ ) and a dramatic shift of cell capacity to lower voltage as indicated by the appearance of peaks in  $\frac{I}{|I|}\sqrt{|dx/dV|}$  near 0.07 volts (figure 6.13). Conoco petroleum coke heated to 2100°C shows a similar capacity ( $x_{max} = 0.41$ ), and even sharper peaks in  $\frac{I}{|I|}\sqrt{|dx/dV|}$  including a doublet during the charge (figure 6.14).

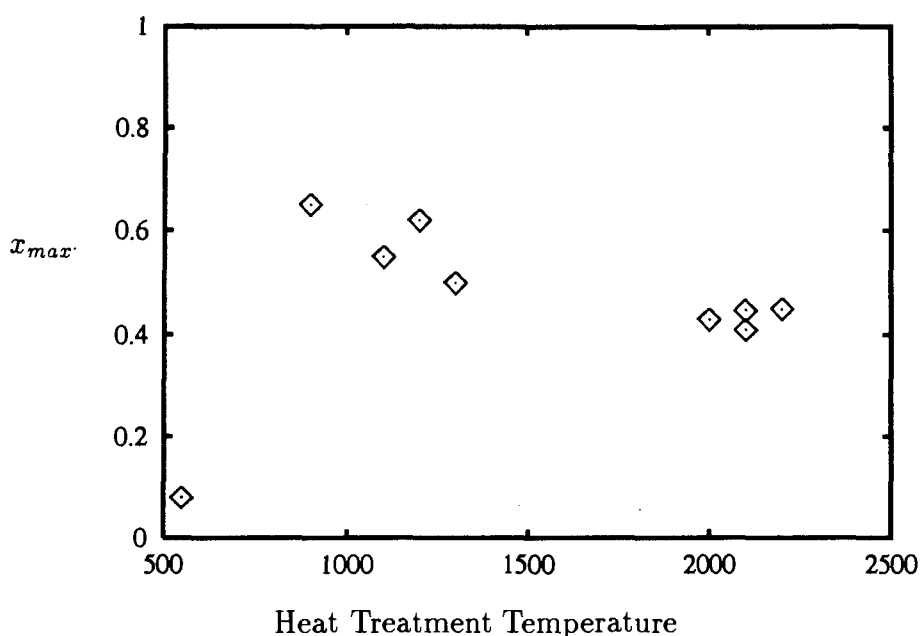


Figure 6.15: Showing the relation between maximum reversible capacities of disordered soft carbon and their heat treatment temperature

The data for  $x_{max}$  and HTT for disordered soft carbons are summarized in table 6.1. The major errors in  $x_{max}$  arise from the following two measurements: the active weight and the utilization of the carbon cathode materials. The weight was measured to  $10^{-3}$  g, which introduces an error of up to 5%. The utilization of the cathode is another source of error, but should not be too big if one assembles the cell carefully, to make sure all parts of the cathode are opposite the corresponding Li anode. The

overall errors involved in  $x_{max}$  should therefore be less than about 8%.

Neglecting the 550°C carbon which is not even carbonized,  $x_{max}$  basically decreases for these disordered carbon as the HTT increases (see figure 6.15). Upon further heating, the capacity begins to increase as we see next.

## 6.6.2 Graphitic Carbons

The capacity increases with further heating above 2200°C when turbostratic disorder begins to be substantially relieved and carbon starts to turn graphitic (also when the two layer model begins to be effective). We have seen examples of a voltage profile of a graphitic carbon in figures 1.3 and 6.4. In this section we will show more examples for different graphitic carbons.

Figures 6.16 to 6.20, selectively show a series of voltage and derivative profiles for the graphitic carbons described in section 5.6, except for the voltage profile shown in figure 6.16, which is Conoco coke heated to 2300°C. It is plotted here for comparison.

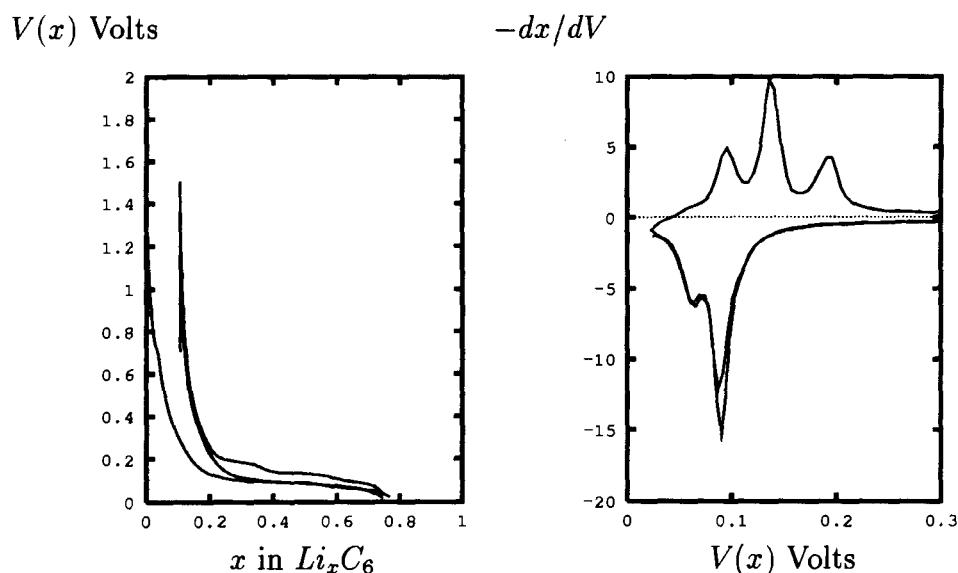


Figure 6.16: The Voltage Curve of Conoco Coke heated to 2300°C



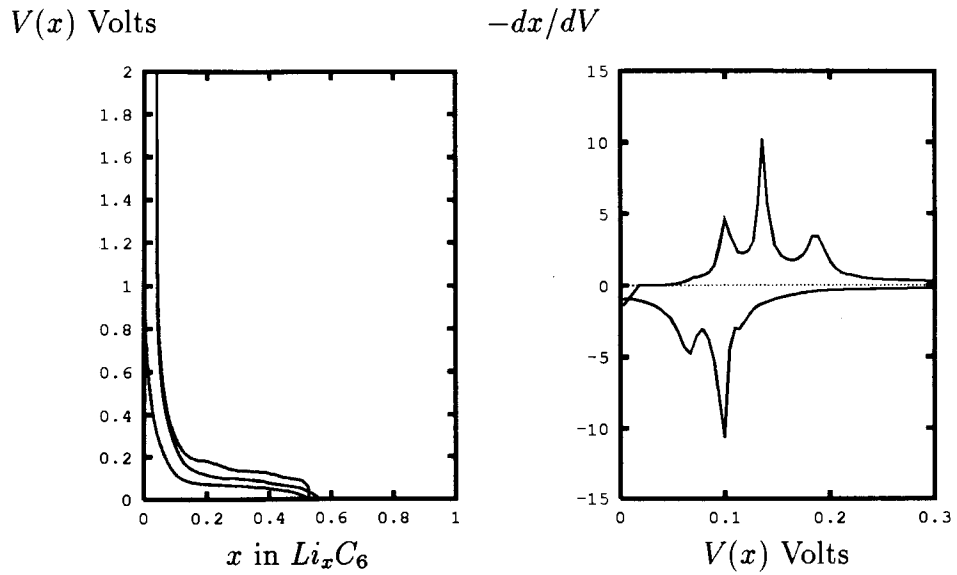


Figure 6.17: The Voltage Curve of a mesocarbon heated to 2300°C

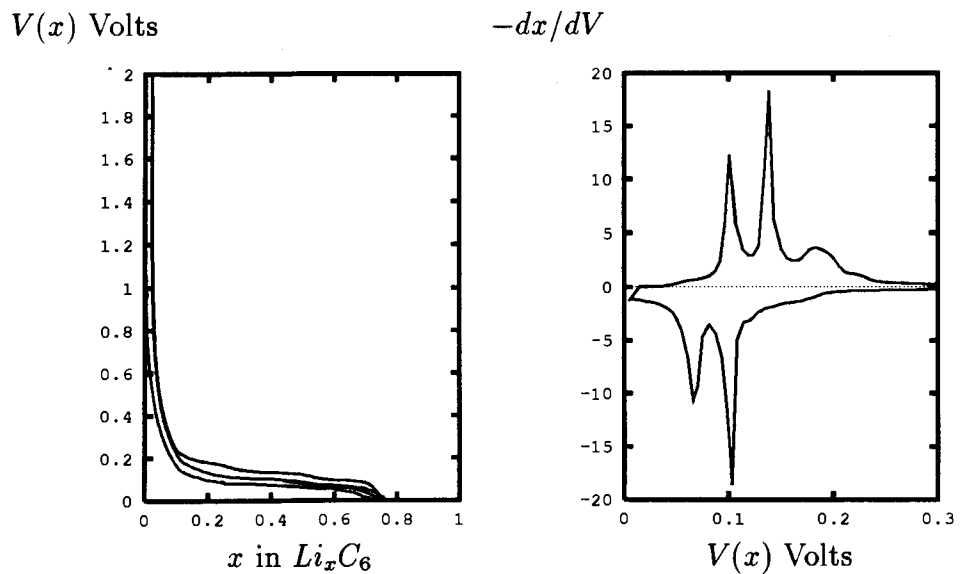


Figure 6.18: The Voltage Curve of a mesocarbon heated to 2400°C

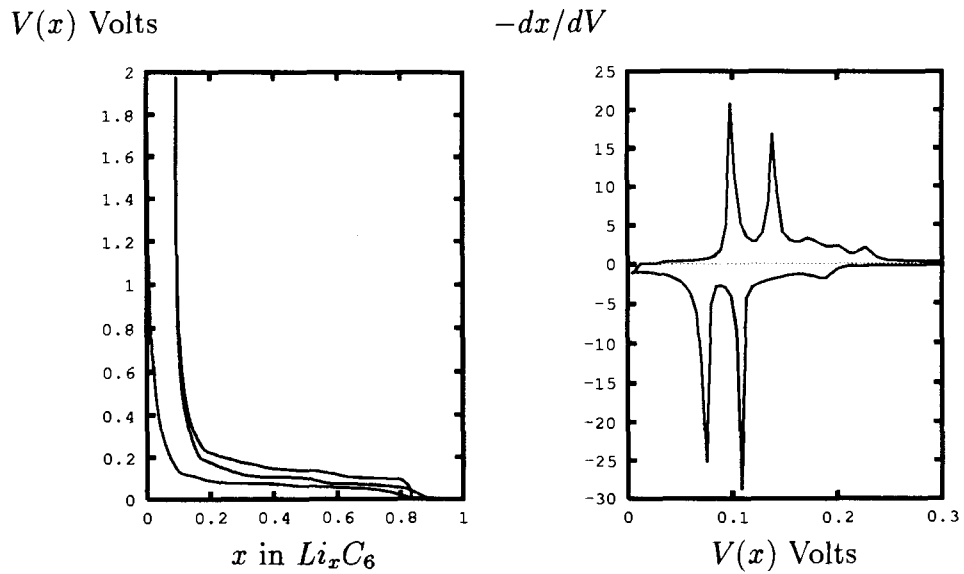


Figure 6.19: The Voltage Curve of a mesocarbon heated to 2600°C

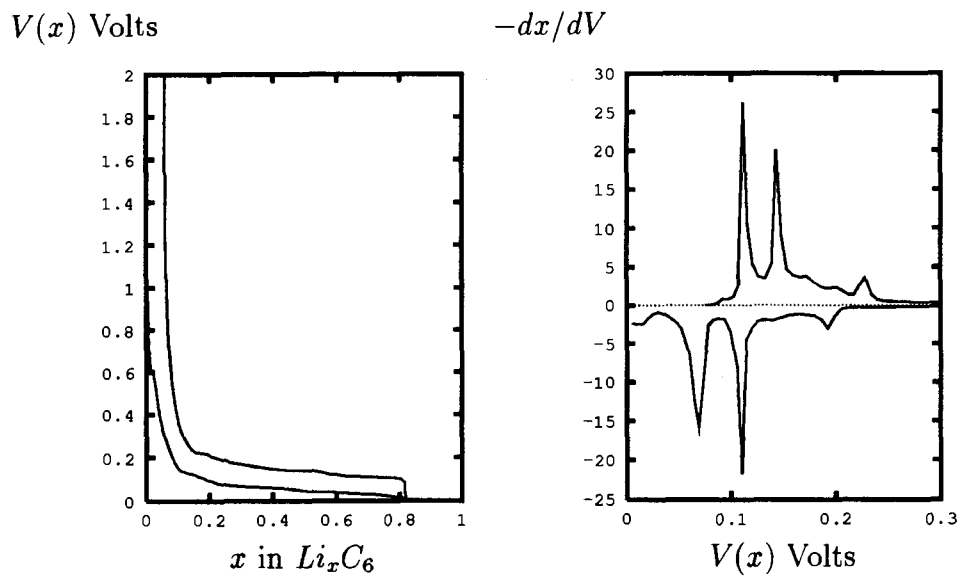


Figure 6.20: The Voltage Curve of a mesocarbon heated to 2800°C

For these soft carbons heated above 2300°C, the peaks in  $-dx/dV$ , indicative of the transitions between the staged phases in  $Li_xC_6$  [14, 71], are clearly observed. All these carbons heated above 2200°C have the majority of their capacity below 0.25 volts. Table 6.2 summarizes the relation between the maximum reversible capacities,  $x_{max}$ , and corresponding HTT. Most of these  $x_{max}$  data were measured by A.K. Sleigh at Moli. Carbons heated at less than 2200°C still have a high percentage of turbostratic disorder and need the one layer model for fitting. Carbons heated at 2000, 2100°C are not graphitic,<sup>1</sup> which can also be seen by the decreasing values of  $x_{max}$  up to 2100°C. Soft carbons heated above 2200°C are basically graphitic carbons.

Table 6.2: The Maximum Reversible Capacity and HTT For Soft Carbons

Carbons	Petroleum Pitch 2850	Conoco 2200 <sup>+</sup>	Conoco 2300	Lonza KS44	G2300
HTT(°C)	2850	2200	2300	3000	2300
$x_{max}$	0.740	0.450	0.640	0.860	0.657*
Carbons	G2400	G2500	G2600	G2700	G2800
HTT(°C)	2400	2500	2600	2700	2800
$x_{max}$	0.722*	0.716*	0.759*	0.786*	0.803*

\* Measured by A.K. Sleigh at Moli, The data were originally received in mAh/g, then divided by 370 mAh/g to change to  $x_{max}$ .

+Actually this carbon does not belong to graphitic carbon.

Figure 6.21 shows  $x_{max}$  as a function of HTT for all disordered and graphitic soft carbons. A minimum at about HTT 2100°C can easily be seen. The carbon structure around this temperature begins to transform from disordered to graphitic. Why is  $x_{max}$  a minimum around 2200°C? We will return to this shortly.

By the way, there is a large body of experimental results for a variety of soft carbons given in reference [78]. The electrolyte used in those studies was 1M  $LiClO_4/PC$ , which is known to cointercalate within and decompose readily on the surface of

<sup>1</sup>One can use the amount of random stacking probability of a carbon to define whether it belongs to the disordered ( $P > 0.5$ ) or graphitic ( $P < 0.5$ ) carbon.

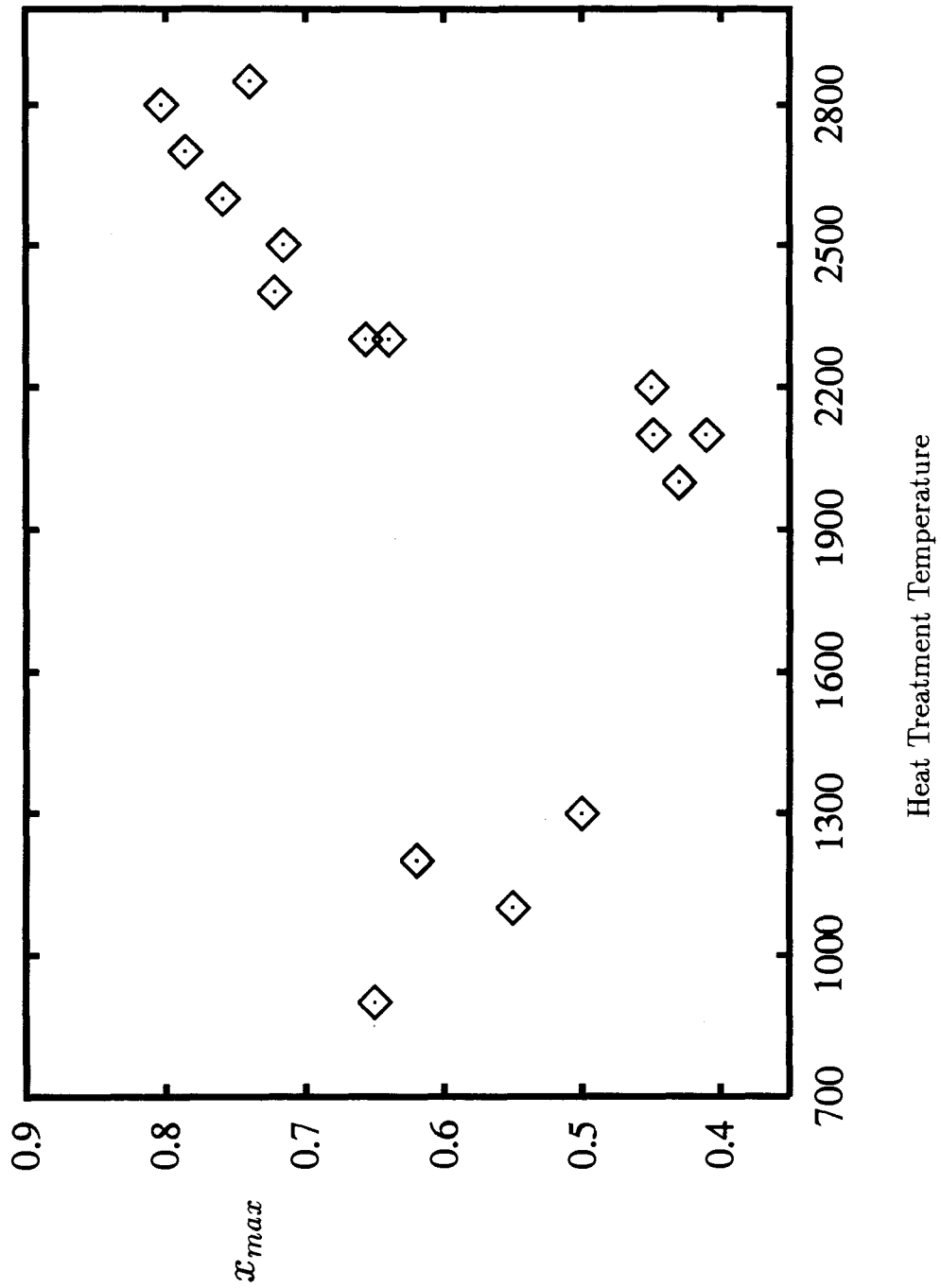


Figure 6.21: Showing the relation between maximum reversible capacity and heat treatment temperature for all the soft carbons

graphitic carbons, so data for carbons heated above 2000°C reported in [78] is unreliable. For low temperature carbons, these results show higher capacities than ours at the same heating temperature, but were measured in a  $LiCoO_2/Carbon$  cell, not against Li metal, so it is possible that the carbon electrode has been taken below zero volts versus Li (under load) which has been shown [79] to give some excess capacity before Li plating begins. More important than the actual capacity values is the trend observed upon heating, which is analogous to our data.

## 6.7 Electrochemical Studies On Hard Carbon

Hard carbons consist of small regions of organized carbon which are crosslinked chemically to other small regions. The cross-linking normally can not be broken even by heating to 3000°C, so these carbons do not graphitize. In addition, the cross-links may involve other atoms, like nitrogen or phosphorus, depending on how the hard carbon is made. Our studies on hard carbons show that simple trends with HTT (like those that exist for soft carbons) are difficult to identify. Furthermore, the voltage profiles of some hard carbon show substantial hysteresis, which was never observed for the soft carbons.

First, we have studied the electrochemical behavior of the commercially available hard carbon series described in section 5.4. Figure 6.22 to 6.24 show  $V(x)$  and  $-dx/dV$  for Hard Carbons 1200,2000 and 2850 respectively. These carbons were made by a Japanese company, and the detailed manufacturing process is unknown to us. The cycling behaviors are similar, which indicates that the structure is not changed much by heating this hard carbon to high temperature, in agreement with our earlier findings in chapter 5.

Next, we studied the hard carbons prepared from Furfuryl Alcohol (FA), described in section 5.5. Zhong et al [56] made Li/FA carbon cells and tested them. During the first discharge of FA600 (see figure 6.25), Li reacts with the carbon corresponding to  $x = 2.8$ , but much of this is irreversible capacity. Only 57% of the Li can be removed from FA600 in the following cycles (the data has been shown in [56]). There is a large hysteresis in the cycling of FA 600. The voltage difference between the charge and

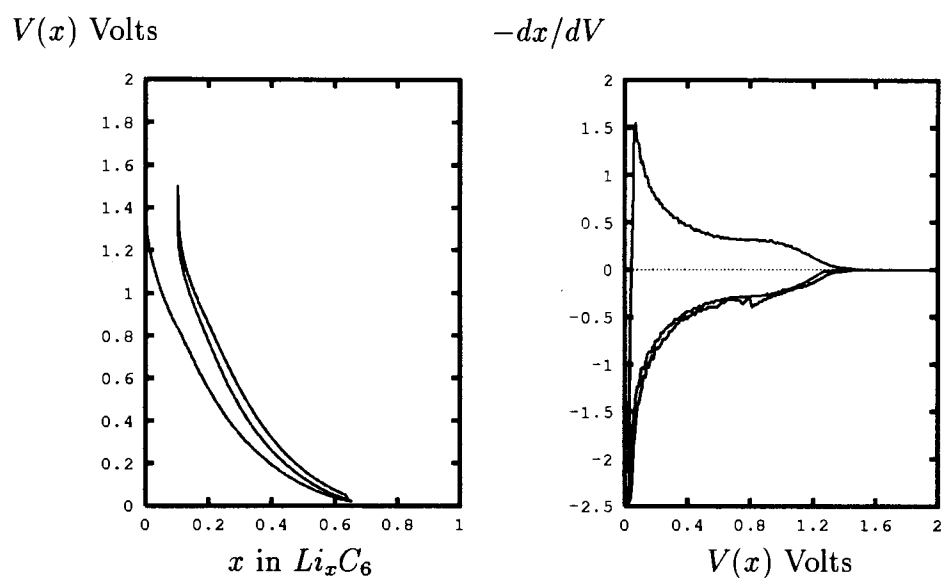


Figure 6.22: The Voltage Curve of hard carbon heated to 1200°C

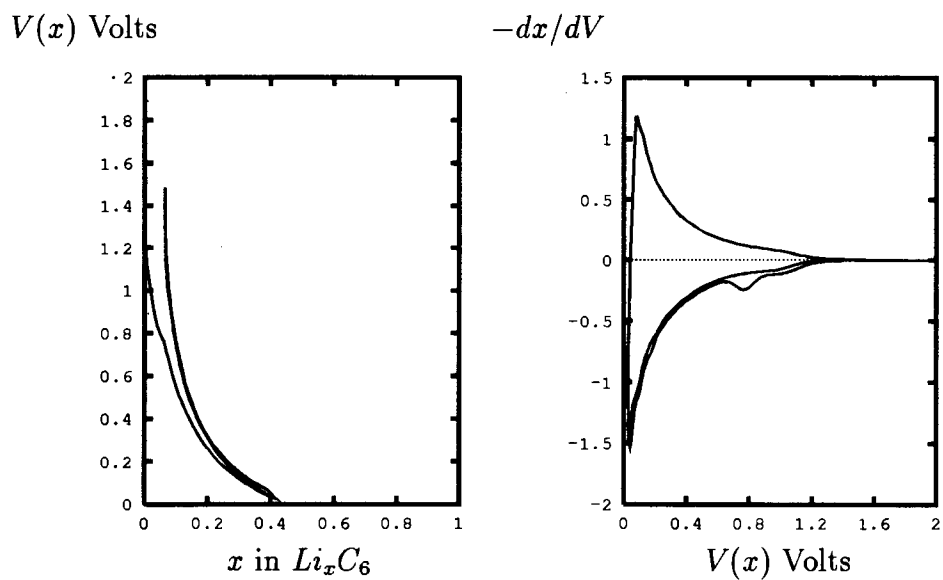


Figure 6.23: The Voltage Curve of hard carbon heated to 2000°C

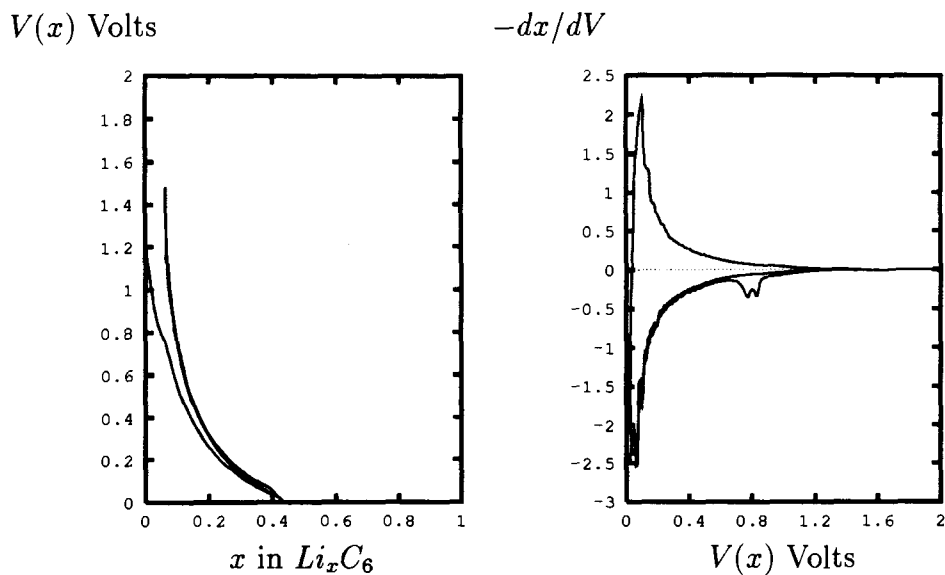


Figure 6.24: The Voltage Curve of hard carbon heated to 2850°C

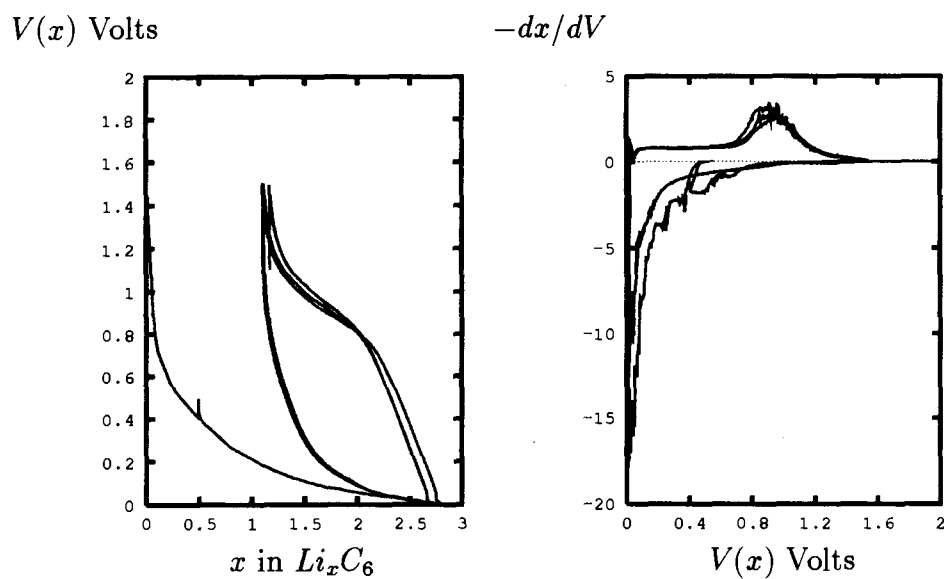


Figure 6.25: The Voltage Curve of FA 600 as a function of  $x$

discharge is as big as 1.0V. After heating to higher temperature, FA carbons show less and less irreversible capacity and hysteresis. Figure 6.26 shows the voltage profile of FA1100. It is our belief that the large irreversible capacity in FA carbons is due to highly disordered structure and phosphorus impurities in the material. The PFA polymer contains mainly pentagonal carbon rings and OH groups. After heating to 600C for several hours, some pentagonal rings still exist in the structure. Zhong et al also did TGA measurements on FA 600 and found that there was a 5-7% weight loss when the FA600 carbon was reheated to 1100C for 2 hours. Extremely disordered structures can account for a large amount of Li trapped in the carbons [62].

The X-ray powder profiles for hard carbon 1200 and FA1100 (see figures 5.13 and 5.18 in chapter 5) are similar, as evidenced by the fitting parameters. However, the voltage profile for Hard Carbon 1200 is similar to that of Petroleum Pitch 1200, but differs greatly from FA1100 even though the X-ray pattern of Hard Carbon 1200 more closely resembles that of FA1100 than the heated pitch. This suggests that factors other than structural ones are involved in determining  $V(x)$  for this case. Work by the Sony group [77] shows that these FA carbons have several percent of incorporated phosphorus in these structures. This could be responsible for the difference.

Table 6.3: The Maximum Reversible Capacity and HTT For Hard Carbons

Carbons	FA 600	FA 900	FA 1100	Hard Carbon 1200	Hard Carbon 2000	Hard Carbon 2850
HTT°C	600	900	1100	1200	2000	2850
$x_{max}$	1.6*	1.0*	0.80*	0.545	0.352	0.380

\* Believed that these carbons contain large percentage of impurities.

HTT and maximum reversible capacity data for the hard carbon and FA series carbons are summarized in table 6.3. It is difficult to make any detailed statements based on the data listed in table 6.3. In what follows, we will only focus on understanding the behavior of soft carbons. The behavior of hard carbon apparently depends on the processing of the carbon and the impurities it contains.



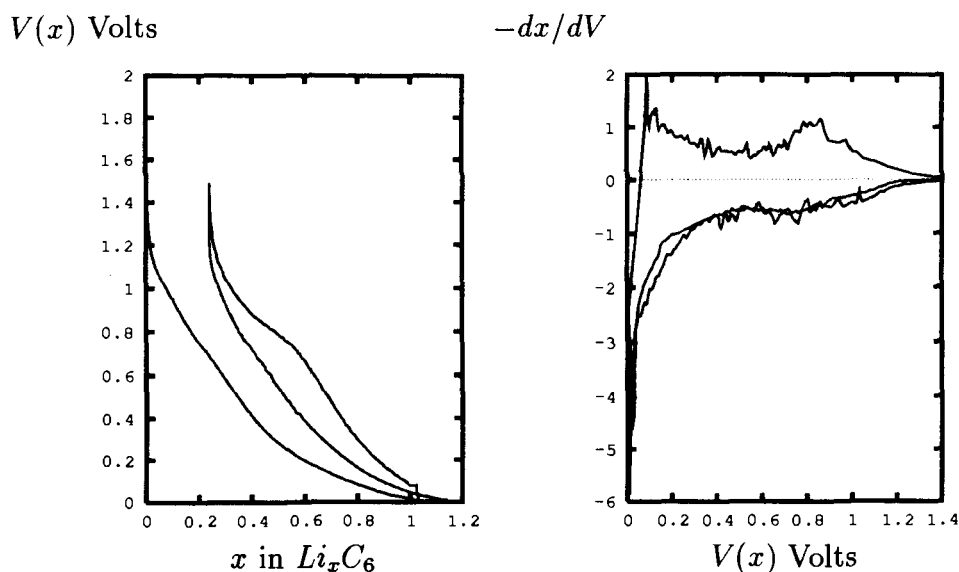


Figure 6.26: The Voltage Curve of FA 1100 as a function of  $x$

## 6.8 Structural Disorder and Capacities For Soft Carbons

As we have seen on the electrochemical study in the previous sections, cell capacities are dependent on the carbon heat treatment temperature and structure. How does one understand the dependence of cell capacity on the carbon structural disorder? In other words, can we correlate cell capacities to structural information, i.e.,  $P$ ,  $P_t$  and  $g$  attained from fitting of carbon X-ray profiles? This is the concern of this section.

### 6.8.1 Probabilities and Disordered carbon

Let us recall our picture about disordered carbon first. Our model of disordered carbon describes it as a stack of registered, random and buckled layers where the percentage of different layers is mainly determined by HTT. Figure 6.27 summarizes the probabilities of the four different layer stacking schemes; random stacking probability  $P$ , 3R-type stacking fault probability  $P_t$ , 2H-type graphite stacking probability

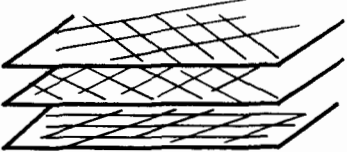
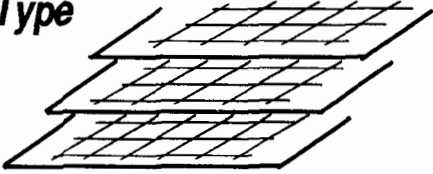
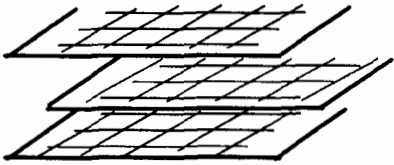
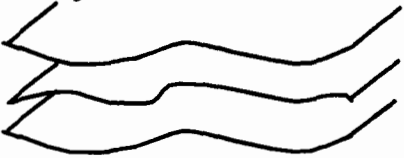
<b>Probs</b>	<b>Layer Stacking</b>
$P$	<b>Random</b> 
$P_t$	<b>3R-Type</b> 
$1-P-P_t$	<b>2H-Type</b> 
$1-g$	<b>Buckled Layers</b> 

Figure 6.27: A summary of probabilities used in our carbon model

$1 - P - P_t^2$  and finally the probability,  $1 - g$ , to include buckled layer fractions in highly disordered carbons. All probabilities can be determined by X-ray fitting as described in the previous chapters. In this section,  $P$  and  $P_t$  always implies the normalized value. For the one layer model, the normalized value is equal to the definition in our model and for the two layer model, the normalized value is half of the value defined in our model (see chapter 2).

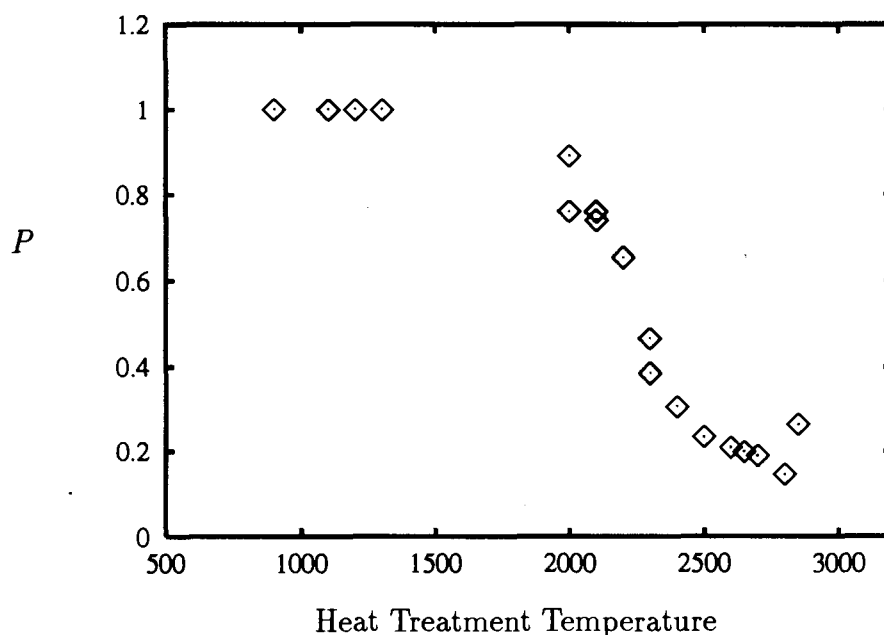


Figure 6.28: Random stacking probability versus the heat treatment temperature for soft carbons

To show the dependence of these probabilities on HTT, we plot  $P$ ,  $P_t$ ,  $1 - P - P_t$  and  $g$  versus HTT in figure 6.28 and 6.29, respectively. Clearly when HTT is below about  $1500^\circ\text{C}$ , there is turbostratic disorder between all adjacent layers ( $P = 1$ , see figure 6.29), and then as the HTT increases, the random stacking probability

<sup>2</sup>For the disordered carbons, this probability is not rigorous 2H-type stacking (see description in chapter 2 about one layer model), but we treat it as 2H-type probabilities for the sake of consistency.

smoothly decreases.<sup>3</sup> The low HTT carbons (less than 1500C) have a large amount of unorganized carbon ( $1 - g$  is around 0.5, see figure 6.29). As HTT increases from

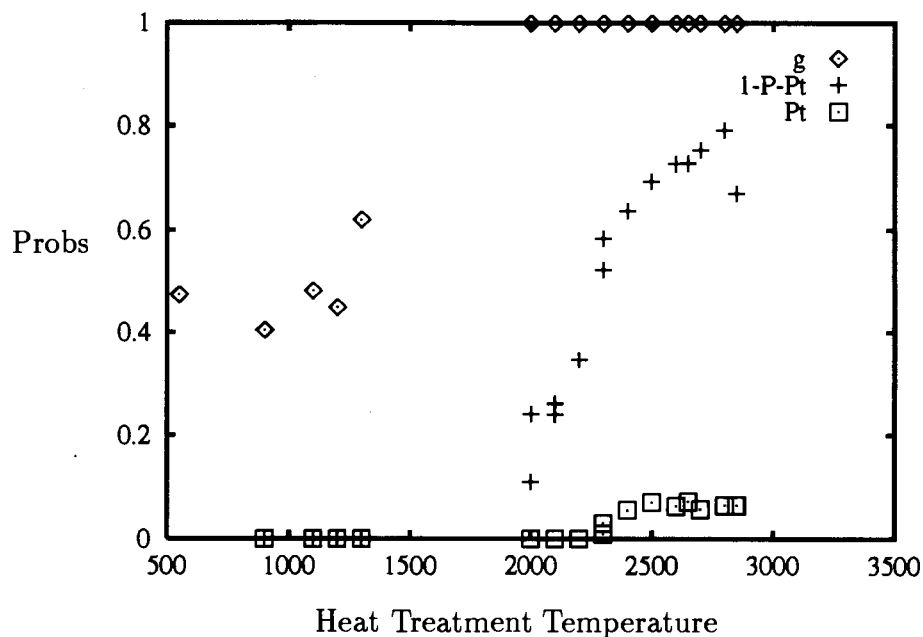


Figure 6.29: 2H-type stacking probability  $1 - P - P_t$ , 3R-type stacking fault probability  $P_t$  and probability for buckled layers versus the heat treatment temperature (HTT) for soft carbons

550C,  $g$  basically increases, which implies that the percentage of organized carbon increases and the layers become less distorted. When HTT increases over some critical temperature (about 2200C), there is a significant transition. The stacking of carbon layers becomes more ordered and it becomes necessary to use the two layer model to fit the X-ray data. The appearance of  $P_t$  is a signal that carbon has a more registered stacking. As a comparison, the reversible capacity as a function of HTT behaves quite differently. Initially, when the heating temperature is only around 550°C,  $x_{max}$  is small because the material contains substantial hydrogen and is a poor conductor.

<sup>3</sup>The carbon supposedly heated The data of 2850°C may have actually been heated to a lower temperature. Otherwise it may be form a source more difficult to graphitize.

$x_{max}$  increases for temperatures near  $1000^{\circ}\text{C}$ , as the hydrogen is lost and reasonable electrical conductivity is attained [81].

Around  $1000^{\circ}\text{C}$ , the fraction of unorganized carbon in the material is relatively large as indicated by the value of  $1 - g$  required to fit the X-ray data (see summary in table 6.4 for reference). The cell capacity is spread over a range of approximately 1.2 volts. For heating temperatures above  $1300$  to  $1500^{\circ}\text{C}$ , the cell capacity decreases to a minimum, near  $2100^{\circ}\text{C}$ , just as the fraction of unorganized carbon is reduced to zero. Simultaneously, the voltage profile flattens and the majority of the cell capacity appears to be near 0.1 or 0.2 V. Upon further heating,  $x_{max}$  increases with registered stacking until finally  $x_{max}$  approaches 1 for perfect graphite, as shown in figure 6.29. This qualitative consideration leads us to a phenomenological model described in the next section, which can correlate the capacity,  $x_{max}$ , to the carbon structure and explain the  $x_{max}$  behavior.

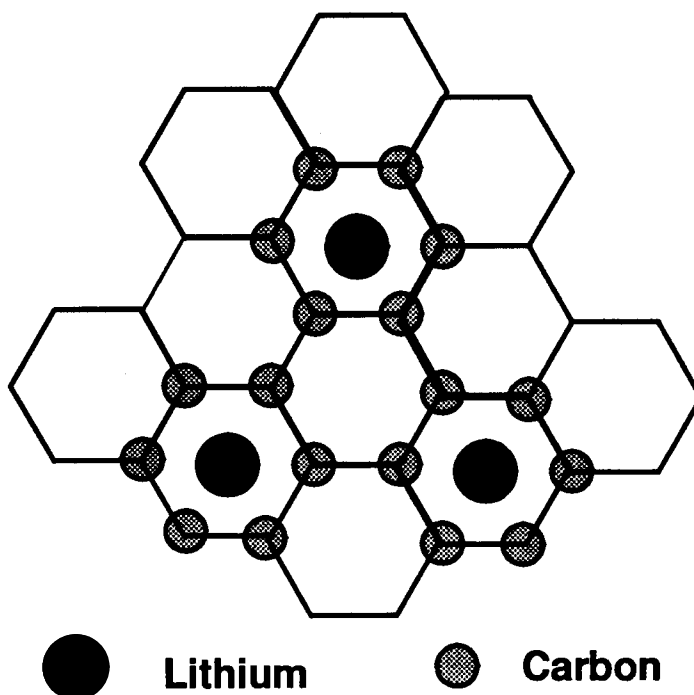


Figure 6.30: Six Carbon atoms share one Lithium in the graphite case

### 6.8.2 A Phenomenological Picture

We can qualitatively understand the temperature dependence of  $x_{max}$  with a simple speculative model, based on the following rational assumptions:

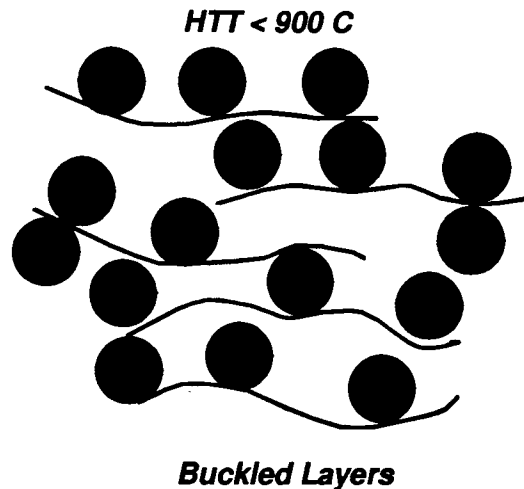


Figure 6.31: Showing that highly distorted layers may accommodate more lithium atoms than randomly stacked flat layers

1. for perfect graphite ( all 2H-type layer stacking), 6 carbon atoms are able to accommodate 1 lithium atom, that is,  $LiC_6$  (stage 1) as shown in figure 6.30. This is a well-known fact. 3R-type graphite should have the same ability to accommodate lithium since the layers are stacked in similar registered positions. We assume that for lithium intercalation, 2H and 3R type stacking can accommodate the same amount of lithium, i.e., one lithium atom per six carbon atoms.
2. the unorganized carbon, isolated single layers or highly strained groups of layers, can reversibly intercalate a significant amount of lithium, say an amount  $x_{uc}$  per 6 carbon atoms. Some isolated single layers may accommodate lithium on both sides of layers (see figure 6.31). Since this material is highly distorted, it follows

that the geometry of the sites for intercalated Li will vary from site to site. This will lead to a distribution in site energies and a sloping voltage profile [71].

- for unstrained pairs of carbon layers, random shifts or rotations between them inhibit the intercalation of lithium. We assume an amount of  $x_r$  per 6 atoms for turbostratically stacked parallel layers (see figure 3.32). This assumption is reasonable, considering the recent work of Boehm and Banerjee [82] who show theoretically that intercalated Li strongly prefers adjacent carbon layers with  $AAAAA \cdots$  stacking, as found in crystalline  $Li_1C_6$  [83]. Carbon layers with turbostratic disorder will most likely be *pinned* and hence unable to shift into the  $AAAAA \cdots$  stacking arrangement, resulting in lower capacity for intercalated Li. (The presence of unorganized carbon leads to lower carbon density and to regions where there is more *space* available for the Li to fit.) Layer spacing may play an important role for lithium intercalating into such randomly stacked layers. Small  $d_{002}$  may totally prevent lithium intercalation in turbostratically stacked adjacent layers and so generally,  $x_r$  may be a function of  $d_{002}$ .

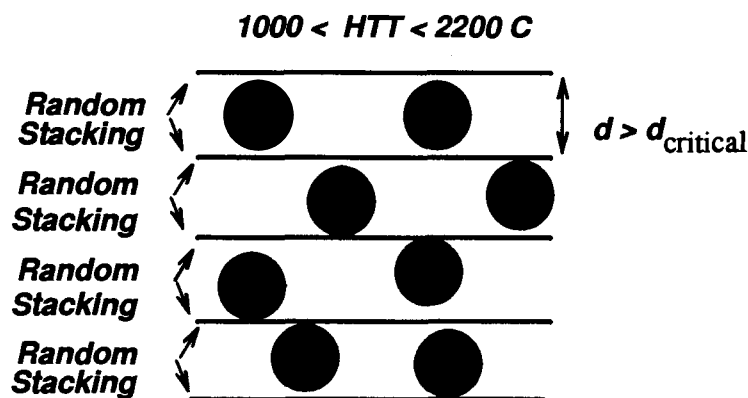


Figure 6.32: Showing that randomly stacked layers may accommodate less lithium atoms than highly distorted layers

Based on these considerations, we can write down the following equations to calculate the capacity of these structures.

$$x_{max} = g \times x_{organized} + (1 - g) \times x_{uc} \quad (6.2)$$

$$x_{organized} = (1 - P) \times 1 + (P) \times x_r$$

where we divide  $x_{max}$  into two parts of contributions: the organized carbon layer and the unorganized carbon layer.

### 6.8.3 Graphitic Carbons

To find  $x_r(d_{002})$  and  $x_{uc}$ , look at graphitic carbons first. For graphitic carbons, equation (6.2) becomes simpler since  $g = 1$  for all graphitic carbons, thus,

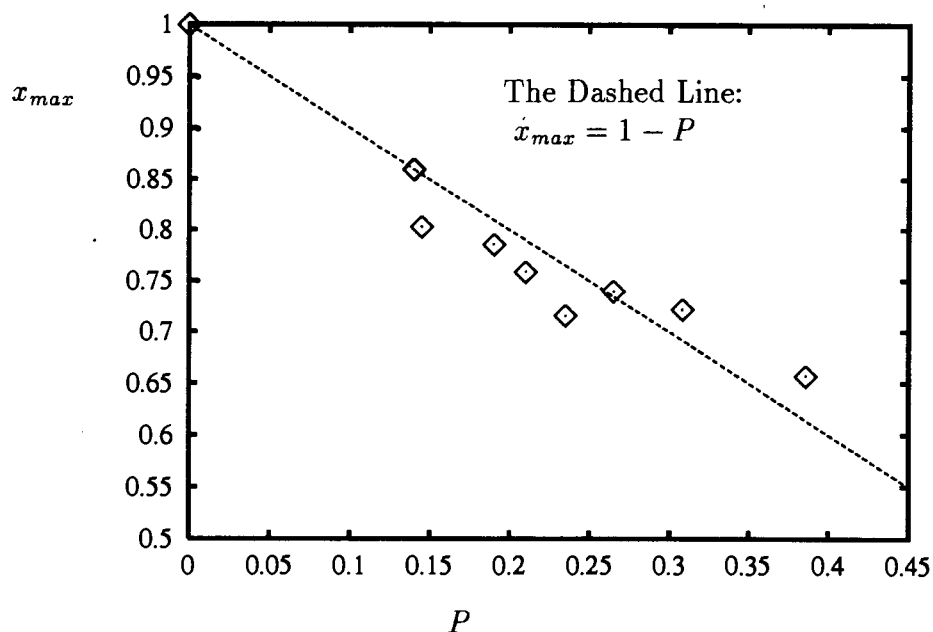


Figure 6.33: Capacities versus  $P$  for graphitic carbons

$$x_{max} = 1 - P \times (1 - x_r) \quad (6.3)$$



This equation allows us to extract  $x_r$  for graphitic carbons if reasonable  $x_{max}$  and  $P$  data are available. Figure 6.33 plots the capacities of graphitic carbons listed in table 6.2 versus  $P$ . The capacities of these graphitic carbons were measured by A. K. Sleight at Moli. Figure 6.33 shows that the data are acceptably falling around the line:  $x_{max} = 1 - P$ . Comparing this with equation 6.3, we can draw following conclusion: for graphitic carbon, the randomly stacked layers can not host lithium ( $x_r = 0$ ), which may be caused by small  $d_{002}$ .

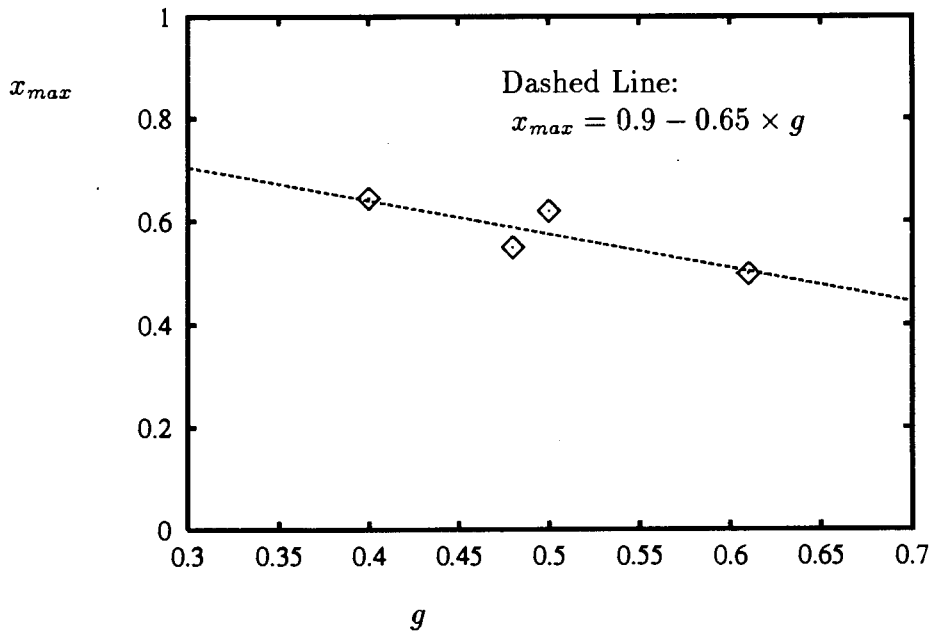


Figure 6.34: Capacities versus  $g$  for highly disordered carbon

#### 6.8.4 Disordered Soft Carbons

Now we are going to look at  $x_{uc}$  and  $x_r$  for disordered soft carbons. For highly disordered carbons,  $P = 1$  and thus equation (6.2) becomes

$$x_{max} = x_{uc} - g \times (x_{uc} - x_r) \quad (6.4)$$

This equation is similar to equation (6.3) replacing  $P$  with  $g$  and 1 with  $x_{uc}$ . Theoretically, we can extract the parameters,  $x_{uc}$  and  $x_r$ , from the plot of  $x_{max}$  versus  $g$ .

Figure 6.34 plots  $x_{max}$  versus  $g$  for four different highly disordered carbonaceous materials: Petroleum Pitch heated at 900, 1100 and 1200, and Xp coke heated at about 1300C, (The data are listed in table 6.1). The solid line is the linear fit:  $x_{max} = x_{uc} - g \times (x_{uc} - x_r)$  with  $x_r = 0.25$  and  $x_{uc} = 0.90$ . The error in these data caused in part by inconsistencies between the different disordered carbons (ie. different starting raw material). While this data is not sufficient to allow an accurate estimate of  $x_{uc}$  and  $x_r$ , it gives a consistent result from the fitting of  $x_{max}$ -HTT curve by adjusting these parameters (we will discuss this in next section).

To conclude this section, we summarize the  $x_r$  values:

$$x_r = \begin{cases} 0.25 & \text{disordered}(HTT < 2200C) \\ 0 & \text{graphitic}(HTT > 2200C) \end{cases} \quad (6.5)$$

This is only a rough equation which gives us a guide to understand the lithium intercalation behavior in disordered layer stackings. The structural and electrochemical data for disordered carbons and graphitic carbons are summarized in table 6.4 and 6.5 respectively.

### 6.8.5 Summary

The values of  $x_{uc}$  and  $x_r$  attained in last section are not very reliable, because of the shortage of data. Another way to estimate these important parameters is to fit the  $x_{max}$ -HTT curve shown in figure 6.21 by adjusting the parameters in equation (6.2). Figure 6.35 shows the fit of our model to the data in figure 6.21, with parameters  $x_{uc} = 0.90$  and  $x_r = 0.25$  obtained by fitting  $x_{max}$  vs.  $g$  curve in figure 6.34. The fit is reasonably acceptable considering the simplicity of the model. It is clear that more data between HTT=1000C and 2200C will be better to verify our theory.

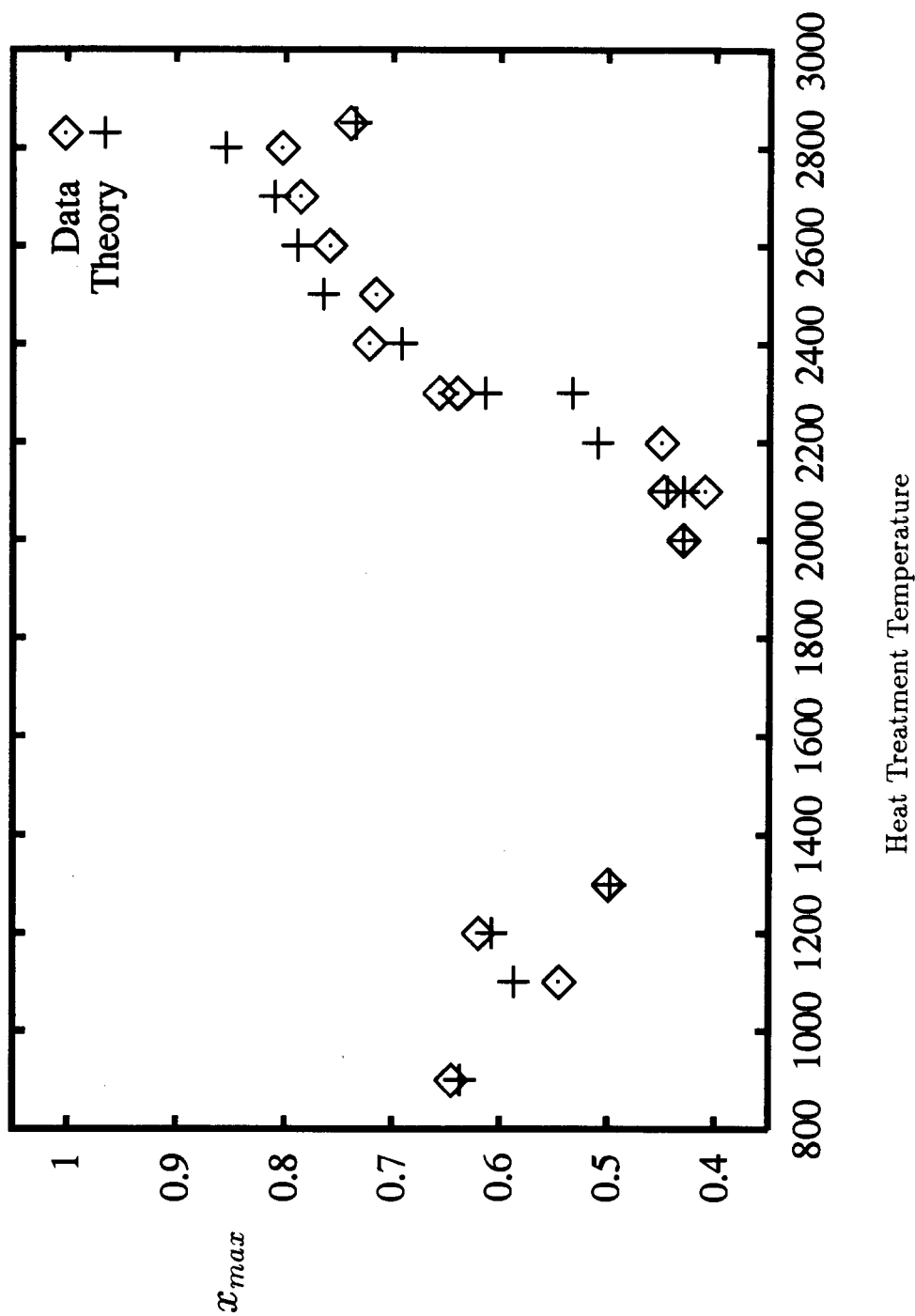


Figure 6.35: Capacities versus HTT for soft carbons: data and prediction

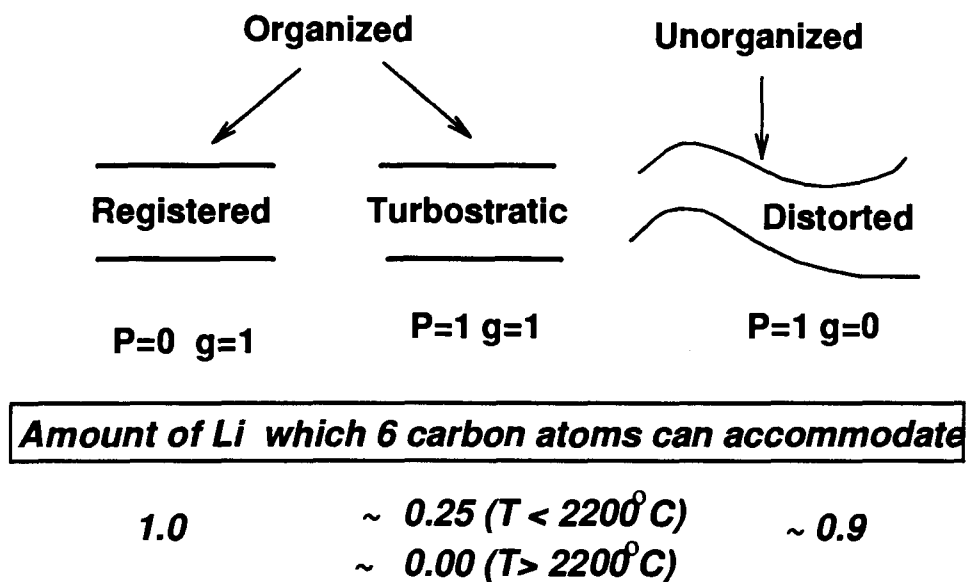


Figure 6.36: Showing our picture for lithium intercalation into carbons

To summarize our understanding of lithium intercalation into disordered carbons, we draw a schematic picture in figure 6.36. When the HTT is less than  $900^\circ\text{C}$ , the carbon layers are mostly buckled and completely, randomly stacked. According to our analysis, an isolated, buckled single layer can hold more lithium than a randomly stacked flat layer ( $x_r < x_{uc}$ ). As HTT increases to about  $2200^\circ\text{C}$ , the carbon layer becomes flat but still completely, randomly stacked ( $P = 1$  and  $g = 1$ ). This kind of carbon structure can accommodate less lithium because of the disordered stacking. Upon further increasing the HTT, the amount of disorder decreases, so that the capacity increases until  $x_{max}$  approaches 1, for natural graphite.

Table 6.4: Electrochemical and Structural Data for disordered carbons

Carbons	FA	Hard	Hard	Hard	Hard	Pitch	Pitch	Pitch	Pitch	Pitch	Pitch	G2100	Xp	Cono	Cono
	1100	1200	2000	2850	550	900	1100	1200	2000				Coke	2100	2200
HTT	1100	1200	2000	2850	550	900	1100	1200	2000	2100	2100	1300	1300	2100	2200
$x_{max}$	0.85	0.545	0.352	0.38	0.075	0.645	0.545	0.62	0.43	0.448	0.448	0.50	0.50	0.41	0.45
$\zeta$	0.027	0.013	0.01	0*	0.03	0.014	0.036		0*	0*	0*	0*	0*	0*	0*
$d_{002}$ Å	3.503	3.537	3.463	3.450	3.488	3.479	3.477	3.497	3.430	3.411	3.411	3.445	3.445	3.402	3.408
$a$ Å	2.441	2.444	2.449	2.450	2.460	2.450	2.441	2.441	2.459	2.460	2.460	2.462	2.462	2.457	2.461
$L_a$ Å	29	24	51	55	7.3	17		35	105	111	111			91	88
$M$	40*	40*	40*	40*	40*	40*	40*	40*	51	74	74	40*	40*	55	69
$\delta$ Å	1.06	1.00	0.91	1.30	2.0	1.02	0.82	0.70	0.108	0.08	0.08	0.06	0.06	0.07	0.07
$g$	0.20	0.26	0.55	0.80	0.475	0.40	0.45	0.45	1*	1*	1*	0.62	0.62	1*	1*
$P$	1*	1*	1*	1*	1*	1*	1*	1*	0.89	0.76	0.76	1*	1*	0.74	0.73

\* Fixed during the fitting.

Table 6.5: Electrochemical and Structural Data for graphitic carbons

Carbons	Cono 2300	G2300	G2400	G2500	G2600	G2650	G2700	G2800	Pitch 2850	Lonza KS44
HTT	2300	2300	2400	2500	2600	2650	2700	2800	2850	?
$x_{max}$	0.640	0.657	0.722	0.716	0.759	?	0.786	0.803	0.740	0.860
$d_{002}\text{\AA}$	3.385	3.39	3.37	3.369	3.372	3.373	3.368	3.373	3.383	3.383
$a\text{\AA}$	2.462	2.461	2.459	2.460	2.460	2.461	2.460	2.461	2.463	2.469
$L_a\text{\AA}$	178	158	153	202	180	198	195	191	198	101
$M$	76	76	66	100	72	94	73	96	73	54
$\delta\text{\AA}$	0.06	0.077	0.066	0.061	0.059	0.060	0.054	0.054	0.006	0.09
$P^+$	0.47	0.386	0.308	0.235	0.210	0.200	0.190	0.145	0.265	0.14
$P_t^+$	0.01	0.030	0.055	0.071	0.063	0.072	0.057	0.064	0.064	0.10

\* Fixed during the fitting.

+ Divided by 2.

# Chapter 7

## Summary and Future Work

### 7.1 Summary of the Thesis

As we showed in the introduction and in chapter 2, carbon is not only a very interesting material but also is a very useful material for our society. Scientists and Engineers have made enormous efforts to try to understand and control this very unique material. This thesis basically concentrates on the study of one important application for carbon, the Li-ion cell. The original motivation of this work is from the rapidly developing field of lithium batteries.

We started by establishing a structural model in chapter 2 for disordered and graphitic carbons and then developed an automated refinement program for extracting the structural information. Although the model is simple in some aspects, it works well for almost all the carbons that we studied. To model a complicated material like disordered carbon is no easy job and our refinement program is the first to do this well. Next, we correlated structural data from fitting the X-ray profiles to the electrochemical measurements on carbon and obtained a qualitative understanding of lithium intercalation in disordered carbons.

The refinement program, we believe, is useful for all aspects of carbon research and for the routine quality control analysis needed by carbon manufacturers. For example, using our program, it is easy to determine all structural parameters accurately which can quantify the order and disorder present in any carbon. This program may find

its home in the marketplace!

## 7.2 Suggestions for Future Work

The market for rechargeable batteries is expected to be strongly affected in the future by government safety and environmental regulations. Safe use and ease of disposal will therefore probably become issues for all consumer accessible batteries and in this respect, the carbon based rechargeable lithium batteries might be the best choice. Although it is still too soon to determine the exact place that lithium-ion batteries will occupy in the future, it is now certain that they are the most promising choice amongst many others.

Future work is expected to focus on further improving anode behavior and optimizing various combination of different processing condition such as carbon particle size, surface area, HTT and addition of other elements etc.. Therefore, the following two things are needed in the short term:

1. Optimizing the carbon processing conditions
2. Substituting carbon atoms by other elements, e.g. B, N, O, P or F etc. to explore the changes in  $V(x)$  and  $x_{max}$ .

More experiments on hard carbons and better information on their manufacturing are needed for better understanding. For soft carbons, we have a shortage in carbons above 2800°C and between 1400 and 2200°C. Natural graphite needs to be carefully studied too.

The refinement program needs to be tested on data collected at very small wavelength so that more Bragg peaks can be included in the profile.



# Bibliography

- [1] I. Samaras, S. I. Saikh , C. Julien and M. Balkanski *Material Science and Engineering* **B3** 209-214 (1989)
- [2] M. S. Whittingham, *Prog. Solid State Chem.* **12** (1978)
- [3] D. C. Dahn and R. R. Haering, *Solid State Comm.* **44** 29 (1982) ; J. R. Dahn W. R. McKinnon and R. R. Haering, *Can. J. Phys.* **58** 207 (1980); M.A. Py and R.R. haering, *Can. J. Phys.* **61** 76 (1983)
- [4] K.M Abraham *J. Power Sources* **7** 1 (1981-1982)
- [5] D.P. Wilkinson, J.R. Dahn, U Von Sacken and D.T. Fouchard, Abstracts 53 and 54, p85 and 87, *The Electrochemical Society Extended Abstracts* Vol 90-2, Seattle, WA. October 14-19 (1990)
- [6] D. W. Murphy, *F. Mat Res. Bull* **13** 1395 (1978)
- [7] K. Mizushima, D.C. Jone, etc *Mat Res. Bull* **15** 783 (1980)
- [8] Rosamaria Fong , U. Von Sacken and J. R. Dahn, *J. Electrochem Soc.* **137**, 2009 (1990)
- [9] M. Sato, T. Iijima, K. Suzuki, and K. I. Fujimoto Paper #41 presented at the 1990 fall meeting of the Electrochemical Society, U.S.A. Oct. 14-19 (1990)
- [10] J.R.Dahn, U. Von Sacken, M. W. Juzkow, and H. Al-Janaby, *J. Electrochem Soc.* **138**, 2207 (1991)

- [11] Ron Dagani, *January* **4** 34 (1993); Robert Neff, in Sci.& tech. of *Business Week* Feb 15 **117** (1993)
- [12] R. Kanno, Y. Takada, *J. Power Sources* **26** 575 (1989)
- [13] M. Mohri, N. Yanagigawa, *J. Power Sources* **26** 545 (1989)
- [14] J.R. Dahn, R.Fong and M.J. Spoon *Phys. Rev.*, **B42**, 6424 (1990)
- [15] V.A.Drits C.Tchoubar, *Xray Diffraction by Disordered Lamellar Structures*, Springer-Verlag, 1991
- [16] W. H. Press, S. A. Teukolsky, W. T. Vetlering and B. P. Flannery *Numerical Recipes in Fortran The art of Scientific Computing* second edition, Cambridge University Press
- [17] P.M. Allemand et al. *Science* **253** 301 (1991)
- [18] S. Charkravarty et al. *Science* **254** 970 (1991)
- [19] W. I. F. David et al. *Nature* **353** 147 (1991)
- [20] R. C. Haddon et al. *Nature* **350** 320 (1991)
- [21] Kim Kimoshita *Carbon, Electrochemical and Physicochemical Properties* John Wiley & Sons (1988)
- [22] T. Ishikawa and T. Nagaoki, Eds. *Recent Carbon Technology* JEC Press Inc., The U.S. Office of the Electrochemical Society of Japan, Cleveland, OH, p139 (1983)
- [23] J.D. Bernal *Proc. Roy. Soc. London A* 106, 749 (1924)
- [24] B.E.Warren *J. Chem. Phys.* , **2** 551 (1934)
- [25] B.E.Warren *Phys Rev.* **9** 693-698 (1941)
- [26] B.D.Cullity, *Elements of Xray Diffraction*, 1956
- [27] J. Biscoe and B. E. Warren *J. Appl. Phys.* **13** 346 (1992)

- [28] R.E.Franklin, *Acta Cryst.* **4** 253 (1951) **3** 107, 158 (1950), *J. Chim. Phys.*, **47** 573 (1950),
- [29] C.R.Houska B.E. Warren *J. Appl. Phys.* **25** 204 (1954)
- [30] G.W.Brindley J. Mering *Acta Crystallogr* **4** 441 (1951)
- [31] G. Allegra *Acta Crystallogr* **14** 535 **17** 577 (1961) G.Allegra *Acta Cryst.*,**17** 579 (1964)
- [32] J. Maire and J. Mering *Chemistry and Physics of Carbon V6* 125-190 (1970), *Proc. Conf. Industrial Carbon and Graphite*, London 204 (1957)
- [33] Hang Shi, J.N. Reimers and J.R. Dahn *J. Appl. Crystallography* Accepted for publication (1993)
- [34] R.E.Franklin, *Proc. ROy. Soc. (London)* A209, 196 (1951)
- [35] S.Ergun *Carbon*, **14**, 139 (1976)
- [36] N.W. Ashcroft and N.D. Mermin, *Solid State Physics* (Saunders College, Philadelphia, U.S.A.) p. 79 (1976)
- [37] S. Brunauer, P.H. Emmett and E. Teller, *J. Amer. Chem. Soc.* **60**, 309 (1938)
- [38] Dahn, J.R., Sleight, A.K., Shi, Hang, Reimers, J.R., Zhong, Q and Way, B.M. *Electrochimica Acta.* (1993) Accepted for publication
- [39] S.Ergun in *Physics and Chemistry of Carbons*, Vol **3** edited by P.L. Walker Jr., (Marcel Dekker Inc., New York) (1968), p. 211
- [40] F.A Heckman *Rubber Chemistry and Technology*
- [41] W. Ruland *Acta Cryst*, **18** 992 (1965)
- [42] W.Ruland H. Tompa *Acta Cryst*, **A24** 93 (1968)
- [43] J. Kakinoki, Y. Komura *J Phys Soc Jan* **7** 30 (1952)

- [44] S. Hendricks and E. Teller, *J. chem. Phys.*, **10** 147 (1942)
- [45] A.J.C. Wilson *Proc. Roy. Soc.* **A180** 277 (1942)
- [46] P.A. Plancon C. Tchoubar *J. Appl. Cryst.*, **9** 279 (1976)
- [47] P.P Ewald *Proc Phys Soc.* **52** 160 (1940)
- [48] M.J. Buerger *etc.*, *International Tables For X-ray Crystallography* Vol. **3** The Keynoch Press (1969)
- [49] B.E. Warren *X-ray Diffraction* Addison Wesley, (1969)
- [50] J. Mering *Acta Crystallogr* **2** 371 (1949)
- [51] A. Guinier, *Xray Diffraction in Crystal, Imperfect Crystals, and Amorphous Bodies*, 1963
- [52] Laue *Z Kristallgr* **82** 127 (1932)
- [53] P. Debye, *Ann. Physik* **46**, 809 (1915)
- [54] D.W. Marquardt *J. Soc. Ind. Appl. Math*, **11** 435-441 (1963)
- [55] Philip R. Bevington *Data Reduction and Error Analysis for the Physical Sciences* New York (Mcgraw-Hill) (1969)
- [56] Q. Zhong, U. von Sacken, J. Dahn and Hang Shi *Lithium Intercalation into disordered carbons made from pyrolysis of poly-furfuryl alcohol* to be submitted to publication (1993)
- [57] Y. Nishi et. al *European Patent Application* 89115940.2 August 29, 1989
- [58] J. De Courville-Brenasin, G. Joyez and D. Tchoubar, *J. Appl. Cryst.*, **14** 17 (1981)
- [59] W.R. McKinnon and R.R. Haering *Modern Aspects of Electrochemistry* Vol 15, ed. R.E. White, J. O'M. Bockris and B.E. Conway N.Y Plenum (1982)
- [60] T. Ohzuku preprint *Four volts cathodes for lithium ion battery* (1993)

- [61] Z. X. Shu, R. S. McMillan and J.J. Murray *J. Electrochem. Soc.* **140**, 922 (1993)
- [62] A. K. Sleight and V. Von Sacken *Solid State Ionics*
- [63] D.P. Wilkinson and J.R. Dahn, U.S. *Patent #5*, 130, 211 (1992)
- [64] A. Herold, *Bull. Soc. Chim.* **187** 999 (1955)
- [65] D. Guerard and A. Herold, *C.R. Acad. Sci. Ser. C***275**, 571 (1972)
- [66] J.E.Fischer and H. J. Kim, *Synthetic Metals*, **23**, 121 (1988)
- [67] M. Arakawa and J. I. Yamaki *J. Electroanal. Chem.* **219**, 273 (1987)
- [68] A. N. Dey and B. P. Sullivan *J. Electrochem. Soc.* **117**, 222 (1970)
- [69] E. Peled *J. Electrochem. Soc.* **126**, 2047 (1979)
- [70] S. E. Safran *Solid State Ionics* **40** 183 (1987)
- [71] J.R. Dahn *Phys. Rev. B* **44** 9170 (1991)
- [72] S.A. Sinha and D.W. Murphy *Solid State Ionics* **20** 81-84 (1986)
- [73] S.A. Solin *Advances in Chemical Physics* **49** 455 (1982)
- [74] D.M. Hwang, G. Kirczenow, P. Lagrange, A. Magerl, R. Moret, S.C. Moss, R. Setton and S.A Solin *Graphite Intercalation Compounds I Structure and Dynamics* (1991)
- [75] M.S. Dresselhaus and G. Dresselhaus *Adv. in Physics* **30** 139 (1981)
- [76] J. R. Dahn *Phys. Rev.* **44** 9170 (1991)
- [77] A. Omaru, H. Azuma, M. Aoki, A. Kita and Y. Nishi, *Paper 25, Extended Abstracts of Battery Division p. 34. Meeting of the Electrochemical Society*, Toronto, Canada (1992)
- [78] A. Yoshino, K. Sanechika and T. Nakajima, *Canadian Patent #* 1265580 (1990)

- [79] D. Guyomard and J. M. Tarascon, *J. Electrochem. Soc.* **139**, 937 (1992)
- [80] B. M. Way, J. R. Dahn, T. Tiedje and K. Myrtle *Phys Rev.* **B46** 1697 (1992)
- [81] J.E. Fischer, in *Chemical Physics of Intercalation*, edited by A.P. Légrand and S. Flandrois (Plenum, New York 1987).
- [82] R.C. Boehm and A. Banerjee, *J. Chem. Phys.* **96** 1150 (1992)
- [83] N. Kambe, M. S. Desselhaus, G. Dresselhaus, S. Basu, A. R. McGhie and J. E. Fischer, *Mat. Sci. Eng.* **40** 1, (1979).